

High-precision pulsar timing:
The stability of integrated pulse profiles
and their representation by analytic templates

A thesis submitted to The University of Manchester for the degree of
Doctor of Philosophy
in the Faculty of Engineering and Physical Sciences

2010

Mark Benedict Purver
School of Physics and Astronomy

“The aggregate of our joy and suffering”

Carl Sagan



Figure 1.1: The Earth, photographed from a distance of 43 astronomical units (6.4 billion kilometres) by the Voyager 1 spacecraft on 14th February, 1990. Carl Sagan instigated the picture, terming it the “pale blue dot”. The quote above comes from his reflections on the image (Sagan 1994) (figure credit: NASA/JPL).

Contents

Abstract	13
Declaration	15
Copyright statement	16
Acknowledgements	17
Acronyms and abbreviations	18
1 Introduction to pulsar timing	21
1.1 The complexity and simplicity of pulsars	24
1.2 Measurement of pulse times of arrival	27
1.2.1 Recording of pulse profiles	27
1.2.2 Processing of pulse profiles	32
1.2.3 Determination of pulse times of arrival by the matching of integrated profiles to templates	34
1.3 Calculation of physical quantities from pulsar timing	37
1.3.1 Pulsar system and Solar System parameters	38
1.3.2 Gravitational wave detection using pulsar timing arrays . .	42
2 Pulsar timing with analytic templates	47
2.1 Production of Gaussian pulse templates	48
2.1.1 Observations	48

CONTENTS

2.1.2	Advantages and disadvantages of Gaussian templates . . .	49
2.1.3	Fitting procedure	51
2.2	Tests of the versatility of Gaussian templates	53
2.2.1	Timing of pulse profiles from multiple telescopes using common templates	53
2.2.2	Adaptation of Gaussian templates across a wide frequency range	55
2.2.3	Adaptation of Gaussian templates across a narrow frequency range	59
2.3	Timing solutions	60
2.3.1	Timing of PSR J1022+1001	64
2.3.2	Timing of PSR J1713+0747	67
2.3.3	Timing of PSR J1857+0943	67
2.3.4	Timing of PSR J1939+2134	69
3	Apparent pulse profile instabilities in PSR J1022+1001	75
3.1	The curious case of PSR J1022+1001	76
3.1.1	Findings of previous work	76
3.1.2	Possible causes of apparent profile variation as a function of time	77
3.2	A new analysis of PSR J1022+1001	80
3.2.1	Observations	80
3.2.2	Data reduction	81
3.3	Evaluation of profile variation	85
3.3.1	Profile shape indicators	85
3.3.2	Advantages and disadvantages of the shape indicators . . .	87
3.4	Evolution of profile shape as a function of observing frequency . .	88
3.4.1	Profile shape indicators as a function of frequency and their consistency between sets of observations	88

3.4.2	Absolute amplitudes of profile components as a function of frequency	90
3.4.3	Separation of profile peaks as a function of frequency	92
3.5	Trends in the profile of PSR J1022+1001 over time	92
3.5.1	Profile variation within an observation	94
3.5.2	Profile variation between observations	96
3.6	Statistical analysis of profile variation with time	98
3.6.1	Detection of excess profile variation	98
3.6.2	Magnitude of excess profile variation	102
3.6.3	Phase location of excess profile variation	106
3.6.4	Possible contributors to observed profile variation	107
3.6.5	Comparison of PSR J1022+1001 with PSR J1730–2304 and PSR J1603–7202	110
3.7	Timing of PSR J1022+1001	113
4	Upper limits on the strength of the gravitational wave background from pulsar timing	117
4.1	Method of determination of an upper limit on gravitational wave background strength	118
4.1.1	Algorithm for determination of gravitational wave background upper limit	118
4.1.2	Parameters of a simulated gravitational wave background	122
4.2	Limits on gravitational wave background strength using pulsar timing with analytic templates	123
4.2.1	Tests of the suitability of timing residuals	123
4.2.2	Limits using PSR J1022+1001	124
5	Discussion of results and future work	129
5.1	Pulsar timing with analytic templates	129
5.2	The effect of apparent pulse profile variation on timing accuracy	130

CONTENTS

References

133

List of figures

1.1	Pale blue dot	2
1.2	Composite image of the Crab Nebula and Crab Pulsar in infrared, optical and X-ray light	19
1.3	A simple impression of a pulsar	26
1.4	Diagram of Earth and pulsar systems, showing the vectors used in calculating the geometric propagation delay	41
1.5	The effect of quadrupolar gravitational waves on a ring of points .	44
2.1	TOA residual as a function of TOA uncertainty for PSR J1022+1001	50
2.2	A profile of PSR J0437–4715 at 1405 MHz from Parkes, showing two notches	52
2.3	The Gaussian template of PSR J1713+0747 at 1410 MHz	54
2.4	Gaussian templates for PSR J1857+0943, overlaid on its compo- nents at 1410 MHz, and overlaid at 863, 1410 and 2693 MHz . . .	57
2.5	Gaussian templates for PSR J1939+2134 at 863 and 1410 MHz, overlaid on their components	58
2.6	The two extreme Gaussian templates that were fitted in a weighted sum to profiles of PSR J1022+1001, overlaid on their components	61
2.7	Overlaid Gaussian templates and error-weighted mean profiles of PSR J1022+1001 as a function of frequency from 1321 to 1425 MHz	62

LIST OF FIGURES

2.8	Timing residuals for PSR J1022+1001 when timed with Gaussian templates using full bands and sub-bands	66
2.9	Timing residuals for PSR J1713+0747 when timed with Gaussian and high-SNR templates using full bands	69
2.10	Timing residuals for PSR J1857+0943 when timed with Gaussian and high-SNR templates using full bands	71
2.11	Timing residuals for PSR J1939+2134 when timed with Gaussian and high-SNR templates using full bands	74
3.1	PA and polarisation profiles of PSR J1022+1001 at 1341 MHz from Parkes	79
3.2	Evolution of area ratio for PSR J1022+1001 over a broad range of observing frequency	89
3.3	All shape indicators as a function of frequency for PSR J1022+1001 in Parkes data around 1400 MHz	90
3.4	All shape indicators as a function of frequency for PSR J1022+1001 in Effelsberg data around 1400 MHz, with Parkes for comparison	91
3.5	Evolution of profile peak separation for PSR J1022+1001 over a broad range of observing frequency	93
3.6	Downward trend in area ratio for PSR J1022+1001 on MJD 53995	95
3.7	Mean area ratio per observation for PSR J1022+1001 as a function of time in Parkes data	99
3.8	Variance of mean area ratio per observation for PSR J1022+1001 as adjacent samples are added together in Parkes data	100
3.9	Error-weighted mean profile and reduced chi-squared of normalised profiles as a function of rotational phase in PSR J1022+1001	108
3.10	A fully calibrated profile of PSR J1603–7202 at 1405 MHz from Parkes, showing extended emission and an interpulse	111

3.11	Error-weighted mean profile and reduced chi-squared of normalised profiles as a function of rotational phase in PSR J1603–7202 . . .	113
3.12	Fully calibrated PA and polarisation profiles of PSR J1730–2304 at 1341 MHz from Parkes	114
4.1	Timing residuals for PSR J1022+1001 after addition of an artificial GWB to the real TOAs, before and after refitting	125
4.2	Threshold and positive detection parameter distributions for artificial GWB detection using TOAs from PSR J1022+1001	127
5.1	Blue marble	138

LIST OF FIGURES

List of tables

2.1	E_{quad} values used to increase TOA uncertainties from each telescope and each pulsar	64
2.2	Fitted system parameters of PSR J1022+1001 when timed with Gaussian templates using full bands and sub-bands	65
2.3	Fitted system parameters of PSR J1713+0747 when timed with Gaussian and high-SNR templates using full bands	68
2.4	Fitted system parameters of PSR J1857+0943 when timed with Gaussian and high-SNR templates using full bands	70
2.5	Fitted parameters of PSR J1939+2134 when timed with Gaussian and high-SNR templates using full bands	73
3.1	Reduced chi-squared of mean peak ratio per observation for profiles of PSR J1022+1001 around 1400 MHz	97
3.2	Reduced chi-squared of mean area ratio per observation for profiles of PSR J1022+1001 around 1400 MHz	97
3.3	Reduced chi-squared of mean shape parameter per observation for profiles of PSR J1022+1001 around 1400 MHz	97
3.4	Reduced chi-squared of peak ratio for profiles of PSR J1022+1001 around 1400 MHz	102
3.5	Reduced chi-squared of area ratio for profiles of PSR J1022+1001 around 1400 MHz	102

LIST OF TABLES

3.6	Reduced chi-squared of shape parameter for profiles of PSR J1022+1001 around 1400 MHz	103
3.7	Additional peak ratio relative errors required to explain the spread of values for profiles of PSR J1022+1001 around 1400 MHz	104
3.8	Additional area ratio relative errors required to explain the spread of values for profiles of PSR J1022+1001 around 1400 MHz	105
3.9	Additional shape parameter absolute errors required to explain the spread of values for profiles of PSR J1022+1001 around 1400 MHz	105
3.10	Fitted system parameters of PSR J1022+1001 using sub-bands, timed with fixed and adaptive templates	115

The University of Manchester

ABSTRACT OF THESIS submitted by Mark Benedict Purver
for the degree of Doctor of Philosophy and entitled
HIGH-PRECISION PULSAR TIMING: THE STABILITY OF PULSE PROFILES
AND THEIR REPRESENTATION BY ANALYTIC TEMPLATES. September 2010.

High-precision timing is an exciting field of pulsar research that holds the promise of direct gravitational wave detection. This goal is at the limit of current technology, and requires the near-seamless combination of data from multiple pulsars observed with multiple telescopes. Accuracy in the recording of pulse profiles and the measurement of their times of arrival (TOAs) is key. In order to time a pulsar, a template is needed that is as close as possible to an ideal version of the pulse profile. Four pulsars were timed using analytic, noise-free templates composed of Gaussian components, and their system parameters were measured to high accuracy. These templates were found to be usable at different telescopes and were adaptable across more than 100 MHz in observing frequency without loss of TOA alignment.

The same approach was used to investigate profile variation in the pulsar PSR J1022+1001, which is a promising member of the arrays used to search for gravitational waves. Variation with time was found that is almost equal in magnitude to typical measurement noise. The timing of the pulsar could not be improved using adaptive templates which were allowed to vary with the profile to a limited extent. If the variation is due to instrumental error, then its removal would improve timing accuracy significantly for this pulsar. If it is intrinsic, then it is an interesting and unusual phenomenon. PSR J1022+1001 was compared to two similar pulsars, one of which showed a lesser degree of variation and one of which did not exhibit significant change.

ABSTRACT

Timing of PSR J1022+1001 was used to calculate upper limits on the amplitude of the stochastic gravitational wave background. A reasonable limit was estimated to be $A_{max} = 1.7 \times 10^{-14}$, which is stringent for a single pulsar timed alone. However, there was evidence that the timing residuals were somewhat correlated in time, which can produce an artificially low limit. Nevertheless, PSR J1022+1001 has the potential to make a valuable contribution to gravitational wave detection. Investigation into its variation highlights the fact that the timing of a number of pulsars may be crucially improved by the next generation of processing instruments.

Declaration

I declare that no portion of the work referred to in the thesis has been submitted in support of an application for another degree or qualification of this or any other university or other institute of learning.

Copyright statement

- (i) The author of this thesis (including any appendices and/or schedules to this thesis) owns certain copyright or related rights in it (the “Copyright”) and s/he has given The University of Manchester certain rights to use such Copyright, including for administrative purposes.
- (ii) Copies of this thesis, either in full or in extracts and whether in hard or electronic copy, may be made **only** in accordance with the Copyright, Designs and Patents Act 1988 (as amended) and regulations issued under it or, where appropriate, in accordance with licensing agreements which The University has from time to time. This page must form part of any such copies made.
- (iii) The ownership of certain Copyright, patents, designs, trade marks and other intellectual property (the “Intellectual Property”) and any reproductions of copyright works in the thesis, for example graphs and tables (“Reproductions”), which may be described in this thesis, may not be owned by the author and may be owned by third parties. Such Intellectual Property and Reproductions cannot and must not be made available for use without the prior written permission of the owner(s) of the relevant Intellectual Property and/or Reproductions.
- (iv) Further information on the conditions under which disclosure, publication and commercialisation of this thesis, the Copyright and any Intellectual Property and/or Reproductions described in it may take place is available in the University IP Policy¹, in any relevant Thesis restriction declarations deposited in the University Library, The University Library’s regulations² and in The University’s policy on presentation of Theses.

¹<http://www.campus.manchester.ac.uk/medialibrary/policies/intellectual-property.pdf>

²<http://www.manchester.ac.uk/library/aboutus/regulations>

Acknowledgements

Thank you:

To my supervisor, Herr Professor Doktor Michael Kramer, who, on many occasions, seeded ideas in my mind with a few words that led to months of fruitful work.

To all the people in the Astronomy group at Manchester University who made my PhD an enjoyable experience (that's most of you).

To The University of Manchester itself, which has provided support and facilities and still allows theses to be published without its precisely coloured logo in the top-left-hand corner.

To my family and friends in Manchester, who have given me roots that can only be grown over a long time.

And, especially, to my grandma, who made learning exciting and gave me a head-start in education that I am still using today.

Mark Purver's work was supported by a studentship from the Science and Technology Facilities Council. This thesis was typeset with \LaTeX .

Acronyms and abbreviations

° : ' : ”	Degrees : minutes : seconds (of declination)
BB	Binary barycentre (of a two-body system)
BT	Blandford & Teukolsky (binary orbit timing model)
DD	Damour & Deruelle (binary orbit timing model)
DM	Dispersion measure
EPTA	European Pulsar Timing Array
FFT	Fast Fourier transform
GWB	Gravitational wave background
h : m : s	Hour(s) : minute(s) : second(s) (of right ascension)
IPTA	International Pulsar Timing Array
ISM	Interstellar medium
LEAP	Large European Array for Pulsars
lt-s	Light-second(s)
M_{\odot}	Solar mass(es)
mas	Milli-arcsecond(s)
MJD	Modified Julian Date
MSP	Millisecond pulsar
NANOGrav	North American Nanohertz Observatory for Gravitational Waves
PA	Position Angle (of linear polarisation)
pc	Parsec(s)
PPTA	Parkes Pulsar Timing Array
PSR	Pulsating source of radio (pulsar)
PTA	Pulsar timing array
RA	Right ascension
RM	Rotation measure
RMS	Root-mean-square
SNR	Signal-to-noise ratio
SSB	Solar System barycentre
TAI	Temps Atomique International (International Atomic Time)
TOA	Time of arrival (of a pulse)
yr(s)	Year(s)



Figure 1.2: The Crab Nebula, a supernova remnant and pulsar wind nebula, shown as a composite image of infrared (purple), optical (red/yellow) and X-ray (blue) light. The X-rays reveal the Crab Pulsar and its particle outflows (figure credit: NASA/JPL-Caltech/Univ. Minn./R. Gehrz; NASA/ESA/ASU/J. Hester & A. Loll; NASA/CXC/SAO/F. Seward).

1

Introduction to pulsar timing

Like many phenomena in radio astronomy, pulsars came as something of a surprise upon their discovery in 1967. At the Mullard Observatory in Cambridge, UK, a chance observation by Jocelyn Bell that a bit of radio ‘scruff’ was recurring in the same patch of sky each sidereal day led to the measurement of an extrasolar source that was pulsing radio waves with implausible regularity every 1.337 seconds (Carroll & Ostlie 1996, p. 608). Until then, no-one had expected or sought to detect such rapidly varying celestial radio emission, so pulsar signals were either smoothed out in time integrations or dismissed as man-made interference (Lyne & Smith 2006, p. 2). Realising that the high intensity, extreme regularity, short duration and frequency-dependent dispersion (see § 1.2.1) of the pulses implied tremendously luminous emission from a region of concentrated mass less than 5000 kilometres across and within our own galaxy, Bell and her PhD supervisor, Anthony Hewish, developed with other colleagues the idea that they originated from the vibrational oscillations of a compact stellar remnant – either white dwarf or then-theoretical neutron star (Hewish et al. 1968). A clutch of similar discoveries soon confirmed that these sources, christened as pulsars by the science correspondent of the *Daily Telegraph* newspaper, were a new class of objects, a serendipitous discovery far removed from the solar scintillation of

quasars¹ that Bell had originally been studying (Carroll & Ostlie 1996, p. 608). Neutron stars had been theorised by Baade & Zwicky (1934) as the possible dense remains of stars after observed supernova explosions, but they were not considered likely to be directly detectable, nor even necessarily considered at all by astronomers, before the first pulsar observation. This is illustrated by two papers published in the *Nature* journal in 1967. Bell & Hewish (1967) published evidence in March that the Crab Nebula contained a small radio source that was too bright to be explained by the synchrotron emission characterising the rest of the nebula, but offered no explanation of what it might be: they had detected its pulsar as a continuum source, but had integrated the signal over too long a sampling time to discern its periodicity. In November, Pacini (1967) produced a theoretical description of neutron stars as strong and rapidly rotating magnets, stating that they would be created in supernovae and that the Crab Nebula could be a supernova remnant energised by the low-frequency magnetic dipole radiation from such an object, but did not mention the paper of Bell and Hewish. No work anticipated pulsed radio emission, and it was Gold (1968) who, after its discovery, put forward the case that it was powered by the rotation of neutron stars and independently presented a similar theoretical framework to that of Pacini, citing a co-rotating magnetosphere of plasma surrounding the object as the likely source of radio emission. The speed of the pulses argued against the vibration or rotation of white dwarves, while their inhomogeneous polarisation (Lyne & Smith 1968) favoured the explanation of a rotational sweep over that of a bodily oscillation. The discovery in late 1968 of the Vela and Crab Pulsars (Large et al. 1968; Staelin & Reifenstein 1968), with their short pulse periods of 89 ms and 33 ms respectively, eliminated the possibility of white dwarves. In 1969, the observation that the position angle (PA) of linear polarisation of Vela’s pulses rotated across its profile – where a pulsar’s profile is the average intensity

¹Multi-wavelength sources of very high redshift, now considered to be extremely luminous and distant galactic nuclei in which a supermassive black hole is rapidly consuming matter.

of its signal as a function of pulse phase – provided simple evidence of a rotating emission beam polarised by a radial magnetic field (Radhakrishnan et al. 1969), while the measurement that the period of the Crab’s pulses was gradually increasing (Richards & Comella 1969) refuted the idea that they came from an oscillatory mechanism (see § 1.1). Only then did a consensus develop that pulsars were neutron stars with continuous radio emission that came from parts of their surfaces or magnetospheres and swept over the Earth as they rotated (Lyne & Smith 2006, pp. 5–6). The somewhat reluctant acceptance of this idea may originate in the sheer implausibility of the objects discovered, which packed the mass of the Sun into the volume of a city and spun this incredibly concentrated bulk at a rate previously unheard of in the field of Astronomy, releasing energy through the action of an unimaginably strong magnetic field.

Although the emission mechanism of pulsars remains incompletely understood (see § 1.1), the extraordinary rotational regularity of these time beacons has been explored and exploited since their discovery. Richards & Comella (1969), in measuring the arrival times of pulses from the Crab Pulsar and demonstrating its slowdown, established the basis of the techniques of pulsar timing widely employed today and used in this PhD project (see § 1.2–1.3). The remainder of § 1 describes more of the nature of pulsars and how they may be used as both objects and tools of study through timing. § 2 gives results of timing conducted by matching analytic, noise-free templates to pulse profiles, an approach used throughout the thesis. In § 3, the assumption of profile stability is tested using the pulsar PSR J1022+1001 and others², to see how instability can affect timing accuracy. In § 4, the timing data analysed in the earlier chapters is used to calculate an upper limit on the strength of the cosmic gravitational wave background

²PSR stands for ‘pulsating source of radio’ and designates a pulsar. The rest of the name gives the pulsar’s sky position in hours and minutes of right ascension (RA) and degrees and arcminutes of declination, using equatorial co-ordinates at the J2000 epoch. Alternative names are sometimes given using positions, without arcminutes of declination, at the B1950 epoch.

(GWB), based on the signature in pulse arrival times that would be expected in the presence of a detectable background. §5 discusses pulse profile stability and analytic templates in the context of pulsar timing accuracy and the search for gravitational waves, using the results of the preceding chapters.

1.1 The complexity and simplicity of pulsars

Pulsars are extremely complex objects, and contain environments not reproducible on Earth. Consisting of increasingly neutron-rich atoms towards their centres and supported mainly by neutron degeneracy pressure (Shapiro & Teukolsky 1983, pp.1–2), they are so dense that the state of matter in their cores is unknown (Lyne & Smith 2006, pp.20–21). Their maximum permitted mass is therefore uncertain, and may be as high as $3 M_{\odot}$ (Solar masses) (Shapiro & Teukolsky 1983, p. 4); the few accurate measurements of neutron star masses give a conservative observed range of $1.2\text{--}1.9 M_{\odot}$ (Janssen et al. 2008; Demorest et al. 2010). Pulsars are surrounded by complicated magnetospheres, but models do not yet say how these can be filled by the plasma required to produce electromagnetic radiation (Michel & Li 1999). Charged particles in the magnetosphere are drawn along and around the magnetic field lines and produce light at frequencies across the electromagnetic spectrum, including radio waves whose brightness can only be explained by a coherent mechanism comprising many particles emitting in phase (Lorimer & Kramer 2005, pp. 54–57). The visible pulses show many puzzling phenomena, such as occasionally switching off or *nulling* for several pulses (Lorimer & Kramer 2005, pp.15–16). The propagation of pulses is complicated by the interstellar medium (ISM). They are spread out in time by dispersion and scattering, while the interference patterns of scintillation cause bright and dim patches in time and frequency as seen from Earth. Pulsars are often very weak emitters, and measuring their pulses is an involved process.

However, many elementary deductions about pulsars have allowed them to

become useful astronomical tools. The case for their being rotating neutron stars – as detailed earlier in this chapter – is simple, being the only explanation for their extreme regularity. Their magnetic fields are modelled at first order as simple dipoles, giving rise to verifiable results such as the PA swing across the pulse that is seen in many pulsars (Lorimer & Kramer 2005, pp.75–76). Their emission beams emanate from their magnetic poles and sweep the Earth at regular intervals due to misalignment between their rotational and magnetic axes, leading them to be described as lighthouses or as ticking clocks (Figure 1.3). In some pulsars, weaker emission called an *interpulse* is seen halfway between each main pulse, indicating that both magnetic poles are visible. Their ages and the strengths of their magnetic fields can be broadly estimated from their rates of spin and of slowdown, assuming that they lose rotational kinetic energy through magnetic dipole braking (Lyne & Smith 2006, pp.59–60); this loss of energy accounts for their emission, except in the case of *magnetars*, which give out more electromagnetic energy at high frequencies than can be explained purely by their slowdown (Mereghetti 2008).

Pulsars have one of the best, but certainly the simplest, clock mechanisms imaginable, with such great and concentrated rotating mass that their enormous kinetic energy means they take a very long time to slow down. The most accurate timekeepers among them are the *recycled* or *millisecond* pulsars (MSPs), which appear to have received angular momentum when accreting material from companion stars that got too close within their intense gravitational fields. They spin more quickly and slow down more gradually than the majority of pulsars, having periods of $\sim 1\text{--}100$ ms and rates of period increase (slowdown or *spin-down* rates³) of $\sim 10^{-21}\text{--}10^{-17}$, which indicate that their magnetic fields are, at $\sim 10^4\text{--}10^6$ tesla, weaker than those of ‘normal’ pulsars (Lorimer & Kramer 2005, pp.26–29). The times of arrival of pulses from MSPs can often be predicted with

³‘Spin-down rate’ is also sometimes used to refer to the rate of *decrease* of a pulsar’s rotational frequency, where its frequency is the reciprocal of its period.

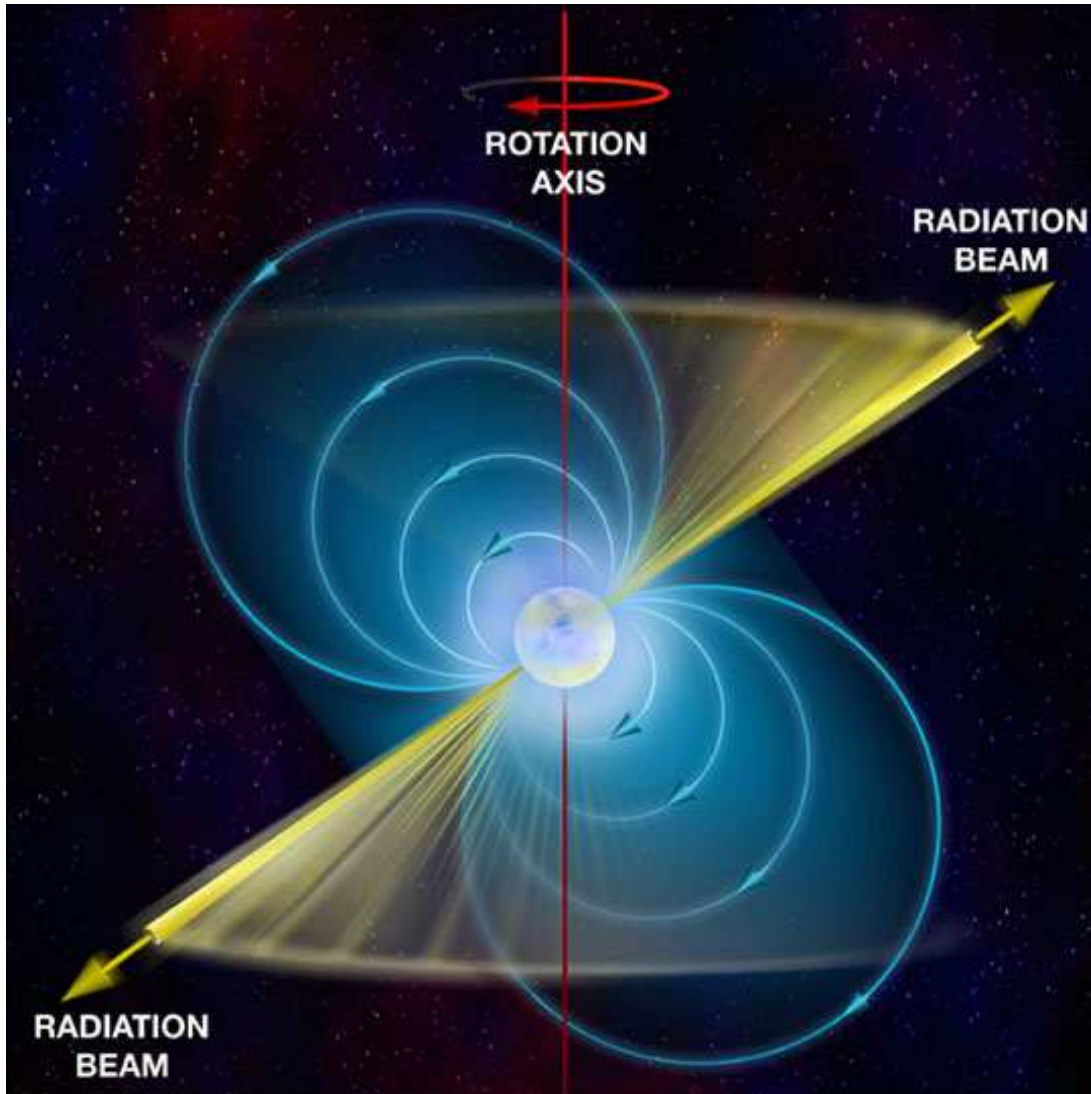


Figure 1.3: A simple impression of a pulsar. The neutron star is at the centre, surrounded by a dipolar magnetic field represented by a two-dimensional cross-section (blue lines with arrows indicating field direction): the three-dimensional field is a repetition of this with circular symmetry about the magnetic axis. The pulsar's radiation beams emerge from the magnetic poles, along the magnetic axis, and are shown sweeping around the rotation axis (figure credit: NRAO/AUI/NSF/B. Saxton).

an accuracy of $\lesssim 1 \mu\text{s}$ over intervals of many years, offering the prospect of making extraordinarily accurate measurements of any phenomenon that alters the pulse times of arrival (TOAs).

1.2 Measurement of pulse times of arrival

The TOAs of pulses from pulsars reveal information about the processing equipment and algorithms used to calculate them, the pulsars' systems, the Solar System and other physical phenomena affecting the propagation of the pulsar signals. The information is found by comparing the TOAs to modelled arrival times which attempt to take these influences into account, using timing software such as TEMPO2 (Hobbs et al. 2006).

1.2.1 Recording of pulse profiles

The rapid variation of pulsar emission requires their observational data to be processed by backends unlike those used for other astronomical applications. Observatories use hardware and, increasingly, software to manipulate the incoming signal as a function of frequency and time so that it can be stored in a relatively compact form suitable for timing.

Polarisation data, rather than simply total intensity, is usually recorded from a pulsar's signal. This allows more accurate reproduction of the profile in total intensity, and also gives polarised profiles which can improve timing precision. The polarisation components of a signal are generally expressed using the four Stokes parameters: I , Q , U and V (see e.g. Burke & Smith 2002, pp. 16–20). I is the total intensity of the signal; $\sqrt{Q^2 + U^2}$ gives its linearly polarised component; V gives its circularly polarised component. The unpolarised component of the signal is $\sqrt{I^2 - Q^2 - U^2 - V^2}$. Each telescope receiver has two feed horns which are sensitive to orthogonal components of the electric field of the incoming radio waves in the plane perpendicular to the line of sight. The components in this

receiver plane may be linear, in perpendicular directions, or circular, in opposite senses of rotation. This allows the full signal to be measured and converted, using mixing in hardware or fast Fourier transforms (FFTs) in software (see e.g. Press et al. 1992, pp. 496–536), into either two products (the magnitudes of the components) or four (the magnitudes and cross-multiplication terms). The use of four polarisation channels doubles the demand for data output and storage but permits the formation of all four Stokes parameters, while the use of two yields only total intensity and one other parameter but allows a greater signal bandwidth to be processed with the same equipment. At least two components are required if the signal is subsequently to be calibrated in polarisation (see § 1.2.2).

Dedispersion of the incoming data, prior to final storage, is the most computationally intensive of the backend processes. A pulsar’s signal is delayed by the ionised component of the ISM as it propagates to Earth, and the length of the delay is a function of electromagnetic frequency:

$$\Delta t \simeq 4.15 \times 10^6 DM f^{-2} \tag{1.1}$$

where f is signal frequency in megahertz, Δt is signal delay in ms relative to a electromagnetic wave of infinite frequency and DM is the pulsar’s *dispersion measure* (DM) in $\text{cm}^{-3} \text{pc}$, which is the integral of the free electron density along its line of sight (Lorimer & Kramer 2005, p. 86). Thus the pulse is dispersed in time across the observational bandwidth. Dedispersion removes the delays in the observed data relative to the central observing frequency so that integration of the data with respect to frequency would represent the summation of photons which left the pulsar at the same time, allowing consistent timing using the whole bandwidth. The incoming signal is first down-converted to a lower frequency so that it can be sampled. It is usually then divided into a number of frequency channels, each containing an integration of the signal over a section of the bandwidth, using a hardware or software filterbank. The latter requires FFTs of the signal from

each feed horn sampled at the Nyquist rate over short, preferably overlapping periods of time, each at least as long as the reciprocal of the desired channel bandwidth, which are each divided up according to frequency and transformed back into separate time series. Longer FFTs reduce the problem of spectral leakage, in which finite FFT length causes signal power near channel edges artificially to spread into two channels; multiplication by a *tapering function*, which decreases values at the ends of the FFTs, may be used for the same purpose (van Straten 2003). A software filterbank necessitates computation and coarsens the time resolution to the Nyquist sampling time for the channel bandwidth, but provides greater flexibility in the number and width of the channels and also enables the four polarisation products to be found from the FFTs without significant further effort. *Incoherent dedispersion* then simply involves applying an appropriate delay to the time series of each frequency and polarisation channel, according to the previously calculated DM of the pulsar. This does not remove dispersion within each frequency channel and so leaves the pulse profile slightly ‘smeared’ in time, but it is effective with channels of narrow frequency width and pulsars of low DM. *Coherent dedispersion* (Lorimer & Kramer 2005, pp.114–120) uses all available frequency information to correct dispersion in the frequency domain with a resolution limited only by computational power and storage space. In this method, overlapping FFTs of the Nyquist-sampled signal in each frequency channel are multiplied by a frequency-dependent *chirp function*. This alters the complex phases of the FFT values in order to remove dispersive delays within the channel, and simultaneously applies a tapering function to the complex amplitudes of the FFTs to inhibit the aliasing of undersampled frequencies above the top of the intended observing band that may be present in the signal. The four dedispersed polarisation products can then be found easily from these FFTs. For Nyquist-sampled data, each FFT must come from a time series at least twice the length of the dispersive delay across the channel bandwidth, with longer FFTs increasing frequency resolution but requiring more computation. Delays are ap-

plied to the inverse FFTs of the dedispersed channels to complete the coherent dedispersion process, and the reconstructed time series are recorded. It is possible to achieve the same result without first dividing the signal into frequency channels, by applying a chirp function to FFTs of the full-bandwidth signal using time series that are at least twice the length of the dispersive delay across the bandwidth, after which channels can be formed from the same FFTs. This requires more processing power and memory than coherent dedispersion of channels produced in software due to the finer time resolution of the signal, but it also achieves finer frequency resolution (Jenet et al. 1997). Dedispersion is more accurate done coherently than incoherently, but requires more computing power as DM and bandwidth increase and as observing frequency decreases. Although the Nyquist-sampled signal may be recorded for later coherent dedispersion, most systems save storage space by dedispersing during the observation. This is usually done with parallel computer central processing units, but graphics processing units are now used at the Nançay observatory in France as their intrinsic parallel structure lends itself to the simultaneous dedispersion of multiple channels (Cognard et al. 2009). The DM of an individual pulsar is not normally strongly time-dependent, but is subject to small variations that can subtly alter profile shape by introducing misalignment into the frequency-scrunching process (see §3.1.2).

The magnetic field in the line of sight to a pulsar also causes the ionised component of the ISM to rotate the signal’s PA by a frequency-dependent angle, ΔPA , which is most easily written in terms of electromagnetic wavelength, λ , in metres:

$$\Delta PA = RM \lambda^2 \tag{1.2}$$

where RM is the pulsar’s *rotation measure* (RM) in rad m^2 , which is the integral of the free electron density multiplied by the parallel magnetic flux density along its line of sight (Lorimer & Kramer 2005, p.88). RM can be measured, and the relative rotation between observing frequencies reversed, analogously with DM

(Lorimer & Kramer 2005, pp187–189). This *derotation* is necessary in order to plot relative PA as a function of pulse phase (see § 1.1).

The data storage required to keep profiles for timing is significantly reduced by a form of time integration called *folding*. After dedispersion, the pulsar signal consists of a time series for each frequency and polarisation channel. Ephemerides of the pulsar and the Solar System are used to convert the epoch of each time sample to a pulse phase corresponding to the rotational phase of the pulsar; the phases are then binned at a resolution typically well below Nyquist sampling, and the intensity values within each phase bin are summed for a length of time greater than the pulse period, typically seconds to tens of seconds. The result is a profile: a time-integrated pulse as a function of phase over a number of rotations of the pulsar, which can also be seen as a time series folded modulo the topocentric pulse period or *folding period*. A profile is, essentially, an average pulse over exactly one period, unique in shape to each pulsar. It may be expressed as a function of phase or time, but the use of phase avoids ambiguity since the length of received pulses in time changes according to the ephemerides. Different profiles are formed at different frequencies and using different polarisation products, but, if these quantities are fixed, the shape of profiles consisting of several thousand pulses is generally stable in time for a given MSP (Liu et al. 2010, in prep.) Highly accurate timing depends on this stability and also, therefore, on the ability to fold with an accurate topocentric period.

The output of a single observation is stored digitally as a three-dimensional set of folded pulse profiles of different epochs, observing frequencies and polarisations which can be manipulated individually and recombined at will. This provides important flexibility in the production of composite profiles. Dedicated software, such as PSRCHIVE (Hotan et al. 2004), is used to view, process and time these profiles.

1.2.2 Processing of pulse profiles

Recorded profiles undergo further processing before they are used for timing. Profiles severely afflicted with radio-frequency interference (‘noise’) are removed or set to zero intensity, either through inspection or automatic recognition. Automatic processes excise ‘bad’ profiles by comparing their total flux (intensity) to those around them in frequency and time: narrowband excision erases a profile if its flux is much greater than the mean⁴ flux of profiles taken within the observing bandwidth at the same time; broadband excision deletes profiles across the bandwidth from a particular time if their integrated flux is much greater than the mean frequency-integrated flux of the profiles near to them in time. The remaining uniform baseline of noise is normally then subtracted from profiles such that the mean intensity in the off-pulse region is zero, although this is not strictly necessary. The off-pulse region, where there is considered to be no pulsar emission, is determined from a profile of high signal-to-noise ratio (SNR). The uncertainty in each profile bin, δP , is taken to be the root-mean-square (RMS) of the values of profile intensity, P , in the off-pulse region after baseline subtraction:

$$\delta P = \sqrt{\frac{1}{N_{off} - 1} \sum_{j=1}^{N_{off}} P_j^2} \quad (1.3)$$

where N_{off} is the number of bins in the off-pulse region and j indicates bin number within this region from 1 to N_{off} .

Many pulsars emit highly polarised radio waves, so calibration of the differently polarised profiles recorded in an observation can be important for the accurate reproduction of the true profile shape in total intensity, as well as in the other Stokes parameters. This amounts to calibration of the two feed horns of a telescope receiver. At some telescopes, a short observation of a polarised

⁴Throughout this thesis, “mean” refers to the arithmetic mean, given by $\bar{z} = \frac{1}{H} \sum_{h=1}^H z_h$ for any set z consisting of H members, while “error-weighted mean” is given by $\bar{z} = \left(\sum_{h=1}^H \frac{z_h}{(\delta z_h)^2} \right) / \left(\sum_{h=1}^H \frac{1}{(\delta z_h)^2} \right)$ for uncertainty δz_h in member z_h . The words “error” and “uncertainty” are used interchangeably.

artificial signal is taken just before or after each pulsar observation and stored separately from the associated profiles. This can then be used to calibrate the profiles for differential gain and phase between the horns at their epoch if there are four polarisation channels, or for differential gain alone if there are two. Some observatories, such as that of the Parkes radio telescope in Australia, also correct for subtle systematic cross-contamination between polarisations arising from slight non-orthogonality between horns and receiver ellipticity (van Straten 2004). For linear feeds observing a pulsar of non-uniform polarisation, non-orthogonality will alter the profile shape in Q , U and I , while ellipticity will not affect I but will mix Q and V . This can be modelled and corrected using observations at different epochs where, for a given source, the rotational phase of the receiver plane about the line of sight will be different (van Straten 2004). This phase is known as *parallactic angle*, and its variation alters the relative amplitudes and phases of radiation picked up by the horns and hence the instrumental response. Equatorially mounted telescopes, like the Westerbork Synthesis Radio Telescope, minimise the need for calibration by maintaining a constant parallactic angle for each source.

Since a pulsar's DM varies by small amounts between observations, timing at very high precision sometimes requires it to be measured regularly so that sufficiently consistent TOAs can be generated at different frequencies. The variations are often too small to be noticeable in the shape of a single frequency-scrunched profile, but large enough to offset TOAs produced from profiles at widely spaced frequencies. Timing using at least two frequencies allows the DM to be fitted using the dispersion law of Equation 1.1 (Lorimer & Kramer 2005, p. 87). These DM corrections can then be applied when the (usually larger) delays are removed relative to infinite frequency during the final timing process. Alternatively, time derivatives of DM can be fitted when timing a set of TOAs produced using multiple frequencies.

A TOA is usually obtained from a 'scrunched' profile, which is a high-SNR

integration in time, observing frequency and polarisation of a number of observed profiles. Time-scrunching uses ephemerides to fold the constituent profiles correctly, while frequency-scrunching employs the pulsar’s DM to do the same. The resulting profile will normally span contiguous ranges of time and frequency covering one complete observation, although scrunching is possible over large and interrupted ranges and is limited only by the quality of the ephemerides used and the variation of DM with time. It may be used, for example, to produce a particularly high-SNR profile as the basis for a template. Polarisation-scrunching gives profiles in total intensity by adding in quadrature the two polarisation channels containing the signal magnitudes from each feed horn. Profiles are usually timed in total intensity, although for some pulsars it can be advantageous to use combinations of several Stokes parameters (see e.g. Britton et al. 2000).

1.2.3 Determination of pulse times of arrival by the matching of integrated profiles to templates

The determination of an individual TOA from an observed profile is based on the assumption that each profile from a single pulsar is a shifted, scaled and noisy version of a template which does not change as a function of time and upon which its characteristic shape allows a fiducial ‘phase of arrival’ to be defined. Matching between template and profile uses the information from all constituent pulses to identify the phase of arrival on the profile, with an error estimate. The TOA and its uncertainty are then calculated for the first pulse within the profile using the epoch at the beginning of the observation and the folding period at that epoch. TOAs and epochs are usually recorded as a Modified Julian Date (MJD), which is expressed in days from the reference epoch of this system.

The template is considered to be an ideal pulse, and is therefore based on a high-SNR profile. The off-pulse region is typically set to constant intensity (usually zero), and the pulse itself may be smoothed to reduce noise. A synthetic

template, consisting of an analytic fit to a profile, may be preferred in order to minimise noise. In this case, the template is a sum of either *Gaussian* or *von Mises* functions, which are generally suitable for representing profile components (see §2). Such a template can be reproduced with any number of phase bins, and the component functions can usually be adjusted in amplitude and width to give phase-aligned templates at nearby frequencies in cases where the profile shape changes measurably across the observational bandwidth (see §2.2.2–2.2.3). The phase of arrival is often defined as the tip of the highest or sharpest profile feature.

Template-matching algorithms commonly employ the method described by Taylor (1992). The relationship between the intensities of profile, P , and template, T , is taken to be:

$$P(t) = a + bT(t - \tau) + G(t) \quad (1.4)$$

where G is the random noise element in the profile, which is assumed to be Gaussian but is not known a priori. P , T and G are discretely and uniformly sampled functions of t , where t can be expressed as either phase or time and covers exactly one folding period. a , b and τ are constants to be calculated from the template-matching, giving the transformations between profile and template: a is the intensity shift; b is the intensity scaling factor; τ is the phase or time shift, expressed in the same units as t . When applying the shift τ , it is assumed that T is periodic in time. The initial value of t is arbitrary: if it is set to the starting epoch of the observation, and the fiducial phase is expressed as a time $t = t_{fid}$ using the folding period at that epoch, then the TOA will be equal to $t_{fid} + \tau$. The values of b and τ are fitted in the frequency domain by minimising the goodness-of-fit statistic χ^2 for the discrete Fourier transforms of $P(t)$ and $bT(t - \tau)$. The complex value of the transform of $P(t)$ in bin q is written in exponential form as $P'_q \exp(\theta_q \sqrt{-1})$, and that of $T(t)$ similarly as $T'_q \exp(\phi_q \sqrt{-1})$, where all values of P' , θ , T' and ϕ are real. This statistic can be expressed explicitly in terms of b

and τ without quantisation of τ or interpolation of the discrete transforms. τ is found iteratively by solving the equation:

$$\sum_{q=1}^{N_{bin}/2} q P'_q T'_q \sin(\phi_q - \theta_q - q\tau) = 0 \quad (1.5)$$

where N_{bin} is the number of bins in the profile (assumed to be equal to the number in the template) and q is transform bin number from 0 to $N_{bin} - 1$. b can be calculated directly once τ is known:

$$b = \left(\sum_{q=1}^{N_{bin}/2} P'_q S'_q \cos(\phi_q - \theta_q - q\tau) \right) / \left(\sum_{q=1}^{N_{bin}/2} T'^2 \right) \quad (1.6)$$

a can then be computed directly from the zeroth bins of the transforms:

$$a = \frac{P'_0 - b T'_0}{N_{bin}} \quad (1.7)$$

One-sigma uncertainties in b and τ are taken to be the excursions of these quantities about their fitted values which increase the value of $\chi^2(b, \tau)$ by 1, providing an uncertainty for the TOA based on the effect of Gaussian profile noise, δP (see § 1.2.2). The uncertainty in τ is:

$$\delta\tau = \delta P / \sqrt{2b \sum_{q=1}^{N_{bin}/2} q^2 P'_q T'_q \cos(\phi_q - \theta_q - q\tau)} \quad (1.8)$$

The uncertainty in b is:

$$\delta b = \delta P / \sqrt{2 \sum_{q=1}^{N_{bin}/2} T'^2} \quad (1.9)$$

This fitting method has been found to yield higher accuracy in template-matching than time-domain techniques, which involve interpolation of the time series T .

TOAs and their uncertainties can be modified after template-matching. Corrections to individual observatory clocks, which are used to determine the epochs of observations, are regularly applied to TOAs in order to convert them to the

international atomic time standard *Temps Atomique International* (TAI)⁵. A constant time offset, or *jump*, may be applied to a set of TOAs to compensate for a uniform delay with respect to another set of TOAs. Such a delay can arise from the use of non-phase-aligned templates, different fiducial phases on the templates or the effects of different observing equipment. DM corrections can be fitted across short periods of time where there are TOAs of different observational frequencies. This alters the dispersive delays which will be taken into account when timing software is used to transform each TOA from its central frequency to infinite frequency for comparison with a timing model. Clock corrections, jumps and DM corrections are applied at the time of TOA-fitting in TEMPO2. If a fit of TOAs shows residuals with a larger or smaller RMS value than expected, their error bars may then be altered to reflect this. They can be multiplied by a constant factor, E_{fac} , if the template-matching uncertainty is found to have been systematically underestimated or overestimated, and they can be added in quadrature to a constant additional uncertainty value, E_{quad} , if a source of error independent of profile noise is found to be associated with the TOAs (see § 2.3).

1.3 Calculation of physical quantities from pulsar timing

In order to derive measurements from pulsar timing, a model is constructed of when pulses are expected arrive, based on whatever factors are known or believed to produce patterns in the TOAs. These parameters are then fitted using the real TOAs with software such as TEMPO2, leaving the fundamental timing quantity,

⁵Observatories generally record daily corrections to their local time standards from the Global Positioning System. This can itself be corrected to TAI daily from the tables of *Circular T*, a regular publication by the Bureau International des Poids et Mesures: <http://www.bipm.org/jsp/en/TimeFtp.jsp?TypePub=publication>

the residual:

$$Residual = TOA_{real} - TOA_{model} \quad (1.10)$$

The fit attempts to minimise the RMS of the error-weighted residuals using the TOA uncertainties derived from Equation 1.8. The parameters of the model are then considered to have measured values, but it is the residuals which contain information about anything *not* in the model and give an indication of the reliability of the parameters and their uncertainties. Many pulsars exhibit unmodelled effects in their residuals, either due to instrumental error, intrinsic pulse shape variability (see § 3), effects of signal propagation or intrinsic rotational instability (‘timing noise’) (see § 2.3.4). These manifest themselves as correlated (non-Gaussian) residuals, showing some pattern but not one able to be fitted to any of those predicted by the timing model.

1.3.1 Pulsar system and Solar System parameters

This sub-section uses information from Lorimer & Kramer (2005, pp. 205–225), Edwards et al. (2006) and Hobbs et al. (2009) throughout. A timing model includes parameters that can be classified as *spin*, such as rotation period, *astrometric*, such as position, and *binary*, such as orbital period, should the pulsar be in a binary system and therefore orbiting a *binary barycentre* (BB). The model also makes use of Solar System parameters and signal DM to predict TOA variations. If a set of parameter values can be found which results in the timing residuals having an uncorrelated distribution comparable to the TOA uncertainties, then the parameters are considered measured to the degree of accuracy permitted by those uncertainties.

The spin parameters are fitted by a Taylor expansion of pulse number as a function of time, using pulse number and its time derivatives at a given epoch in the past, $t = 0$:

$$N(t) = N_0 + \nu_0 t + \frac{\dot{\nu}_0 t^2}{2} + \frac{\ddot{\nu}_0 t^3}{6} + \dots \quad (1.11)$$

where N is pulse number, spin frequency is $\nu = \frac{dN}{dt}$, dots indicate further time derivatives (i.e. $\dot{\nu} = \frac{d^2N}{dt^2}$, $\ddot{\nu} = \frac{d^3N}{dt^3}$ etc.) and subscript 0 indicates values at $t = 0$. An inaccurate value of spin frequency will thus produce a linear slope in timing residuals, an inaccurate value of slowdown rate will produce a quadratic slope and subsequent terms will produce successively higher-order polynomials. More accurate timing and a longer span of TOAs allows more terms to be calculated and improves the precision of those known. For most pulsars, terms from $\ddot{\nu}$ onwards are too small to be measured using current instruments over the time spans so far available.

The use of Solar System and non-spin pulsar parameters can be regarded as corrections from the non-inertial observatory frame of reference to the pulsar's own reference frame, which then allow determination of the spin parameters. The required overall correction to transform TOAs measured at an observatory to those from which spin parameters can be found may be expressed as:

$$\Delta t = \Delta_C - \Delta_D + \Delta_G + \Delta_A + \Delta_S + \Delta_E \quad (1.12)$$

where Δt is the TOA correction, Δ_C is a clock correction, Δ_D is a dispersion correction, Δ_G is the *geometric propagation delay*, Δ_A is the *aberration delay*, Δ_S is the *Shapiro delay* and Δ_E is the *Einstein delay*. These corrections are built into the fitting procedure of TEMPO2, although they are not all always fitted.

Δ_C encompasses the corrections made to observatory time to bring it into line with TAI (see §1.2.3). Δ_D is the correction made during dedispersion to account for frequency-dependent signal propagation delays. Δ_G describes the classical signal travel time change due to the Earth's orbital motion about the *Solar System barycentre* (SSB) and the secular and orbital motion of the pulsar with respect to the SSB. Using \underline{R} as the Earth \rightarrow pulsar position vector at the time of observation, \underline{r} as the SSB \rightarrow Earth position vector at the time of observation ($t = t_{obs}$), \underline{R}_0 as the SSB \rightarrow BB position vector at a fixed reference time in the past ($t = 0$), \underline{k} as the displacement of the BB between the reference time and

the time of observation and \underline{b} as the BB \rightarrow pulsar position vector at the time of observation (all objects being considered to be at their apparent positions as seen from Earth at the TOA), the relation:

$$\underline{R} = \underline{R}_0 + \underline{k} + \underline{b} - \underline{r} \quad (1.13)$$

can be used to write the geometric propagation delay, $\Delta_G = (|\underline{R}_0| - |\underline{R}|)/c$ (where c is the speed of light), as a Taylor series:

$$\Delta_G \simeq \frac{r_{\parallel} - k_{\parallel} - b_{\parallel}}{c} + \frac{1}{c|\underline{R}_0|} \left(-\frac{|\underline{r}_{\perp}|^2}{2} - \frac{|\underline{k}_{\perp}|^2}{2} - \frac{|\underline{b}_{\perp}|^2}{2} + \underline{r}_{\perp} \cdot \underline{k}_{\perp} + \underline{r}_{\perp} \cdot \underline{b}_{\perp} - \underline{k}_{\perp} \cdot \underline{b}_{\perp} \right) \quad (1.14)$$

where $x_{\parallel} = \underline{x} \cdot \underline{R}_0$ and $\underline{x}_{\perp} = \underline{x} \times \underline{R}_0$ for any vector \underline{x} . Figure 1.4 is a diagram of the vectors in Equation 1.13. Higher-order terms are smaller, but may be included for greater accuracy if their contributions are detectable. Terms involving \underline{r} and \underline{b} can be measured by the sinusoidal patterns they produce in timing residuals. \underline{r} is normally considered known and is based on an existing ephemeris, so $\frac{r_{\parallel}}{c}$, the *Römer delay*, allows the position of the pulsar to be determined. Recently, however, Champion et al. (2010) fitted the position of the SSB itself in order to measure planetary masses in the Solar System. TEMPO2 allows \underline{b} to be fitted with more than one binary model. The two most commonly used, referred to as BT (Blandford & Teukolsky 1976) and DD (Damour & Deruelle 1986), incorporate relativistic effects. For close, regular pulsars, $-\frac{|\underline{r}_{\perp}|^2}{2c|\underline{R}_0|}$, the *parallax delay*, can be measured and provides a precise distance value. Because \underline{k} is not generally periodic in time, the contribution of $-\frac{k_{\parallel}}{c}$ is lost in fitting to the apparent spin period, while that of $-\frac{|\underline{k}_{\perp}|^2}{2c|\underline{R}_0|}$ is similarly subsumed into the spin period time derivative, making it appear higher than its intrinsic value in the case of constant transverse velocity between the SSB and BB (the *Shklovskii effect*); if there is radial acceleration of the BB relative to the SSB due to an external gravitational field, the apparent spin period time derivative may be higher or lower than its intrinsic value. Transverse secular motion, \underline{k}_{\perp} , may eventually be observed through a change in the direction of \underline{R}_0 or through the coupling of \underline{k}

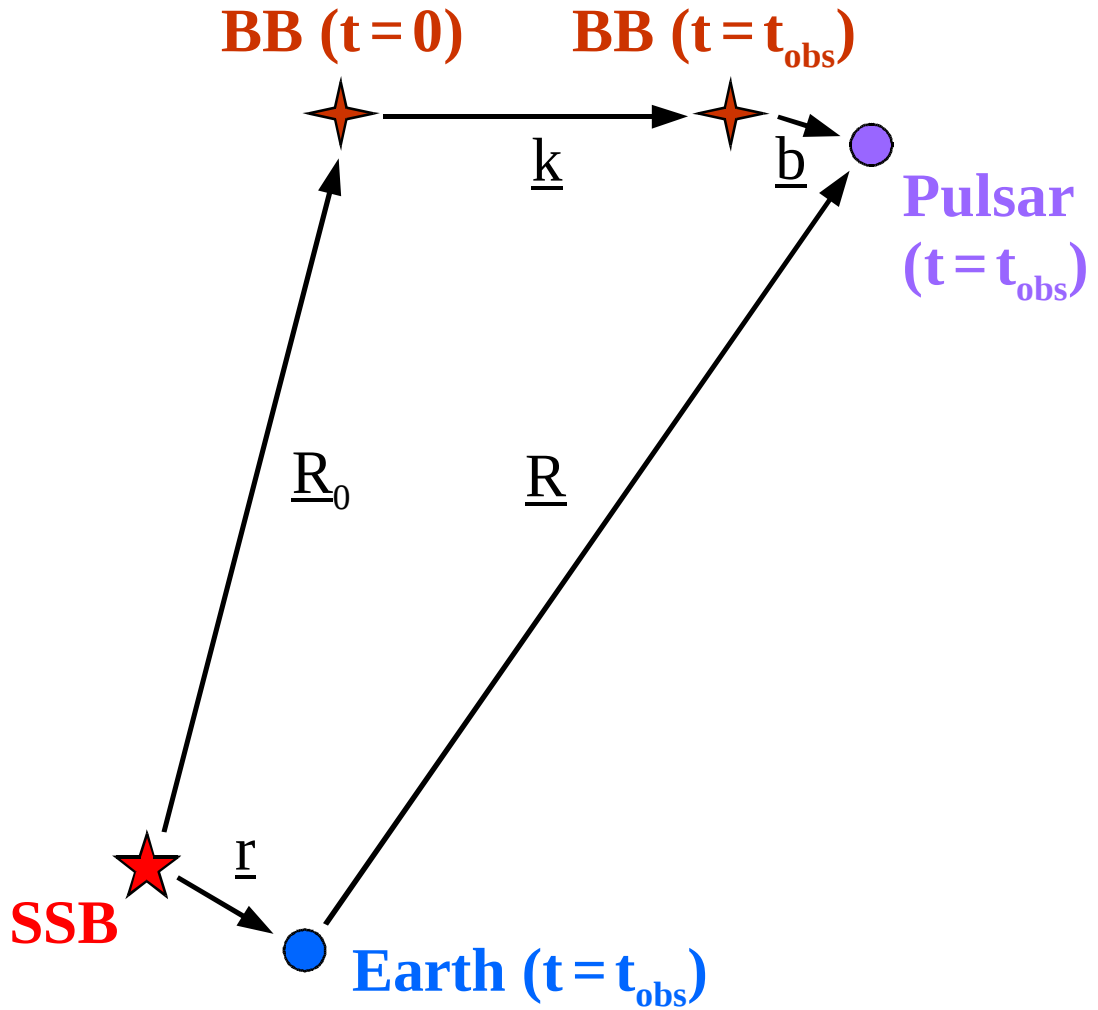


Figure 1.4: Diagram of Earth and pulsar systems (not to scale), showing the vectors used in Equations 1.13–1.14 to calculate the geometric propagation delay. The reference time is $t = 0$ and the time of observation is $t = t_{obs}$.

to other vectors in the higher-order terms of Equation 1.14; with next-generation telescopes, contributions of still higher order will be accessible for many pulsars, allowing the full determination of distance, secular velocity and binary motion to high accuracy.

Δ_A allows for Lorentz transformation of the pulse beam's direction and time of emission between the pulsar and observatory reference frames, which is periodic over time in the case of a binary pulsar. Δ_S removes the effect of relativistic

signal deflection due to passage through the gravitational fields of massive bodies between the pulsar and the Earth, notably any pulsar companion and the larger bodies in the Solar System, which alter the space-time path of the signal. Δ_E subtracts two effects: the first is the general relativistic time dilation caused by the gravitational fields of the Solar System (including Earth) and of the pulsar’s companion, which slow down time at the observatory and the pulsar respectively relative to time outside these fields; the second is the special relativistic time dilation caused by the orbital motions of the pulsar, if it is in a binary orbit, and of the Earth.

The overall impact of the corrections summarised in Equation 1.12, ideally, is to transform the observatory-measured TOAs into TOAs as measured by a perfect observing clock in the pulsar’s frame of reference but subject to no gravitational field, the measured signals having been emitted from within the gravitational field of the pulsar alone and having propagated to the observer without aberration, deflection or dispersion.

1.3.2 Gravitational wave detection using pulsar timing arrays

This section uses information from Misner et al. (1973, pp. 943–954) throughout. General relativity predicts that non-spherically symmetric accelerations of mass – in orbiting binary systems, for example – will lose kinetic energy in the form of quadrupolar gravitational radiation (and, to a lesser extent, in higher multipoles), which manifests itself as sinusoidally oscillating, propagating distortions of space-time separable from familiar non-propagating gravitational fields in regions where the static field is weak. These *gravitational waves* propagate at the speed of light and periodically ‘stretch’ and ‘squash’ space perpendicular to their direction of motion. The maximum amplitude, or *strain*, of a gravitational wave, h_0 , is expressed as the maximum fractional change in any length of space subject to

the wave:

$$h_0 = \frac{L_{max} - L_{min}}{L_0} \quad (1.15)$$

where L_0 is the length of the space in the absence of the wave and L_{max} and L_{min} are the maximum and minimum lengths of the space due to the wave. The time-variable amplitude of the wave, $h(t)$, can be written in a familiar form if $h_0 \ll 1$:

$$h(t) = h_0 \sin\left(\frac{2\pi z}{\lambda} - 2\pi ft\right) \quad (1.16)$$

where z is distance in the direction of propagation, t is time, λ is wavelength and f is wave frequency. An illustration of the effects of the two orthogonal polarisations of a quadrupolar gravitational wave on a circular ring of points in the plane perpendicular to their direction of propagation is shown in Figure 1.5. If this ring has an initial radius r , and the perpendicular axes of its later ellipses have time-variable lengths $a(t)$ and $b(t)$, then these quantities are related by:

$$a(t) = r \left(1 - \frac{h_0}{2} \sin(2\pi ft)\right) \quad (1.17)$$

and:

$$b(t) = r \left(1 + \frac{h_0}{2} \sin(2\pi ft)\right) \quad (1.18)$$

Binary systems produce gravitational radiation predominantly at a wave frequency of twice their orbital frequency, while violent events such as supernovae produce bursts of waves. Current ground-based interferometers, such as LIGO (Laser Interferometer Gravitational-Wave Observatory) and the future spaced-based interferometer LISA (Laser Interferometer Space Antenna), aim to detect gravitational waves in the approximate frequency ranges ~ 0.01 – 1 kHz and ~ 1 – 100 mHz respectively. Since gravitational waves should change the path length of pulsar signals as they propagated to Earth, pulsar timing can, in principle, be used to detect them. Detweiler (1979) first assessed the prospects of using pulsar timing residuals to observe gravitational waves of much lower frequency, ~ 3 – 30 nHz, corresponding to periods of ~ 1 – 10 years. The periodic effects of

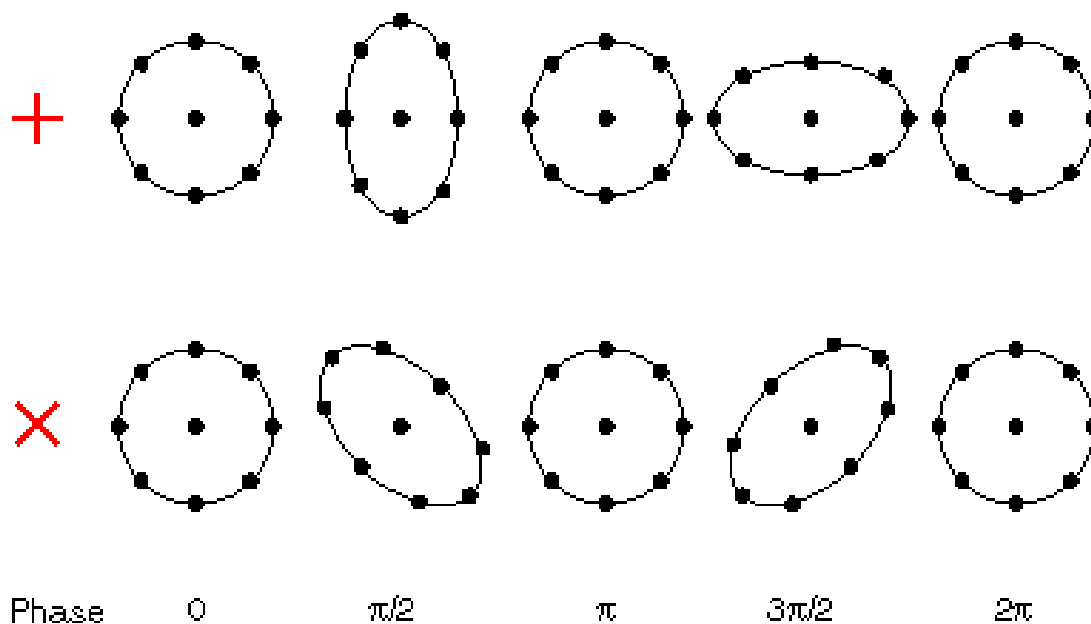


Figure 1.5: The effect of quadrupolar gravitational waves of orthogonal polarisations on a circular ring of points over one wave period. The polarisations differ by a rotation of $\pi/4$ radians (45°). The direction of wave propagation is perpendicular to the plane of the ring (figure credit: LSU/S. Merkowitz).

higher- and lower-frequency waves would be largely lost in residual noise or in the fit for effects of the Earth’s orbit on TOAs, but, by keeping timing residuals low over years of observations, these long-period waves might be detectable using stable MSPs.

The best prospects may come not from single, strong bursts of waves creating clear residuals, but from a stochastic background of sources producing a ‘red’ residual noise signature, which is one containing more power at lower frequencies (Jenet et al. 2005). A number of calculations have been made, using years of observations from one or more pulsars, constraining the energy density of this background from the expected major sources of coalescing massive black hole binary systems and a cosmic GWB due to the decay of cosmic strings and the production of ‘relic’ waves in the early Universe (Jenet et al. 2006). Propagating spatial distortions at both a pulsar and Earth would alter the total path length of

the pulsar's signal and so contribute to the timing residual, but the contribution at Earth would be correlated across all observable pulsar residuals, suggesting that correlated timing in the form of a pulsar timing array (PTA) would be the most sensitive pulsar gravitational wave detector (Hellings & Downs 1983).

Three timing projects now collaborate in an International Pulsar Timing Array (IPTA) (Hobbs et al. 2010), which brings together high-quality MSP observations from all over the World: the European Pulsar Timing Array (EPTA) (Janssen et al. 2008), the North American Nanohertz Observatory for Gravitational Waves (NANOGrav) (Jenet et al. 2009) and the Parkes Pulsar Timing Array (PPTA) (Manchester 2008). This may make a gravitational wave detection before the next generation of radio telescopes is operational, by using not only combined observations but also, in the case of the EPTA initiative known as the Large European Array for Pulsars (LEAP), phase-correlated observations to increase sensitivity (Ferdman et al. 2010). Currently, PTA observations are used to place upper limits on the background of gravitational waves permeating the Universe. These are described as maximum values of a dimensionless amplitude, A , which is the total strain due to gravitational waves, h_c , at a frequency of 1 yr^{-1} . This value depends on the power spectrum of the waves, characterised by a spectral index α :

$$h_c(f) = A \left(\frac{f}{\text{yr}^{-1}} \right)^\alpha \quad (1.19)$$

Jenet et al. (2006) gave a range of $10^{-15} < A < 10^{-14}$ due to massive black holes, as predicted by various theoretical models for which $\alpha = -2/3$. The empirical upper limit on the strength of the GWB with this spectrum was given by Jenet et al. (2006) as $A_{max} = 1.1 \times 10^{-14}$, just above the top of this range.

2

Pulsar timing with analytic templates

It is increasingly clear from high-precision pulsar timing results that the combination of data from many of the World's largest radio telescopes is a necessary step towards targets such as gravitational wave detection with the current generation of instruments (Hobbs et al. 2010) (see § 1.3.2). Phase alignment of timing templates across different frequencies and telescopes is important in attempting to create seamless TOA sets using all available high-quality data. Analytic templates, described by algebraic equations, are simple, flexible and noise-free, and can be used on different data sets and adapted to different frequencies while maintaining good phase alignment. They also allow the subtleties of pulse profile shapes to be quantified and studied. They are, nevertheless, an approximation to reality, and their adaptability has limits.

For this chapter, Gaussian templates (see § 1.2.3) were assessed by employing them to time four MSPs used in PTAs, with profiles produced at three different telescopes at widely separated observing frequencies. The TOAs were combined with pre-existing TOAs that had been created using conventional high-SNR templates and profiles from a further three telescopes. Gaussian templates attempt

to replicate real pulse profile components and are analytic, having the form:

$$T(x) = \sum_{g=1}^{N_{gauss}} \frac{a_g e^{-(x-b_g)^2}}{2c_g^2} \quad (2.1)$$

where x is profile phase, g is an integer indicating Gaussian component number from 1 to N_{gauss} and a , b and c are the parameters of the N_{gauss} components.

2.1 Production of Gaussian pulse templates

2.1.1 Observations

Gaussian templates were fitted semi-automatically to coherently dedispersed profiles of PSR J1022+1001 recorded at the Effelsberg, Parkes and Westerbork radio telescopes (see §2.1.3). The same was done for coherently dedispersed profiles of PSR J1713+0747, PSR J1857+0943 and PSR J1939+2134 observed at Effelsberg. For the latter three pulsars, the templates were used to produce TOAs which were combined with pre-existing TOAs obtained from the Arecibo, Lovell (Jodrell Bank), Nançay, Parkes and Westerbork radio telescopes. The Arecibo and Jodrell profiles were incoherently dedispersed, the others coherently dedispersed. All the telescopes are of 100-m class, with diameters or equivalent diameters of 305 m at Arecibo (or less, depending on the angle of the dish to the line of sight to a source), 100 m at Effelsberg, 96 m at Westerbork, 94 m at Nançay, 76 m at Jodrell Bank and 64 m at Parkes. Of the profiles studied and used for timing, those from Effelsberg came from total observational bandwidths of 45 MHz centred on 863 MHz, 56 MHz centred on 1410 MHz and 112 MHz centred on 2695 MHz; those from Parkes came from two bands of 48 MHz each in width, centred on 1341 MHz and 1405 MHz; those from Westerbork came from a bandwidth of 160 MHz centred on 1380 MHz (see §3.2.1 for further details of the processing instruments used). Profiles at around 1400 MHz formed the great majority of data examined.

Profiles were processed before being used to create Gaussian templates or

being timed with them. Those from Effelsberg were calibrated for differential gain using Effelsberg’s own software, while those from Parkes were calibrated for differential gain and phase and, for one receiver, instrumental imperfections (see § 1.2.2 and § 3.2.2) using the PSRCHIVE data reduction suite. The Effelsberg software performs the same basic polarisation calibration functions as PSRCHIVE, without receiver calibration but with the additional capability to calibrate profiles containing two polarisation channels (see § 1.2.1), such as many of those recorded at Effelsberg. The band edges of the Parkes data were excised due to low sensitivity to these frequencies, leaving the bandwidth quoted above. At Effelsberg and Westerbork, this had already been done. Individual frequency channels which contained noise or were instrumentally defective were identified by eye and removed from individual Effelsberg observations. Some additional clock corrections were manually added to the Effelsberg data, where mistakes had been made in producing the standard clock corrections; this was checked among all the pulsars to ensure consistency. Once TOAs had been produced, those which were subject to apparent instrumental errors were removed, as were any with an uncertainty above $15\ \mu\text{s}$. The latter condition was imposed because large uncertainties are underestimated by their calculation procedure, as shown in Figure 2.1.

2.1.2 Advantages and disadvantages of Gaussian templates

When producing TOAs, template-matching assumes that a template is a perfect representation of the pulse profile with which it is correlated (Taylor 1992). If a template is a high-SNR profile, however, it will contain instrumental noise which violates this assumption. In particular, if the constituent profiles of the template are timed with that template, the common noise components may correlate, resulting in underestimated TOA uncertainties (Liu et al. 2010, in prep). Although the effects of template noise are small for high-SNR templates, smoothing is desirable to remove it. Gaussian template-fitting provides a simple and robust method

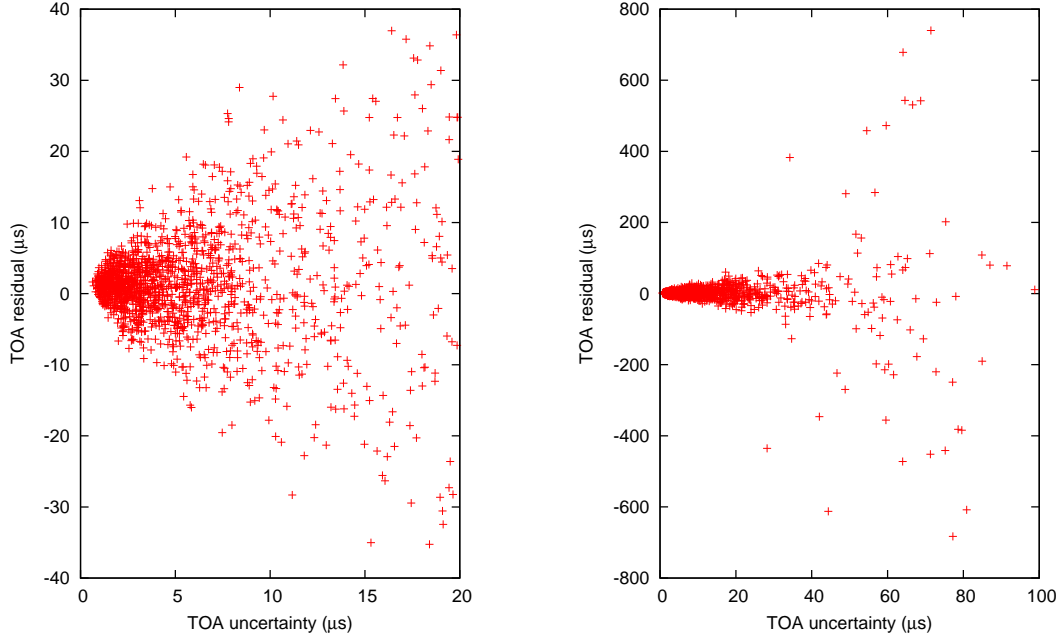


Figure 2.1: TOA residual as a function of TOA uncertainty for PSR J1022+1001, shown for uncertainties up to $20 \mu\text{s}$ (left) and up to $100 \mu\text{s}$ (right). Below an uncertainty of about $20 \mu\text{s}$, the distribution of residuals is consistent with the uncertainties. Above it, the uncertainties increasingly underestimate the residuals, necessitating a maximum error cutoff when timing. These data were produced using Gaussian templates, but the underestimation is a general result when template-matching to low-SNR profiles.

to produce a noise-free template, which often produces better results than other forms of smoothing such as the removal of high spatial frequencies. Because pulse components resemble the Gaussian template components, it is usually possible to fit fine pulse features without fitting noise. Where only a relatively low-SNR profile is available, such as in the case of a weakly detected or recently discovered pulsar, a noise-free fit is especially useful.

Perhaps the greatest advantage of Gaussian templates is that they are adaptable, because they are characterised by just a few well-defined components. As well as being usable with profiles from different telescopes (see § 2.2.1), the parameters of the Gaussians can be used to check whether profiles have systematic

differences between those telescopes. If the component centres are kept fixed, they can take advantage of the smooth evolution of profiles with emission frequency to model those changes by a similarly smooth variation in component widths and relative heights, ideally resulting in phase-aligned templates at different observing frequencies (see §2.2.2–2.2.3). This adaptability can reduce or eliminate the need for the offsets, known as jumps, that as are normally required between TOAs produced using different templates (see §1.2.3).

Gaussian templates, while they fit the pulsars investigated here well, do not always allow a sufficiently accurate representation of a pulse profile using a reasonable number of components. The general shape of PSR J0437–4715, for example, and in particular its so-called notches (Figure 2.2) (Navarro et al. 1997), are difficult to fit adequately in a high-SNR profile using even 30 Gaussian components (Liu 2009, personal communication), although Gangadhara & Thomas (2008) successfully used 11 components to fit a profile of lower SNR in which the notches were not discernible. It also cannot be shown that there is a uniquely defined optimum Gaussian fit to any specific profile. Each template component does not necessarily correspond to a single physical profile component, so quite different components may be used to produce multiple reasonable fits to a complex profile. The initial parameters of components affect the outcome of automated fitting, and it is up to the judgement of the user to decide which apparent profile features should be fitted and which are instrumental or the result of noise. If spurious features are fitted, systematic timing artefacts may be introduced. For these reasons, it is best to fit a Gaussian template to a high-SNR profile, and to use as few components as give a reasonable correlation between the two.

2.1.3 Fitting procedure

Gaussian templates were fitted to profiles using the interactive `BFIT` programme, written in `FORTRAN77` by Michael Kramer and described (in all but name) by

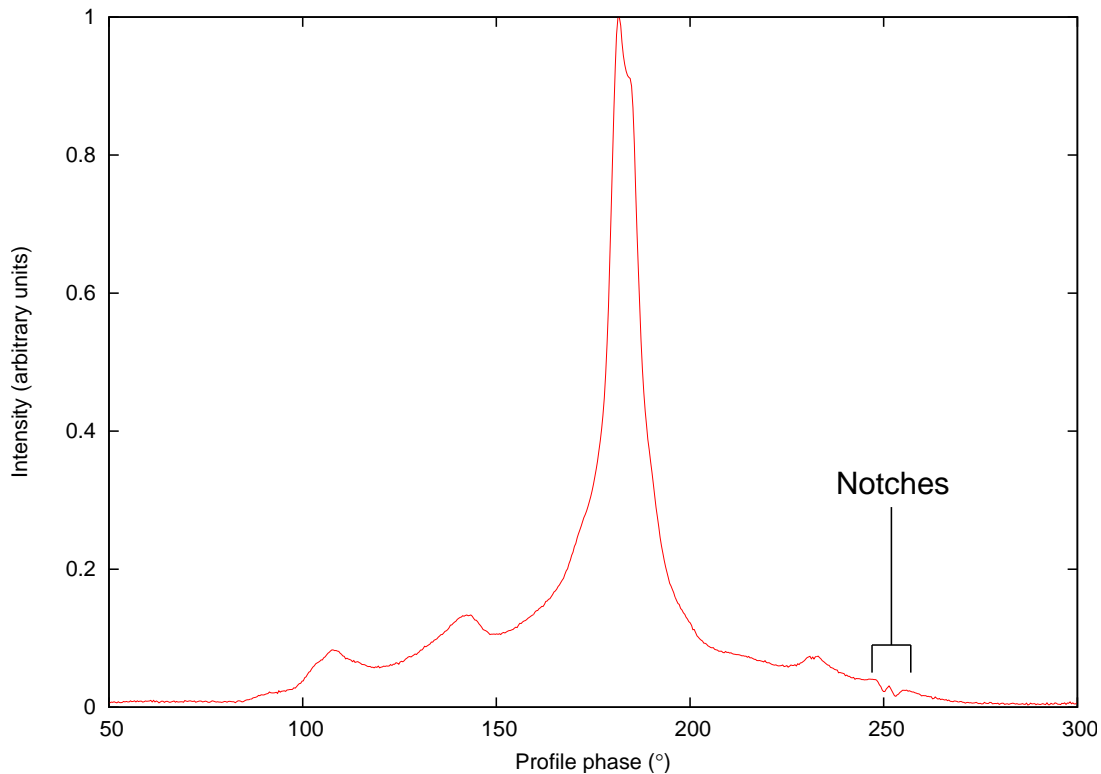


Figure 2.2: A profile of PSR J0437–4715 at 1405 MHz from Parkes, showing two notches immediately around 250° of phase. These features are among several in the profile that are difficult to fit using Gaussian components. The integration time of the profile is 64 minutes and the bandwidth is 48 MHz.

Kramer et al. (1994). The subject profile is first loaded and can be shifted and scaled in amplitude and shifted in phase as desired. The user then selects an initial template component position, height and width to correspond approximately to what appear to be real pulse components. Further components may be added, and the user can, at any point, view the summed template, individual numbered template components and profile, overlaid in any combination. Once enough components are considered to be roughly in place, they can be automatically fitted to the profile by either a downhill simplex or Levenberg-Marquardt algorithm (Press et al. 1992, pp.408–412, 683–688) in order to converge on a better template. The former is often best used first, before refinement using the latter. The previous fitting step can be undone if the fitting algorithm is

found to have become unstable and produced a divergent template solution. The residuals between profile and fitted template can be viewed in order to decide where further components may be needed. These are then added manually and the fitting process is repeated. The reduced chi-squared of the template about the profile can be viewed, and new components added and fitted until it is sufficiently close to 1 to satisfy the user. For this work, a template producing a value of between 1 and 1.05 was considered acceptable, as long as the residuals also resembled the off-pulse profile noise and showed no significant structure. Figure 2.3 shows the 7-component Gaussian template fitted to a high-SNR Effelsberg profile of PSR J1713+0747 observed at 1410 MHz, which was used to time the other Effelsberg profiles.

Any parameters of any template components can be kept fixed in a fit using BFIT. Frequency adaptation was achieved by loading a template produced at one frequency and fitting it to a profile produced at another, keeping the Gaussian component centres fixed (see § 2.2.2).

2.2 Tests of the versatility of Gaussian templates

Gaussian template adaptation and timing were conducted using PSR J1022+1001, PSR J1713+0747, PSR J1857+0943 and PSR J1939+2134 in order to test the flexibility of Gaussian templates discussed in § 2.1.2. This provided tests of their ability to produce consistent results across telescopes and to be adaptable to different observing frequencies.

2.2.1 Timing of pulse profiles from multiple telescopes using common templates

The quality of timing obtained using the same Gaussian templates with profiles from Effelsberg, Parkes and Westerbork was investigated using PSR J1022+1001.

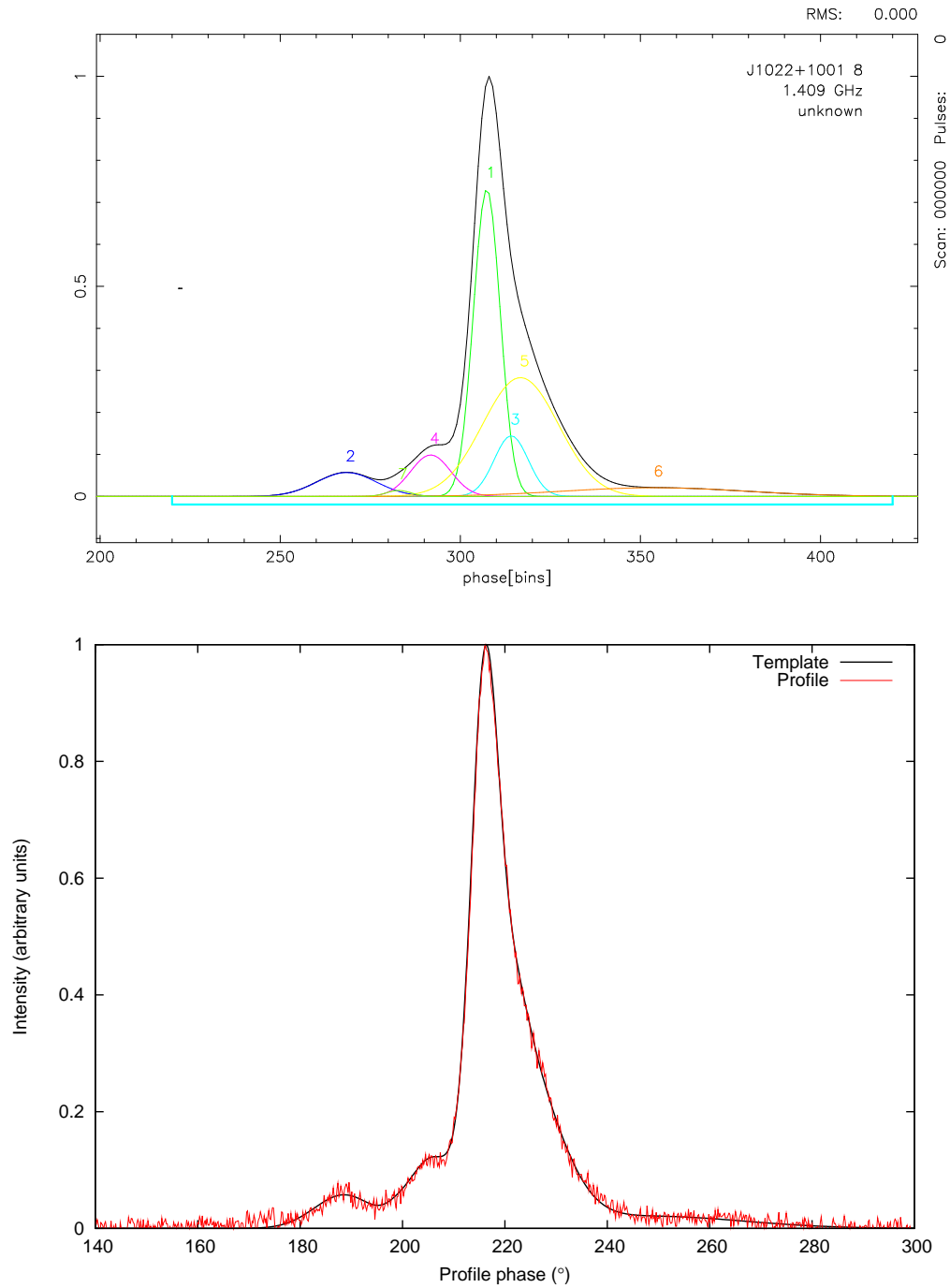


Figure 2.3: The Gaussian template of PSR J1713+0747 at 1410 MHz, with the numbered components overlaid on the black summed template (top), and the template overlaid on the profile to which it was fitted (bottom). The top panel is a screenshot from BFIT.

Because this pulsar is subject to strong scintillation (Hotan et al. 2004) which can vary its SNR across the observational bandwidth, it was timed using profiles of full bandwidth and separately using profiles in sub-bands of ~ 8 MHz bandwidth. Its profile also changes significantly over a small frequency range around 1400 MHz (see § 3.4), so its template was adapted for the different full bands and sub-bands, keeping component centres fixed, by fitting to high-SNR mean profiles (see § 2.2.3). Where frequencies coincided closely, templates based on profiles from Parkes were used for all telescopes. The basis template consisted of 5 components.

Assessing the profile shape of PSR J1022+1001 is difficult as it seems to change slightly over time (this, and systematic profile differences between telescopes, are investigated in § 3). Nevertheless, the templates changed smoothly with frequency and this was a consistent trend among profiles from all telescopes. Jumps were still required between the sets of TOAs from different telescopes, but they were very much smaller than one pulse period, being around $10 \mu\text{s}$ between Effelsberg and Parkes and $0.1 \mu\text{s}$ between Effelsberg and Westerbork. They were, presumably, due to instrumental offsets. The TOAs fitted together well when jumps were included, with their residuals showing no obvious systematic effects and only slightly greater degrees of spread than their uncertainties implied. The resulting timing parameters agreed well with values published by Hotan et al. (2006), taking into the account the different Solar System ephemeris used, and the full-bandwidth and sub-band timing parameters were all consistent with one another to within their uncertainties for each pulsar (see § 2.3.1).

2.2.2 Adaptation of Gaussian templates across a wide frequency range

Gaussian templates were adapted across a frequency range of approximately 2000 MHz for PSR J1857+0943 and PSR J1939+2134 using Effelsberg profiles, with mixed results. Both pulsars have interpulses and required a high number of

components to make a good fit to their profile shapes. PSR J1857+0943 needed 14 components, but these were successfully adapted from 1410 MHz to 863 MHz and 2695 MHz using BFIT, keeping their centres fixed. The pulse and interpulse narrow as frequency increases, while the main pulse peaks move closer together, but, as each peak consists of multiple components, this can all be accounted for by adjusting the component heights and widths (Figure 2.4). Only four TOAs at 863 MHz, and two at 2695 MHz, had sufficient SNR to be used in the timing analysis, so any phase offset from those at 1410 MHz could not be determined, but they appeared to fit in well without jumps (see § 2.3.3) and helped a calculation of DM that agrees with published values (Kaspi et al. 1994).

PSR J1939+2134 needed 13 components at 1410 MHz, which were able to be adapted to 2639 MHz using BFIT, without moving the component centres. However, similar adaptation to 863 MHz was not possible without the addition of a 14th component (Figure 2.5). The peaks of the main pulse get further apart as frequency increases and are well merged at 863 MHz, and it was the trailing peak of the main pulse that required the extra component. This change may be due to adjacent physical pulse components rising and falling in amplitude as frequency changes, but it may equally be due to broadband emission regions of the pulsar having different positions at different frequencies, rather than just different widths. It is clear that Gaussian template adaptation across a sufficiently wide frequency range requires either components that are redundant at some frequencies or component centres that change as a function of frequency, both of which approaches make phase alignment uncertain across the range. In general, phase alignment may be restricted to a few hundreds of MHz without absolutely simultaneous observations. PSR J1939+2134 also suffers from apparent timing noise and variable propagation effects that make it difficult to reconcile TOAs of different epochs and frequencies (see § 2.3.4). Of the Effelsberg profiles, only those from around 1400 MHz were used for timing.

2.2: TESTS OF THE VERSATILITY OF GAUSSIAN TEMPLATES

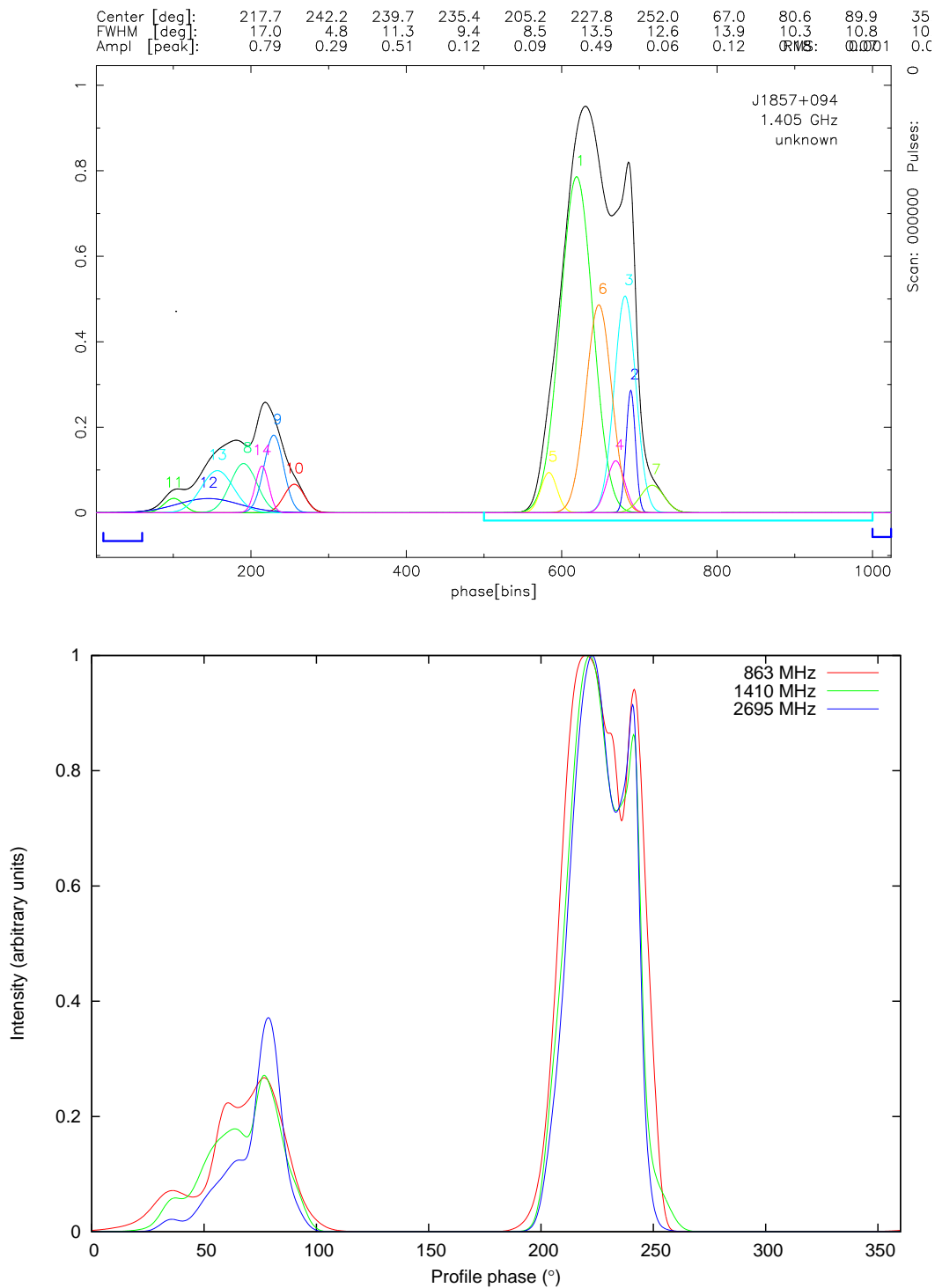


Figure 2.4: Gaussian templates for PSR J1857+0943, in black at 1410 MHz and overlaid on its numbered components (top), and overlaid at 863, 1410 and 2693 MHz (bottom). The main pulse and interpulse both narrow as frequency increases.

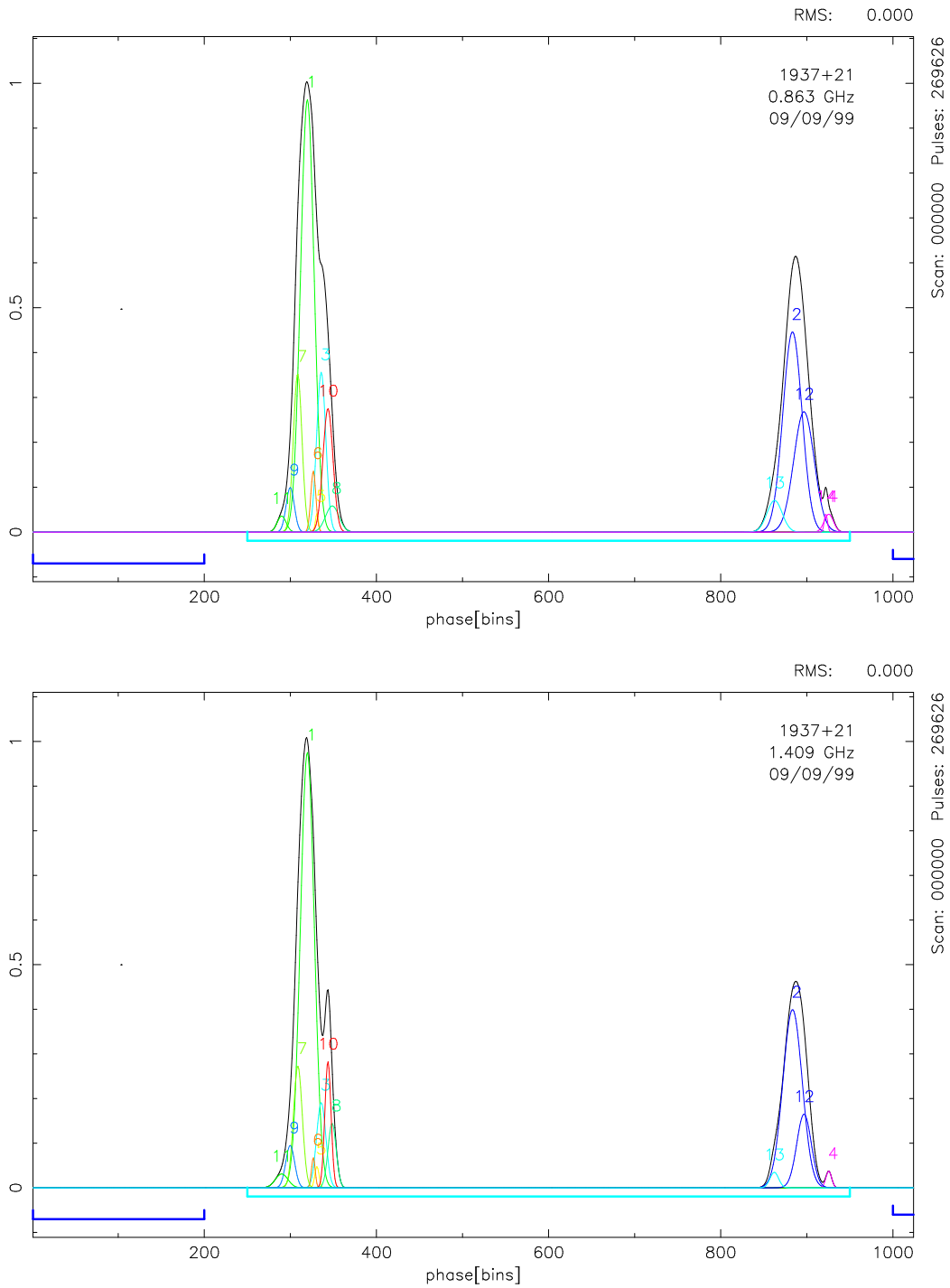


Figure 2.5: Gaussian templates for PSR J1939+2134 at 863 MHz (top) and 1410 MHz (bottom) in black, overlaid on their numbered components. The main pulse peaks of the lower-frequency template are merged together, and it needs an extra component to be added when adapted from the higher-frequency template.

2.2.3 Adaptation of Gaussian templates across a narrow frequency range

As mentioned above, PSR J1022+1001 is subject to scintillation which can give its profile an instantaneous SNR that varies significantly with observing frequency. Since all constituent frequencies were weighted equally when creating each profile, broad-bandwidth profiles could be somewhat diluted by this. The significant change in the profile as a function of frequency might also lead to these profiles differing from a template fitted to a profile with constant SNR. To preserve timing quality, narrow-bandwidth profiles were created that would have a more consistent SNR across their frequency range, and these were compared to the full-bandwidth profiles originating from the same data. The sub-band profiles would give a higher error-weighted residual RMS in a timing fit than the corresponding full-bandwidth ones, but their greater number would compensate in the accuracy of the fitted parameters, as long as the TOA uncertainties were accurately represented and used as weights in the fit.

Significant change in the profile of PSR J1022+1001 over a small frequency range necessitated the adaptation of its template over 160 MHz in bandwidth. The sub-band profile bandwidth was 7 MHz for Effelsberg data and 8 MHz for Parkes and Westerbork, and a template was created approximately every 8 MHz across the total bandwidth of the observations (sub-bands at similar frequencies from different telescopes used common templates). Because of the number of profiles to be created, and the relatively small change across the bandwidth, an automatic fitting procedure was employed. BFIT was first used to fit Gaussian templates to two high-SNR Parkes profiles of significantly different shape, each template containing 5 components with central positions common to the two (Figure 2.6). These ‘extreme’ profiles had central observing frequencies of 1321 and 1425 MHz respectively, and each had a bandwidth of 8 MHz. The corresponding extreme templates were scaled by setting their maximum intensity values to 1.

A weighted sum of the two corresponding extreme templates was then fitted to a high-SNR mean profile in each sub-band and full band, on the assumption that the profile evolved smoothly between them as frequency changed. This method was later used to characterise the profile shape of PSR J1022+1001, and is further detailed in §3.3.1.

The resulting templates are shown over the bandwidth of Parkes observations in Figure 2.7, overlaid on the high-SNR error-weighted mean profiles to which they were fitted. The relative height of the two main pulse components changes smoothly in both profiles and templates as frequency increases. Any change in the separation of the profile peaks is almost imperceptible, and the overall shapes of the profiles appear to be adequately represented across the total observation band by a weighted sum of the two basis profiles. The leading profile component, however, is less well approximated by the templates, reflecting the profile differences seen over time and demonstrating the difficulty in capturing it using a combination of only two modes. No jumps were required between the sub-bands, as when fitted they made a negligible difference to the timing results. Only small jumps between the different telescopes were needed (see §2.2.1). The sub-bands also produced slightly smaller parameter errors in timing than did the full bands (see §2.3.1). Gaussian template adaptation over a frequency range of ~ 100 MHz seems to produce aligned TOAs and accurate timing.

2.3 Timing solutions

TOAs were created from profiles of PSR J1713+0747, PSR J1857+0943 and PSR J1939+2134 using Effelsberg data, and for profiles of PSR J1022+1001 using Effelsberg, Parkes and Westerbork data. Those from Effelsberg were produced using its own software, while the rest were produced using PSRCHIVE. These were combined with pre-existing TOAs acquired from Arecibo, Jodrell Bank, Nançay, Parkes and Westerbork. Each TOA had an associated uncertainty based solely on

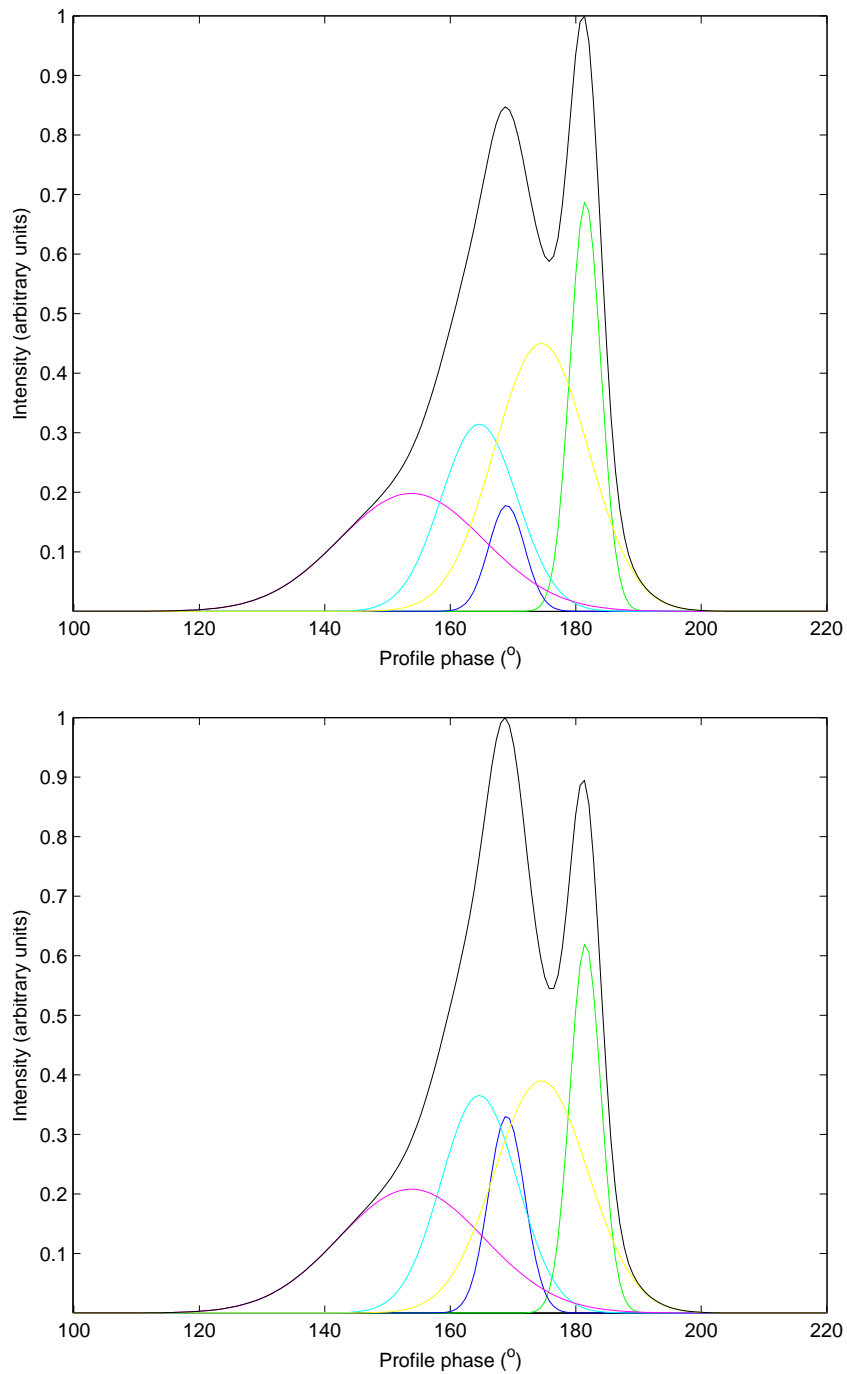


Figure 2.6: The two extreme Gaussian templates that were fitted in a weighted sum to profiles of PSR J1022+1001 (black), overlaid on their components (colour). The upper and lower templates were produced by fits to profiles from Parkes at central observing frequencies of 1321 and 1425 MHz respectively, chosen for their significantly different shapes.

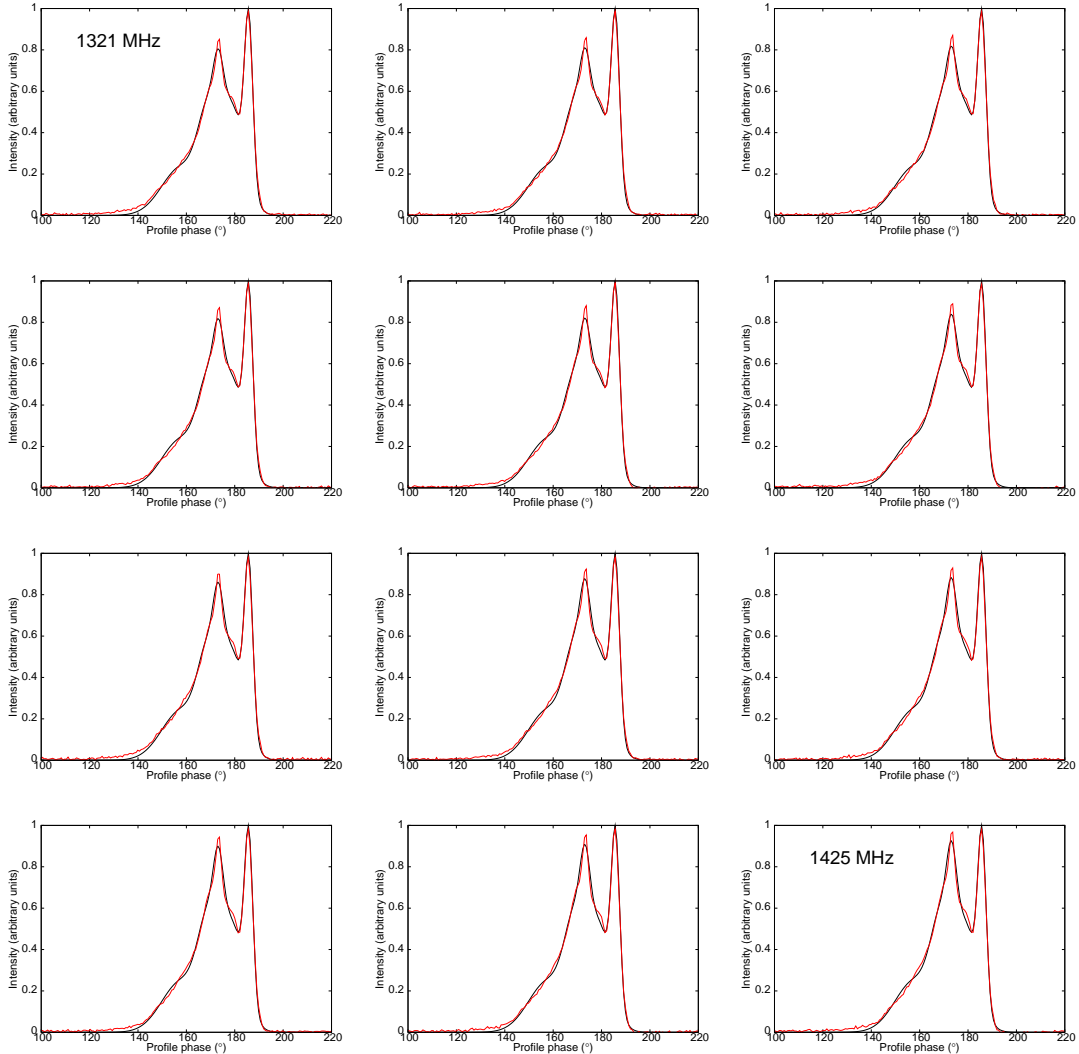


Figure 2.7: Overlaid Gaussian templates (black) and high-SNR error-weighted mean profiles (red) of PSR J1022+1001 from Parkes, as a function of frequency from 1321 to 1425 MHz. The smooth change in the relative height of the two main pulse components can be seen. Each template is a weighted sum of the two extreme templates in Figure 2.6, with the weightings determined by fits to the corresponding profiles. Frequency increases from left to right and from top to bottom. Adjacent templates are separated by 8 MHz, except for the sixth and seventh, which are separated by 24 MHz.

template-matching. The full set of TOAs from each pulsar was fitted, with error-weighting, to a model of the pulsar system using the TEMPO2 timing package, with jumps fitted between the different telescopes' data (see § 1.2.3–1.3.1). No jumps were used between different observing frequencies at the same telescope. The 2006 DE414 Solar System ephemeris¹ was used for all pulsars. The derived system parameters are presented below, with one-sigma errors on the final decimal places in brackets (see § 1.2.3), and are accompanied by information about each TOA set.

Since timing residuals often have a greater spread than their uncertainties imply, the uncertainties of these parameters need to be larger than is initially given by the timing analysis in order to be accurate. For this work, it was assumed that excess spread resulted from some source or sources of error independent of the template-matching error. For each pulsar, a constant additional uncertainty, E_{quad} , was added in quadrature to all the TOA uncertainties from a single telescope (see § 1.2.3). Its value was set such that the reduced chi-squared of the residuals from that telescope became equal to 1 when its TOAs were fitted alone, where this reduced chi-squared was defined as:

$$\chi_r^2 = \frac{1}{N_{TOA} - N_{par} - 1} \sum_{i=1}^{N_{TOA}} \frac{r_i^2}{(\delta t_i)^2 + E_{quad}^2} \quad (2.2)$$

where N_{TOA} is the number of TOAs used in the fit, N_{par} is the number of model parameters fitted using the TOAs, i is an integer indicating TOA number from 1 to N_{TOA} and r and δt are, respectively, the post-fit residuals and the uncertainties associated with the TOAs. Once the TOAs from all telescopes had been combined, a further E_{quad} was added in quadrature to all the TOAs uniformly, to make $\chi_r^2 = 1$ for the full TOA set. The TOA and parameter uncertainties were then considered to be accurately represented. This relies on the assumption that the unmodelled uncertainties are constant in time and independent of template-

¹DE414 was published by the National Aeronautics and Space Administration's Jet Propulsion Laboratory: ftp://naif.jpl.nasa.gov/pub/naif/generic_kernels/spk/planets/a_old_versions

	Arecibo	Effelsberg	Jodrell	Nançay	Parkes	Westerbork
PSR J1022+1001						
(full bands)	-	2.53	-	-	1.88	1.00
(sub-bands)	-	0.60	-	-	2.18	0.60
PSR J1713+0747	-	0.85	4.04	-	0.96	0.78
PSR J1857+0943	2.98	1.15	-	-	1.19	-
PSR J1939+2134	-	1.48	-	1.38	-	2.51

Table 2.1: E_{quad} values, in μs , used to increase uncertainties associated with the TOAs from each telescope and each pulsar.

matching error, which is not necessarily true. However, it is an unbiased way to account for unmodelled errors about which nothing is a priori known. It changes the fitted parameters, as well as their uncertainties, because it alters the relative weightings of the TOAs in the fit. The final values of E_{quad} for each telescope and pulsar are shown in Table 2.1.

The RMS of the error-weighted residuals after the addition of E_{quad} , and the value of χ_r^2 for all TOAs before the addition of E_{quad} , is listed with the timing parameters for each pulsar. The final residuals are also shown.

2.3.1 Timing of PSR J1022+1001

Short integrations of around 10 minutes were used to form TOAs for PSR J1022+1001 in order to prevent SNR loss due to scintillation, and all were produced with Gaussian templates. The timing solutions with full bands and sub-bands are presented for comparison in Table 2.2, with the residuals shown in Figure 2.8. All TOAs used came from profiles around 1400 MHz, so DM was not fitted. Proper motion in declination was not fitted because the pulsar’s position close to the ecliptic plane currently prevents a measurement accurate enough to be inconsistent with zero. The slightly smaller parameter uncertainties yielded by the sub-bands demonstrate that narrowband timing is effective for PSR J1022+1001.

Parameter	Full-bandwidth TOAs	Sub-band TOAs
Time span of observations (yrs)	12.08	12.08
Number of TOAs	1804	7739
Error-weighted residual RMS (μs)	3.74	5.47
χ_r^2 without E_{quad}	1.43	1.16
Right ascension (h:m:s)	10:22:58.0062 (13)	10:22:58.0058 (10)
Declination ($^{\circ}$:':")	+10 : 01 : 52.77 (5)	+10 : 01 : 52.76 (4)
Spin frequency (s^{-1})	60.77944798776623 (19)	60.77944798776615 (14)
Frequency derivative (s^{-2})	$-1.60096 (3) \times 10^{-16}$	$-1.60097 (3) \times 10^{-16}$
Reference epoch (MJD)	52754	52754
DM (cm^{-3} pc)	-	-*
Proper motion (RA) ($mas\ yr^{-1}$)	-17.16 (4)	-17.17 (3)
Parallax (mas)	2.10 (30)	1.95 (19)
Binary model	BT	BT
Binary orbital period (days)	7.80513028244 (14)	7.80513028255 (10)
Epoch of periastron (MJD)	52759.96990 (30)	52759.96964 (16)
Projected semimajor axis (lt-s)	16.76541623 (14)	16.76541620 (10)
Longitude of periastron ($^{\circ}$)	97.742 (11)	97.732 (8)
Orbital eccentricity	$9.7241 (15) \times 10^{-5}$	$9.7234 (11) \times 10^{-5}$

Table 2.2: Fitted system parameters of PSR J1022+1001 when timed with Gaussian templates at Effelsberg, Parkes and Westerbork using full bands and sub-bands.

* A fixed value of $DM = 10.2521 (1) cm^{-3} pc$ was used (Hotan et al. 2006).

The sub-bands also give a smaller reduced chi-squared value than the higher-SNR full bands, as would be expected if the excess variation were independent of profile SNR. Smaller values of E_{quad} were required in the sub-bands for Effelsberg and Westerbork and a slightly larger one needed for Parkes, suggesting that the sub-band templates may, overall, fit profiles slightly better than the full-bandwidth ones (Table 2.1). The sub-band E_{quad} values for Effelsberg and Westerbork were the lowest of any of the pulsars timed.

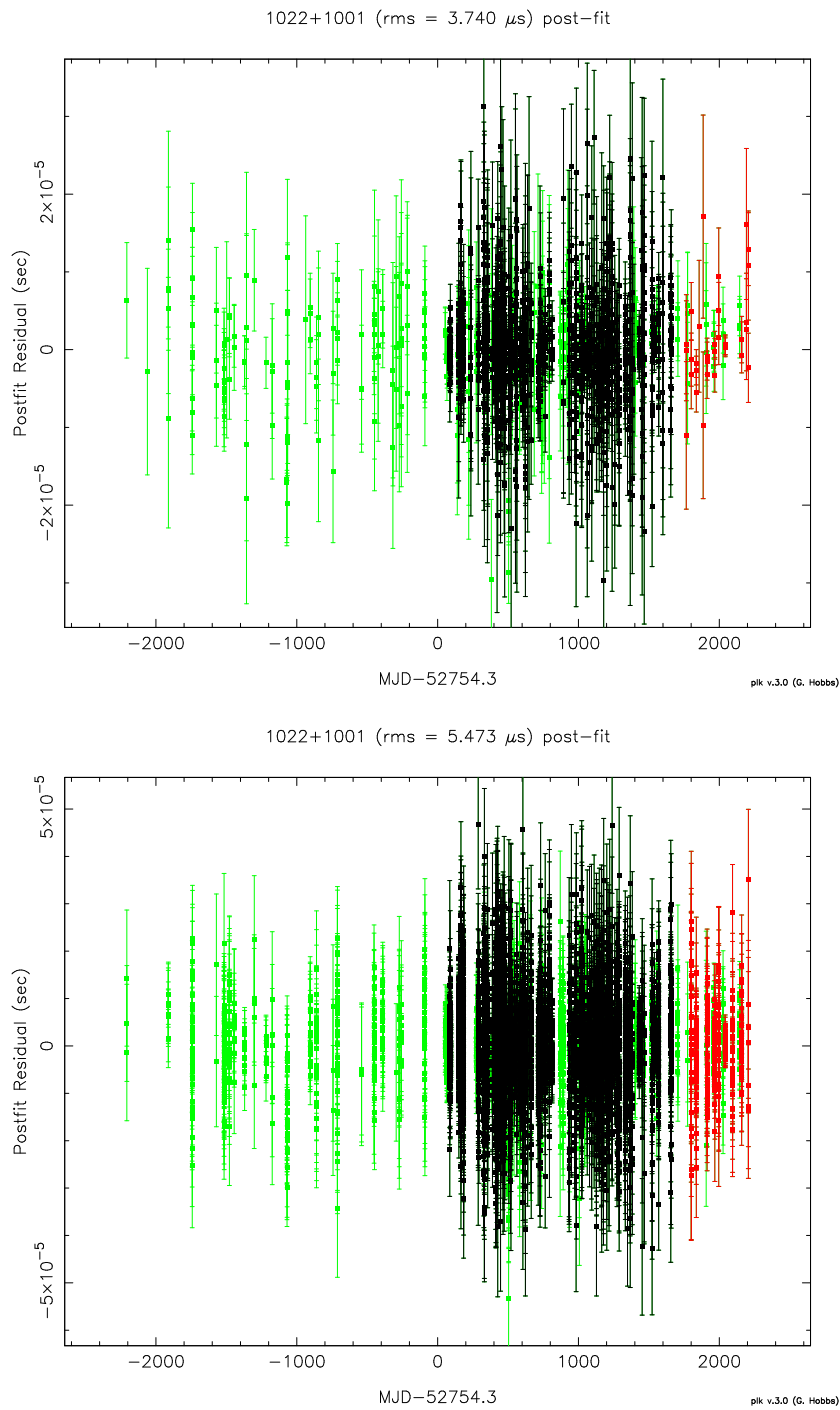


Figure 2.8: Timing residuals for PSR J1022+1001 when timed with Gaussian templates using full bands (top) and sub-bands (bottom). Effelsberg is in green, Parkes in black and Westerbork in red.

2.3.2 Timing of PSR J1713+0747

Short integrations produced the best timing results for PSR J1713+0747, resulting in smaller parameter uncertainties and values of χ_r^2 and E_{quad} than longer ones. The shortest available, which were between 1 and 15 minutes in length, were used for Effelsberg data. The results with these analytically timed TOAs are shown in comparison to those using all TOAs in Table 2.3. The residuals appear largely uncorrelated, but there is clear structure visible in the early Effelsberg and late Jodrell TOAs (Figure 2.9), and values of χ_r^2 are well above 1. Some of the parameters do not agree between the analytic and overall fits to within their uncertainties, hinting that some underestimation of error remains. The TOAs were from around 1400 MHz, with the exception of eleven from 840 MHz at Westerbork, so the Westerbork TOAs were timed alone to determine the pulsar’s DM.

2.3.3 Timing of PSR J1857+0943

Medium-length integrations, of between 15 and 45 minutes, produced the best timing results for Effelsberg observations of PSR J1857+0943. The results with these analytically timed TOAs are shown in comparison to those using all TOAs in Table 2.4. These residuals have the lowest reduced chi-squared values of any of the pulsars timed, but structure is still apparent over a long time span (Figure 2.10). The shorter data set from Effelsberg alone produced less obviously correlated residuals, but gave larger uncertainties on the pulsar system parameters. These may still be underestimated as the parameter values do not all agree between the analytic and overall fits. This may be because the additional, unmodelled sources of uncertainty are assumed to be uncorrelated in time, even though the residual structure shows that they are not. The TOAs were from around 1400 MHz, apart from four from 863 MHz and two from 2695 MHz at Effelsberg. The Effelsberg TOAs, produced using Gaussian templates, were used by Champion et al. (2010) in the measurement of the masses of planets in the Solar System. All the TOA

Parameter	Analytic-fit TOAs only	All TOAs
Time span of observations (yrs)	10.56	12.59
Number of TOAs	575	1193
Error-weighted residual RMS (μs)	1.04	1.32
χ_r^2 without E_{quad}	2.61	4.33
Right ascension (h:m:s)	17:13:49.5310560 (30)	17:13:49.5310465 (16)
Declination ($^{\circ}$:':")	+07:47:37.51751 (8)	+07:47:37.51757 (5)
Spin frequency (s^{-1})	218.81184049976116 (17)	218.81184049976039 (13)
Frequency derivative (s^{-2})	$-4.08350 (3) \times 10^{-16}$	$-4.08365 (3) \times 10^{-16}$
Reference epoch (MJD)	52659	52659
DM ($cm^{-3} pc$)	-	15.99013 (11) *
Proper motion (RA) ($mas yr^{-1}$)	4.950 (10)	4.909 (8)
Proper motion (dec.) ($mas yr^{-1}$)	-3.890 (30)	-3.899 (17)
Parallax (mas)	1.30 (20)	0.90 (14)
Binary model	DD	DD
Sine of inclination angle	0.71 (9)	0.84 (6)
Binary orbital period (days)	67.8251309180 (30)	67.8251309247 (14)
Epoch of periastron (MJD)	52743.677 (7)	52743.665 (4)
Projected semimajor axis (lt-s)	32.342408 (7)	32.342417 (3)
Longitude of periastron ($^{\circ}$)	176.310 (40)	176.246 (18)
Orbital eccentricity	$7.4933 (6) \times 10^{-5}$	$7.4938 (4) \times 10^{-5}$
Companion mass (M_{\odot})	2.2 (12)	0.8 (4)

Table 2.3: Fitted system parameters of PSR J1713+0747 when timed with Gaussian templates at Effelsberg, and with high-SNR templates at Jodrell Bank, Parkes and Westerbork, using full bands.

* DM fitted using Westerbork TOAs alone.

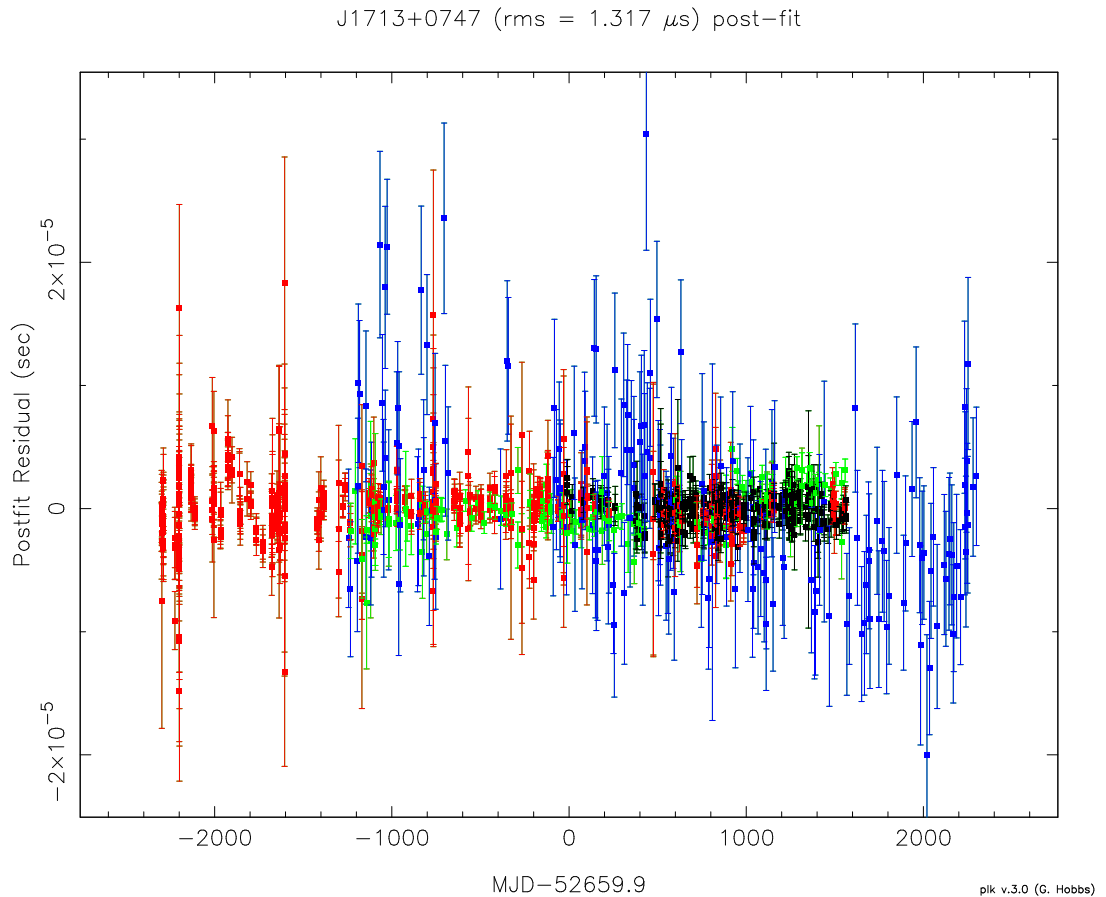


Figure 2.9: Timing residuals for PSR J1713+0747 when timed with Gaussian and high-SNR templates using full bands. Effelsberg is in red, Jodrell in blue, Parkes in black and Westerbork in green.

uncertainties from PSR J1857+0943 used in that work were ‘whitened’, based on the correlation of their associated residuals, in an attempt to make a fairer estimate of their values.

2.3.4 Timing of PSR J1939+2134

Short integrations of 1 to 15 minutes were used from Effelsberg observations of PSR J1939+2134. Strong signals, such as are obtained from this pulsar, can cause artificial intensity dips to be recorded on both sides of the pulse when the signal is digitised, and this effect is minimised with short integrations as the

Parameter	Analytic-fit TOAs only	All TOAs
Time span of observations (yrs)	10.29	21.30
Number of TOAs	96	406
Error-weighted residual RMS (μs)	1.85	2.71
χ_r^2 without E_{quad}	1.04	1.15
Right ascension (h : m : s)	18:57:36.392930 (40)	18:57:36.392908 (6)
Declination ($^{\circ}$: ' : ")	+09 : 43 : 17.27790 (70)	+09 : 43 : 17.27643 (17)
Spin frequency (s^{-1})	186.4940815201750 (30)	186.4940815201699 (5)
Frequency derivative (s^{-2})	$-6.20487 (16) \times 10^{-16}$	$-6.20462 (3) \times 10^{-16}$
Reference epoch (MJD)	50326	50326
DM ($\text{cm}^{-3} \text{pc}$)	13.2939 (8)	13.2939 (8)
Proper motion (RA) (mas yr^{-1})	-2.710 (80)	-2.667 (12)
Proper motion (dec.) (mas yr^{-1})	-5.83 (14)	-5.49 (3)
Parallax (mas)	-	-0.6 (5) *
Binary model	DD	DD
Sine of inclination angle	0.9999 (6)	0.9986 (11)
Binary orbital period (days)	12.327240 (110)	12.327179 (19)
Epoch of periastron (MJD)	50328.180 (20)	50328.183 (5)
Projected semimajor axis (lt-s)	9.2307834 (12)	9.2307806 (7)
Longitude of periastron ($^{\circ}$)	276.90 (60)	276.94 (13)
Orbital eccentricity	$2.129 (14) \times 10^{-5}$	$2.165 (8) \times 10^{-5}$
Companion mass (M_{\odot})	0.10 (5)	0.25 (4)

Table 2.4: Fitted system parameters of PSR J1857+0943 when timed with Gaussian templates at Effelsberg, and with high-SNR templates at Arecibo and Parkes, using full bands.

* Parallax fitted only when using all TOAs.

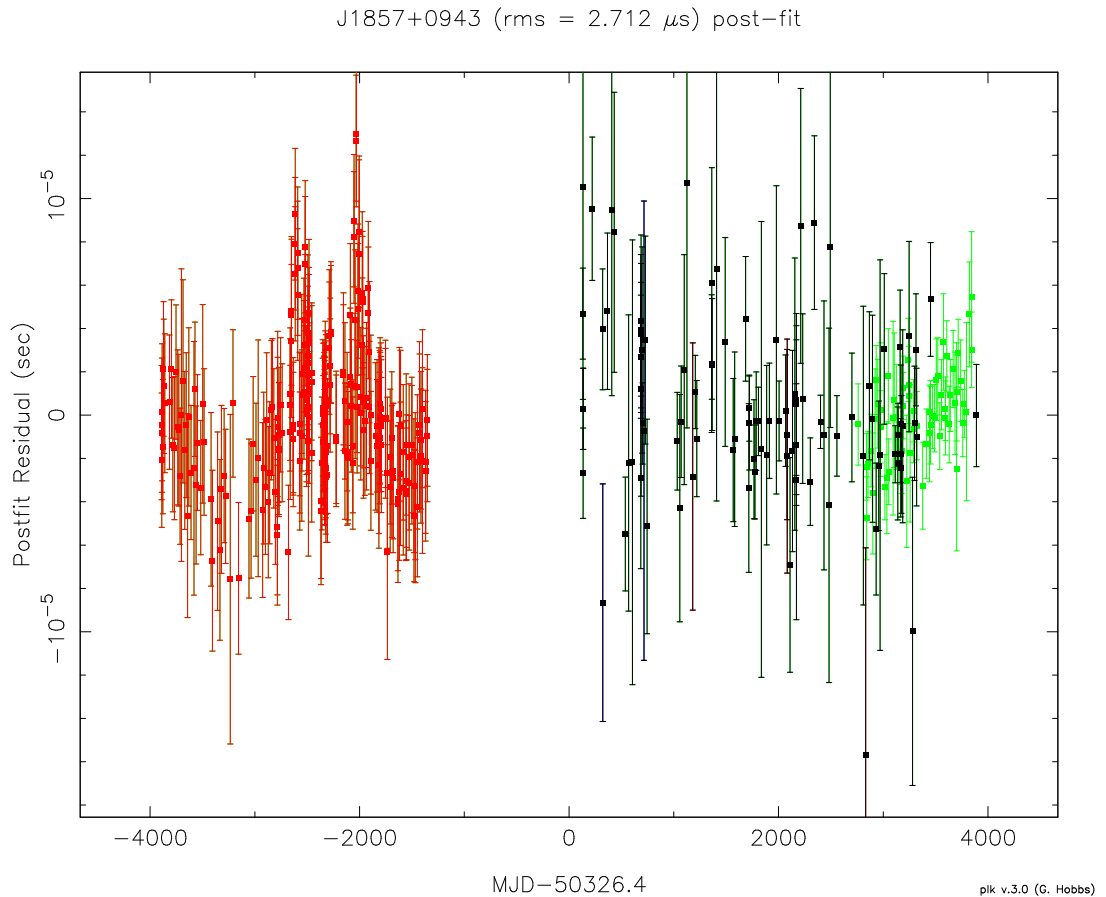


Figure 2.10: Timing residuals for PSR J1857+0943 when timed with Gaussian and high-SNR templates using full bands. Arecibo is in red, Effelsberg in black and Westerbork in green.

folded pulse has a lower SNR (Jenet & Anderson 1998). Shorter integrations of PSR J1939+2134 provided marginally better timing results, but all instrumental errors and template inaccuracies in the TOAs of this pulsar are dominated by timing noise and propagational effects (Verbiest et al. 2009; You et al. 2007). The results of these analytically timed TOAs are shown in comparison to those using all TOAs in Table 2.5. Its residuals are small, but are predominantly the result of structure (Figure 2.11), giving rise to very large reduced chi-squared values with either TOAs produced with analytic templates or all TOAs (Table 2.5). The smaller value from the Effelsberg data alone is likely due its shorter time span. A second time derivative of spin frequency made little difference to the residuals

and so was not used, but three derivatives of DM were fitted in order to account for Westerbork TOAs from around 840 and 2278 MHz, which were difficult to reconcile with the other TOAs from around 1400 MHz. Rotational instability and variable DM both appear to afflict PSR J1939+2134. Unsurprisingly, most of the system parameters did not concur between the analytic and overall timing solutions to within their uncertainties, particularly spin frequency and spin-down rate. A number of higher time derivatives of spin frequency might help, but could also be highly degenerate with other fitted parameters. The timing quality of the pulsar is still relatively good among MSPs due to the strength of its signal, but it has reached a level where further refinement will require a very long, multi-frequency data set. Nevertheless, the residuals from different telescopes, but similar frequencies, largely followed the same patterns over time.

Parameter	Analytic-fit TOAs only	All TOAs
Time span of observations (yrs)	11.22	11.22
Number of TOAs	792	1126
Error-weighted residual RMS (μs)	1.33	1.36
χ_r^2 without E_{quad}	27.03	48.22
Right ascension (h:m:s)	19:39:38.561195 (3)	19:39:38.561186 (3)
Declination ($^{\circ}$:':")	+21 : 34 : 59.12846 (5)	+21 : 34 : 59.12842 (5)
Spin frequency (s^{-1})	641.9282342779965 (4)	641.9282342779220 (40)
Frequency derivative (s^{-2})	$-4.331082 (1) \times 10^{-14}$	$-4.331015 (6) \times 10^{-14}$
Reference epoch (MJD)	52409	52409
DM ($\text{cm}^{-3} \text{pc}$)	-	71.02579 (15) *
DM derivative ($\text{cm}^{-3} \text{pc yr}^{-1}$)	-	$-0.00170 (9) *$
DM second derivative ($\text{cm}^{-3} \text{pc yr}^{-2}$)	-	0.00025 (3) *
DM third derivative ($\text{cm}^{-3} \text{pc yr}^{-3}$)	-	$-0.0000020 (8) *$
Proper motion (RA) (mas years^{-1})	0.150 (10)	0.085 (9)
Proper motion (dec.) (mas years^{-1})	$-0.353 (15)$	$-0.380 (12)$
Parallax (mas)	1.00 (30)	0.81 (18)

Table 2.5: Fitted system parameters of PSR J1939+2134 when timed with Gaussian templates at Effelsberg, and with high-SNR templates at Nançay and Westerbork, using full bands.

* DM and its derivatives fitted only when using all TOAs.

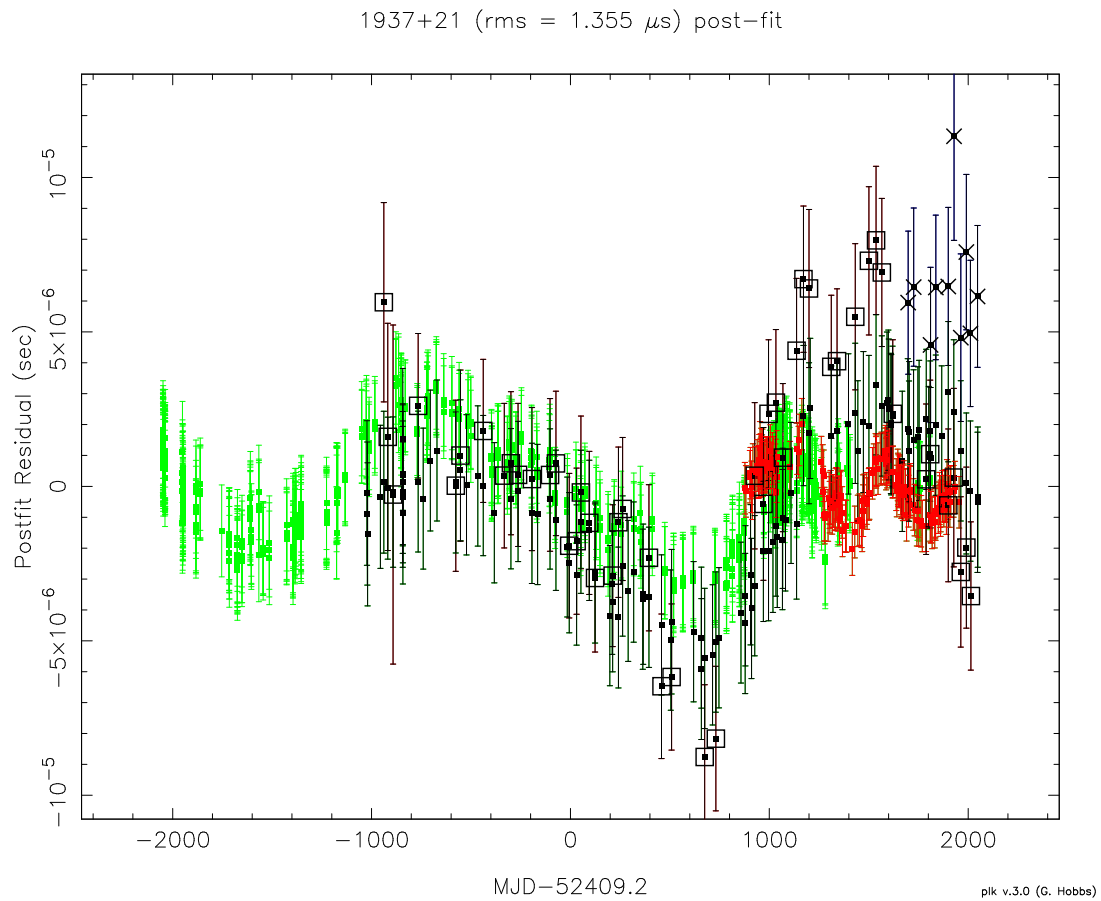


Figure 2.11: Timing residuals for PSR J1939+2134 when timed with Gaussian and high-SNR templates using full bands. Effelsberg is in green, Nançay in red and Westerbork in black; squares and crosses indicate TOAs from around 850 and 2280 MHz respectively, while the other TOAs are from around 1400 MHz.

3

Apparent pulse profile instabilities in PSR J1022+1001

The stability of integrated pulse profiles is a fundamental assumption of pulsar timing (see § 1.2.3), according to which the measured shape of each profile from which a TOA is obtained should be altered only by time-varying random noise that is uncorrelated between its phase bins. If the assumption of stability is violated and the profile shape of a pulsar instead shows bin-correlated variation, so that it is not always a scaled and shifted version of a single template (see Equation 1.4), any TOAs obtained from matching its profiles to a fixed template will be affected and additional scatter will be introduced into the resultant timing residuals. Measurements made from these residuals will then have greater associated uncertainties than they would in the absence of bin-correlated variation. If the variation is also correlated in time between profiles as well as between bins, the residuals may contain patterns which mask or imitate red noise from other sources. The additional residual scatter will not be attributable to the usual instrumental and environmental noise, nor to actual rotational instability in the pulsar.

Profile shape changes can limit the accuracy of pulsar timing. Where intrinsic

to a pulsar, they may restrict its usefulness in high-precision timing. Where extrinsic, they may indicate propagation effects or systematic instrumental errors which will affect the precision of all pulsar timing to some extent. There is no consensus in published work as to whether intrinsic change in profiles integrated over more than 10^4 periods has been observed in MSPs. This chapter examines profile stability, focusing on PSR J1022+1001, a pulsar which has previously been said to show variation.

3.1 The curious case of PSR J1022+1001

3.1.1 Findings of previous work

PSR J1022+1001 is an unusual pulsar. Its spin period of 16.5 ms places it among the slower MSPs, but, with a slow rate of period increase and a relatively strong radio signal at the Earth, it has been shown to yield high timing accuracy (Hotan et al. 2004; Hotan et al. 2006; Verbiest et al. 2009), and is the longest-period pulsar currently used in PTAs (Yardley et al. 2010). The most striking feature of PSR J1022+1001 is the rapid shape evolution of its double-peaked pulse profile as a function of observing frequency (Camilo 1995; Kramer et al. 1999; Ramachandran & Kramer 2003), a property atypical of MSPs (Xilouris et al. 1998). More unusually still, evidence has been presented that the shape of the integrated profile, folded modulo the rotational phase over more than 10^4 periods, varies intrinsically with time (Camilo 1995; Kramer et al. 1999; Ramachandran & Kramer 2003). A separate study, however, concluded that there was no evidence of significant variation and that any apparent changes could be explained entirely by effects extrinsic to the pulsar, such as interstellar scintillation and dispersion and instrumental polarisation calibration error (Hotan et al. 2004). The significance of the latter effect comes from the high degree of polarisation of the profile (see §3.1.2) (Xilouris et al. 1998; Ord et al. 2004).

3.1.2 Possible causes of apparent profile variation as a function of time

Any intrinsic explanation for profile instability must use variation in either the mechanism or propagation of emission, both of which depend on the nature of the pulsar magnetosphere. Since this is not well understood (see § 1.1), such theories are necessarily vague. Ramachandran & Kramer (2003) suggested that it may be related to the PA curve of PSR J1022+1001, in which a section corresponding to the leading part of the pulse appears to be offset from the rest (see Figure 3.1). This could be explained either by emission from two different heights in the magnetosphere, where magnetic field sweep-back and beam aberration would result in different angles of emission to the line of sight, or by penetration of the beam through a sheet of return current, which is the particle flow balancing the polar cap currents responsible for emission (Hibschman & Arons 2001). In either case, the dynamics of the different magnetospheric regions probed could perturb the pulse profile, but current explanations go no deeper than this.

Extrinsically, interstellar diffractive scintillation is capable of translating the frequency dependence of the profile shape of PSR J1022+1001 into a time dependence. It is known to affect the pulsar’s signal strongly (Hotan et al. 2004), and can, over time, change the relative brightness of the pulsar at different frequencies within the band, ‘bringing out’ the subtly different pulse shapes therein. The characteristic scintillation timescale and bandwidth of PSR J1022+1001 at an observing frequency of 1400 MHz should be roughly 45 minutes and 40 MHz respectively, according to the NE2001 electron density model (Cordes & Lazio 2003; Cordes & Lazio 2003)¹, so, although this effect is not smoothed out over the duration of a typical observation, it can largely be mitigated by examining profiles of bandwidth $\lesssim 10$ MHz. Actual scintillation measurements of PSR J1022+1001

¹Values for scintillation timescale and bandwidth were calculated using a tool provided by the United States Naval Research Laboratory: http://rsd-www.nrl.navy.mil/7213/lazio/ne_model/

at 685 MHz by You et al. (2007) give a timescale range higher than the model and a bandwidth range mostly higher than the model, so this may also be the case at 1400 MHz. DM changes could also alter the profile shape by causing it to be aligned incorrectly upon frequency-scrunching (see § 1.2.1). As with scintillation, the effect can be reduced by the use of profiles of bandwidth $\lesssim 10$ MHz.

Hotan et al. (2004) argued that the principal source of profile variation in PSR J1022+1001 is not in the radio signal at all, but is introduced by instrumentation during the measurement process. Imperfect polarisation calibration of receivers with linear feeds has been identified as a significant source of error in the total intensity of highly linearly polarised signals. The trailing component of the profile of PSR J1022+1001 has a high degree of linear polarisation (Figure 3.1), and would therefore be expected to show greater spurious variation than the rest of the profile, with its severity dependent on the receiver, recording system and calibration scheme used. Ord et al. (2004), with the same instrumentation used to make most of the observations analysed in § 3.2, employed a full calibration method, including a receiver model (see § 1.2.1), in polarimetric observations of 27 MSPs; they estimated that systematic changes occurring after the model was made could introduce errors of, at most, 2% in total intensity and 4% in linear and circular polarisation. Hotan et al. (2004) used the same equipment with simpler calibration when analysing PSR J1022+1001, correcting only for differential gain and phase between the feeds, but were slightly more optimistic in anticipating resultant errors of ~ 1 –2% in total intensity at pulse phases of high linear polarisation. Such variation should appear as a function of parallactic angle superimposed on a random fluctuation over time (van Straten 2004). Even with the most sophisticated calibration available, pulsar data still sometimes contain unexplained artefacts. Most of the data examined in § 3.2 were acquired with a 2-bit digitiser employing dynamic level setting to adjust its dynamic range continuously and separately for each feed. This can result in small changes to the differential gain of the feeds, which are not corrected because they

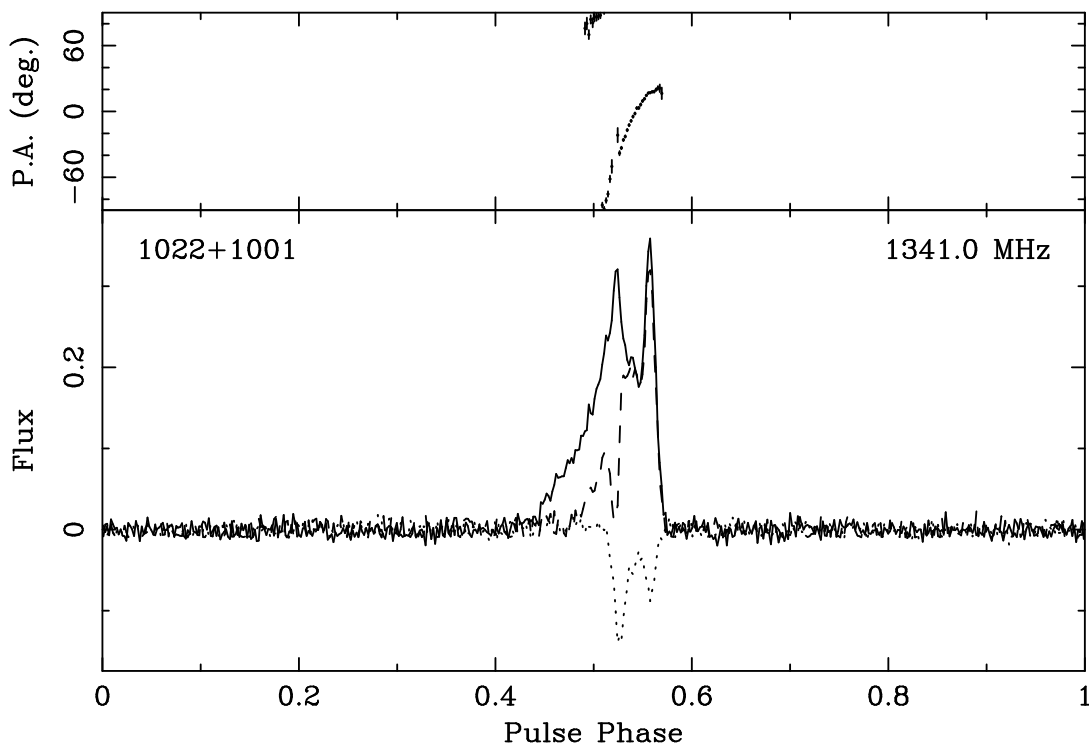


Figure 3.1: PA and polarisation profiles of PSR J1022+1001 at 1341 MHz from Parkes. The integration time is 27 minutes and the bandwidth is 48 MHz. Top window: PA as a function of profile phase. The jump in PA reported by Ramachandran & Kramer (2003) is visible from the raised data point at fractional pulse phase 0.525, PA -20° . Bottom window: polarisation profiles. The solid line is total intensity, the dashed line linearly polarised intensity and the dotted line circularly polarised intensity. The trailing component has a high degree of linear polarisation, which could lead to spurious variation in its total intensity relative to the rest of the profile as a result of imperfect polarisation calibration.

happen between calibrator observations (see § 1.2.1). Shape variation caused by this, and by other unmodelled instrumental effects, is thought to afflict polarised pulse profiles (van Straten 2010, personal communication).

3.2 A new analysis of PSR J1022+1001

There are now many more observations of PSR J1022+1001 than were available when the previous papers on the pulsar were written, allowing a rigorous statistical analysis of profile variation. In this new analysis, the methods previously used to assess variation were extended and some new techniques were used. Profiles were studied across broad and narrow bandwidths of frequency and over short integration times, partly to mitigate scintillation and partly because this is how Kramer et al. (1999) observed variation. The effects of calibration were investigated, as Hotan et al. (2004) considered them significant. The profiles' shapes were quantified, and they were timed with both fixed and adaptive templates. Data were taken from the same telescopes and instruments as in the previous papers.

3.2.1 Observations

The profiles analysed were the same as those used to time PSR J1022+1001 in §2 and were all coherently dedispersed. Data from the 100-m Effelsberg telescope were acquired over around 12 years between 1996 and 2009 with observations of varying duration and separation in time, 15–30 minutes every 20 days being typical. These measurements were recorded by the 4-bit Effelsberg-Berkeley Pulsar Processor (EBPP) mainly across a bandwidth of 56 MHz centred on 1410 MHz, with a smaller number of profiles taken over 56 MHz centred on 863 MHz and a handful taken over 112 MHz centred on 2695 MHz. Data from the 64-m Parkes telescope were taken over almost 5 years from 2003 to 2008, typically with a 1-hour observation every 15 days. The 2-bit Second Caltech-Parkes-Swinburne Recorder (CPSR2) mostly provided two 48-MHz-wide bands centred on 1341 and 1405 MHz, with a smaller number of profiles taken over one 48-MHz-wide band centred on 685 MHz. The Westerbork Synthesis Radio Telescope (WSRT), with an equivalent diameter of 96 m, yielded observations spanning more than 1 year

from 2008 to 2009, each lasting around 25 minutes and occurring about every 40 days. Data were stored by the 2-bit Pulsar Machine (PuMa) and its successor, the 8-bit PuMa-II, across a bandwidth of 160 MHz, centred on 1380 MHz. Since there were relatively few Westerbork observations, these were used only in the timing study.

3.2.2 Data reduction

As explained in §2.1.1, the band edges of the Parkes data were excised using PSRCHIVE. Noisy or defective individual frequency channels in the Effelsberg observations were found by eye and removed using Effelsberg software. The same software was used to scrunch the Effelsberg data into total intensity profiles of approximately 10 minutes' duration. Each profile was bin-scrunched to 899 phase bins, since this was a factor of the number of bins in the original profiles. The Parkes and Westerbork data were scrunched into profiles of about 10 minutes and exactly 512 bins using PSRCHIVE, the latter being sufficient to capture the pulse features of PSR J1022+1001. In the case of the Parkes data, PSRCHIVE also allowed a *scattered power correction* where deemed necessary (van Straten 2003), in which the profile is adjusted to correct for the digitisation distortions around the profile that can be introduced by the dynamic setting of instrumental signal recording levels that is employed at Parkes (Jenet & Anderson 1998).

All profiles were initially uncalibrated, and all had been recorded by linear receiver feeds. The Westerbork profiles did not have associated calibrator observations. Many of the Effelsberg profiles did have such observations, of an artificial, linearly polarised signal made just before or after the pulsar observations, so these were used to polarisation-calibrate those profiles with Effelsberg software, correcting for the differential gain of the receiver feeds (see §1.2.1). The uncalibrated profiles corresponding to the polarised ones were kept for comparison. Many of the Parkes profiles also had associated calibrator observations, and

so were similarly calibrated, but with correction for differential phase as well as gain, allowing profiles to be formed from the linearly and circularly polarised components of the pulsar signal if desired. The 1400-MHz Parkes data were acquired using two receivers at different times, known as *H-OH* and *multibeam*. A receiver model was created for the multibeam receiver by Kuo Liu using PSR J0437–4715, and this was used to further calibrate the relevant observations. This additional calibration was implemented using PSRCHIVE, and has been described by van Straten (2004) using the Parkes multibeam receiver as a demonstration. The H-OH receiver was not considered to need such calibration (van Straten 2008, personal communication). Profiles from the two receivers were generally analysed together, but could be separated as the receiver information was recorded within the archives. Differential gain and phase calibration is hereafter referred to as *simple calibration*, and calibration including receiver corrections as *full calibration*. Both calibrated and uncalibrated profiles were kept and analysed separately.

After calibration, the profiles were further scrunched into two groups of profiles originating from the same observations: *sub-band* profiles of 7 MHz in bandwidth for Effelsberg, 8 MHz for Parkes and 8.125 MHz for Westerbork, and profiles in *full bands* of the total observational bandwidth. Data from each telescope and, within this, profiles of different sub- and full bands, were generally analysed separately as independent data sets.

The appropriately calibrated and scrunched profiles were output as text files and analysed using scripts written within version R2009a of the MATLAB programming environment². More filters were applied at this stage to remove weak and corrupted profiles: profiles were included if they had a minimum peak SNR (ratio of maximum intensity to profile noise level) of 10, a separation between profile peaks of 9–15° (the correct value being approximately 12°) and an observational duration of between 5 and 15 minutes. The approximate peaks in each profile were calculated initially by finding the highest intensity value in the

²MATLAB[®] is produced by MathWorks[™]: <http://www.mathworks.com/products/matlab/>

profile, excluding a sufficient phase range around it and then finding the highest intensity value outside this range. The noise level in each profile, which was used as the uncertainty in the intensity of each bin, was taken to be the RMS of the off-pulse intensity values after subtracting a constant baseline to give a mean off-pulse intensity of zero (see Equation 1.3). The off-pulse region was taken to be everything outside a safe range around the approximate peak bins. It avoided the areas next to the pulse where digitisation distortions can occur. The ranges used to determine the approximate locations of the peaks and the off-pulse region were specific to PSR J1022+1001, but were made easily changeable within the MATLAB scripts, so that other profile shapes could be accommodated with a small amount of user intervention. After filtering, there were a total of several thousand Parkes profiles, several hundred Effelsberg profiles and around one hundred Westerbork profiles, calibrated in all bands, that were considered usable in the analysis of pulse shape variation.

The locations of the profile peaks, which were critical to the shape analysis (see § 3.3), were determined precisely by normalising all the profiles in each band and aligning them with one another, which involved recursively normalising and aligning them with their own error-weighted mean profile. The errors were those derived from profile noise (see Equation 1.3). To produce a reasonable initial error-weighted mean profile, the profiles were aligned by their approximate peaks and normalised by their summed intensities in the on-pulse region. Since each summed intensity had uncertainty based on that profile's noise level, the propagation of errors produced different uncertainty values in each bin of each normalised profile. Uncertainties in this, and subsequent, sections were propagated according to the equation:

$$\delta\left(u(w)\right) = \sqrt{\sum_{y=1}^{N_{var}} \left(\delta w_y \left|\frac{\partial u}{\partial w_y}\right|\right)^2} \quad (3.1)$$

where δu is the uncertainty in u , which is any function of multiple arbitrary variables w , each of which is indicated by y from 1 to N_{var} and has an uncertainty

of δw_y . Profile alignment down to the sub-bin level was accomplished using the frequency-domain method of Taylor (1992). This was implemented using MATLAB's inbuilt FFT function and a simple iterative procedure to converge on the most likely phase offset between an individual profile and the mean by matching the FFTs of the two (see §1.2.3). The method is the same as that used to obtain timing residuals by template-matching, and so also allowed profiles to be accurately shifted and scaled in intensity to match the mean. Although the profiles were not flux-calibrated and therefore of arbitrary intensity relative to one another, this alignment and normalisation permitted an assessment of where in profile phase excess variation might be occurring (see §3.6.3). The profiles were shifted by non-integral numbers of phase bins using the MATLAB function `RESAMPLE`, which employs a weighted sum of surrounding bins to estimate intensity values within each bin and applies an anti-aliasing finite impulse response filter (see e.g. Press et al. 1992, pp. 538–540) to the output in order to suppress artificial profile structure at high spatial frequencies. Interpolation accuracy is generally improved by using more bins in the weighted sum, and can be quantified by its effect on the RMS of a set of normally distributed random numbers. Simulations of such sets showed that the use of 30 bins resulted in an acceptable reduction of about 1% in RMS, so this value was used when aligning profiles. Once a set of profiles had been aligned with its mean, the mean was recalculated and the alignment process repeated. This was generally a convergent process, requiring only a few iterations before the profile phase shifts at each successive iteration became negligible. The final phase locations of the peaks were those found in the mean aligned profile at each frequency.

3.3 Evaluation of profile variation

3.3.1 Profile shape indicators

Three separate indicators were used to quantify the shape of PSR J1022+1001, in order to be as sensitive as possible to shape variation. The first was the *peak ratio*, R , used by Kramer et al. (1999) to define the double-peaked profile shape simply by the intensity ratio of its leading and trailing peaks:

$$R_i = \frac{P_{i,F}}{P_{i,B}} \quad (3.2)$$

where $P_{i,j}$ is the intensity of profile i in bin j and F and B are the bin numbers of the leading and trailing peak respectively. This quantity avoids the scaling problems of absolute flux calibration and variable pulse intensity and provides a consistency check between the profiles recorded by the different telescopes, but it is highly subject to random error as it uses only two phase bins.

The second indicator was the *area ratio*, A , the ratio of the integrated intensity of the leading component to that of the trailing one, using several phase bins around each peak:

$$A_i = \left(\sum_{j=F-M}^{F+M} P_{i,j} \right) / \left(\sum_{j=B-M}^{B+M} P_{i,j} \right) \equiv \frac{S_{i,F}}{S_{i,B}} \quad (3.3)$$

where M is an integer defining the width of the areas used ($2M + 1$ bins are used for each component) and S_F and S_B are the areas of the leading and trailing peak respectively. Areas of approximately 6.3° each in phase width were used (i.e. $M = 4$ for 512-bin profiles). This indicator offered the same advantages as the peak ratio while giving a higher SNR in the measurement of the relative strengths of the two components.

The uncertainties assigned to peak and area ratios were calculated by propagating the uncertainties in each bin of the unnormalised profiles (see Equation 3.1), which were each equal to RMS of the off-pulse intensity values. Respective noise errors in sub-bands and full bands are typically 9% and 4% of peak ratios

and 4% and 2% of area ratios, and were computed directly from the RMS of off-pulse intensity and therefore independently of the ratios themselves.

The third indicator was the *shape parameter*, s , which used the entire pulse to define a profile's shape more fully than the ratio indicators. It represented the shape as a weighted sum of two 'extreme' Gaussian templates (see Figure 2.6), based on high-SNR profiles selected from the available set as having very different peak and area ratios and each scaled to a maximum intensity of 1 (see §2.2.3). The shape of profile i was then represented by the weighting factor or *shape parameter*, s_i , which was the shape parameter value. The intensity of each observed profile, i , was described in each phase bin, j , as the linear combination of the two templates, T_1 and T_2 , plus a Gaussian random noise term, G_i :

$$P_{i,j} = s_i v_i T_{1,j} + (1 - s_i) v_i T_{2,j} + G_{i,j} \quad (3.4)$$

with a scaling factor v_i due to the arbitrary intensity scale of each profile. The extreme templates were formed from 5 Gaussian components each, with centres common to the two. For each observed profile, the parameter s was obtained by an iterative least-squares fit of Equation 3.4 over all phase bins, allowing a shift in phase between templates and profile.

Error estimates for the shape parameter were derived as a function of RMS off-pulse noise and shape parameter by using numerical simulations. Fake observed profiles were obtained by artificially adding random noise of various amplitudes to summed-template profiles with different values of s , and then recording the distribution of measured values of s when these fake profiles were fitted according to Equation 3.4. For the real profiles, values of s had typical uncertainties of 10–30% in sub-bands and 5–15% in full bands, the relatively high percentage errors reflecting the fact that a fractional change in peak or area ratio corresponds to a greater fractional change in s . Michael Kramer designed the shape parameter technique and wrote the programmes used to find its error distribution and to compute its value for a given profile.

3.3.2 Advantages and disadvantages of the shape indicators

In general, the simplicity of the shape indicators is both their strength and weakness. The peak and area ratios, and their uncertainties, are easy to calculate and use the strongest parts of the pulsar signal. Their usefulness, however, is restricted to profiles with at least two peaks.

The shape parameter benefits from the accuracy afforded by using the whole profile, and is an indicator readily transferable to other pulsars. Its assumption that profile variation can be described by a linear combination of its two extreme templates with fixed central components, however, prevents s -values from being comparable outside a fairly narrow frequency range around 1400 MHz. Even within this range, its value would become unpredictable if the real profile change could not be described by a linear combination of the two extremes, as would be the case, for instance, if profile component separation were to change. At some frequencies, many values of s came out at either 0 or 1, since these were its limits. This shows that there was profile variation outside the range of the extreme templates. These values were removed so that they did not dominate the rest.

All the indicators reduce profile shape from a parameter consisting of as many dimensions as there are profile bins to a parameter consisting of one dimension, so prior assumptions must be made and information is inevitably lost. The shape indicators were nevertheless consistent with one another and appeared to capture the essence of the shape changes of PSR J1022+1001, as the following sections demonstrate.

3.4 Evolution of profile shape as a function of observing frequency

3.4.1 Profile shape indicators as a function of frequency and their consistency between sets of observations

The peak ratio, area ratio and shape parameter demonstrate the strong dependence of profile shape on emission frequency observed by Kramer et al. (1999), Ramachandran & Kramer (2003) and Hotan et al. (2004). For each parameter, it is indicated by the error-weighted medians of the sets of values in each sub-band, which largely average out any time variations. Error-weighted median values, and their uncertainties, were computed according to the method of Müller (2000) as described by Ratel (2006), assuming that the sets from which they were derived were internally uncorrelated. The Parkes data, having the most profiles, provide the clearest results. Over a large frequency range, the unusual turnover of area ratio noted by Ramachandran & Kramer (2003) can be seen, after which the leading component grows relative to the trailing one as frequency increases (Figure 3.2). The slight offset between Parkes and Effelsberg data points, apparent around 1400 MHz in Figure 3.2, is due to the different numbers of bins used in calculating the peak areas of the different telescopes' profiles: this is a result of using an integral number of bins in each case (see § 3.2.2 and Equation 3.3). Around 1400 MHz, all three shape indicators show a positive correlation with frequency that is apparent over a range of $\lesssim 40$ MHz. They are largely consistent between uncalibrated, simply calibrated and fully calibrated profiles, but the effect of calibration is visible, most obviously in the shallowing of the trend in the lower sideband when full calibration is applied (Figure 3.3). Between sub-band central frequencies of 1321 and 1425 MHz, peak ratio increases by approximately 15 %, area ratio by around 13 % and shape parameter by about 0.4.

The Effelsberg profiles are less numerous, and so give larger uncertainties,

3.4: EVOLUTION OF PROFILE SHAPE AS A FUNCTION OF OBSERVING FREQUENCY

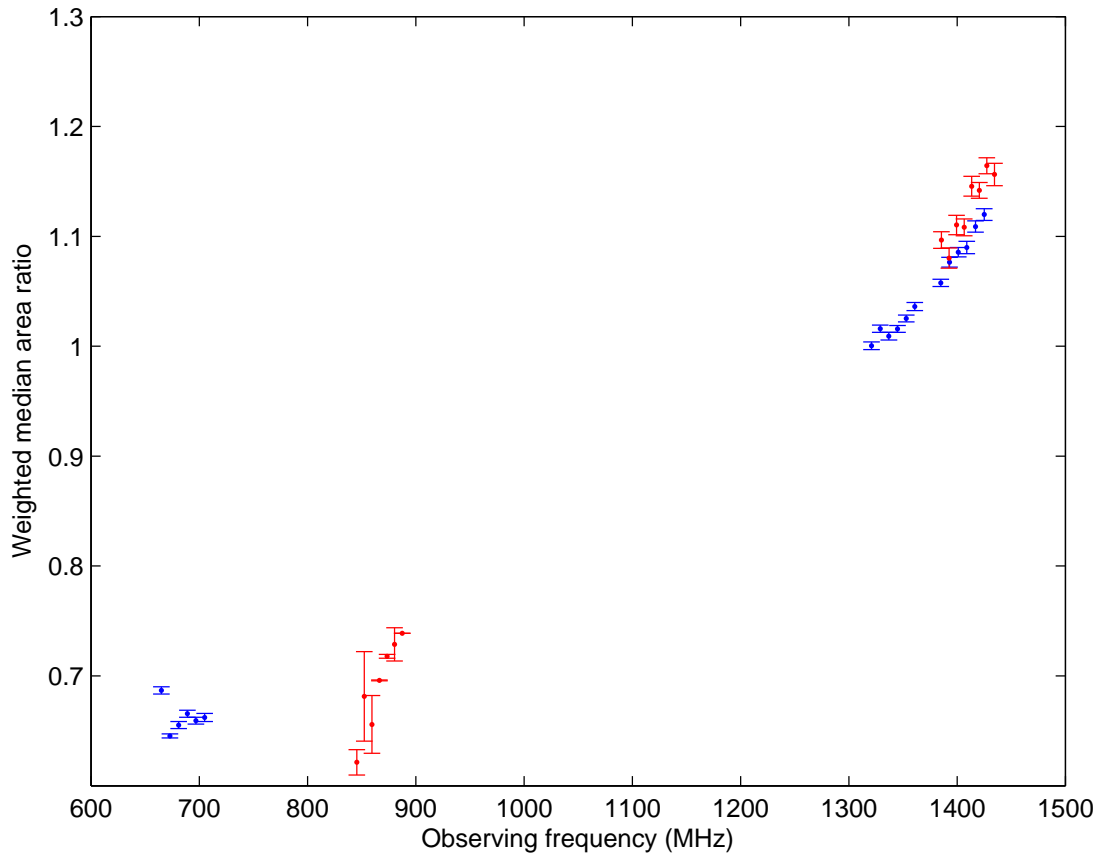


Figure 3.2: Evolution of area ratio for PSR J1022+1001 over a broad range of observing frequency, showing a turnover around 800 MHz followed by an increase. These values are error-weighted median values in sub-bands, all from simply calibrated profiles for consistency. The blue points are from Parkes and the red points are from Effelsberg. The slight offset between Parkes and Effelsberg points, apparent around 1400 MHz, is due to the different numbers of bins used in calculating the peak areas of the different telescopes' profiles.

but show the same trends. Their error-weighted median values are consistent with those of the Parkes profiles in peak ratio, slightly higher in area ratio and noticeably lower in shape parameter (Figure 3.4). This appears to show a small systematic difference between Parkes and Effelsberg profiles of PSR J1022+1001, visible when inspecting complete profiles but less evident around their peaks, and highlights the problem of subtle instrumental corruption of profiles.

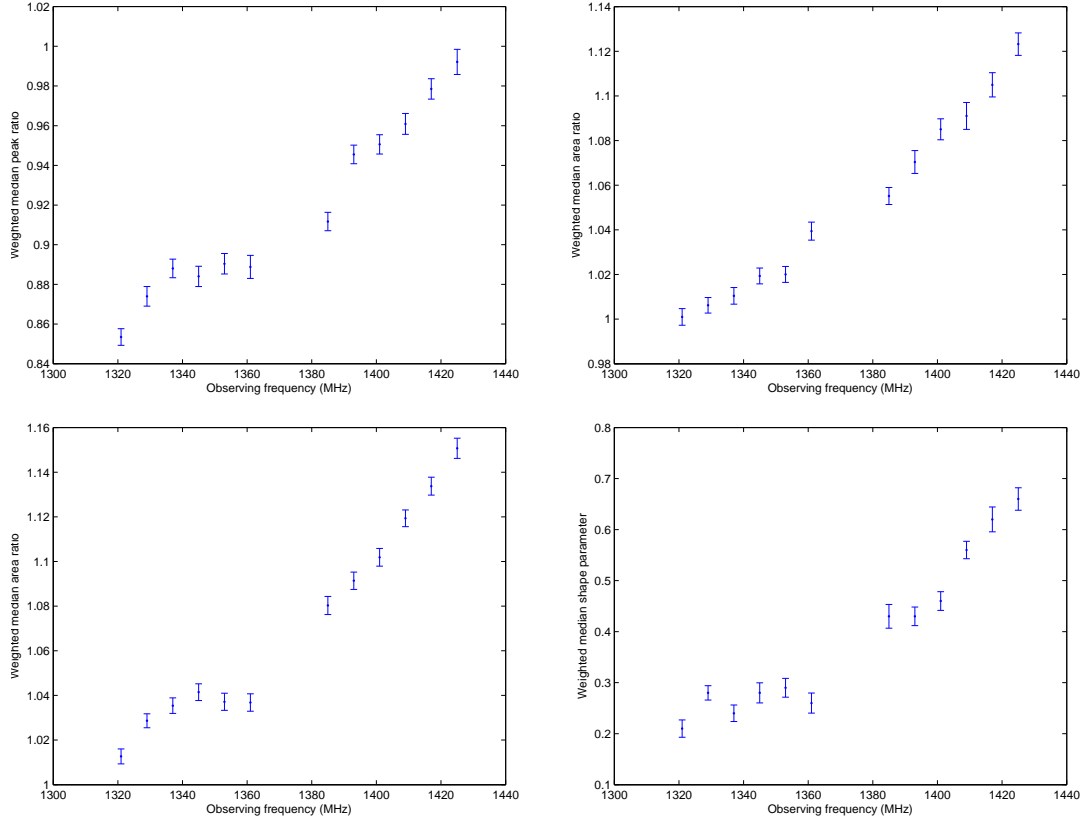


Figure 3.3: Evolution of all shape indicators as a function of frequency for PSR J1022+1001 in Parkes data around 1400 MHz. The panels show fully calibrated peak ratio (top left), simply calibrated area ratio (top right), fully calibrated area ratio (bottom left) and fully calibrated shape parameter (bottom right).

3.4.2 Absolute amplitudes of profile components as a function of frequency

As frequency increases around 1400 MHz, the profile shape change appears to be the result of a simultaneous strengthening of the leading component and weakening of the trailing component in absolute intensity. This is shown by the mean relative uncertainties of each component in each sub-band, quantities whose values do not depend on absolute flux calibration. As frequency increases, the mean relative error in leading component intensity decreases consistently while the mean relative error in trailing component intensity consistently increases, but

3.4: EVOLUTION OF PROFILE SHAPE AS A FUNCTION OF OBSERVING FREQUENCY

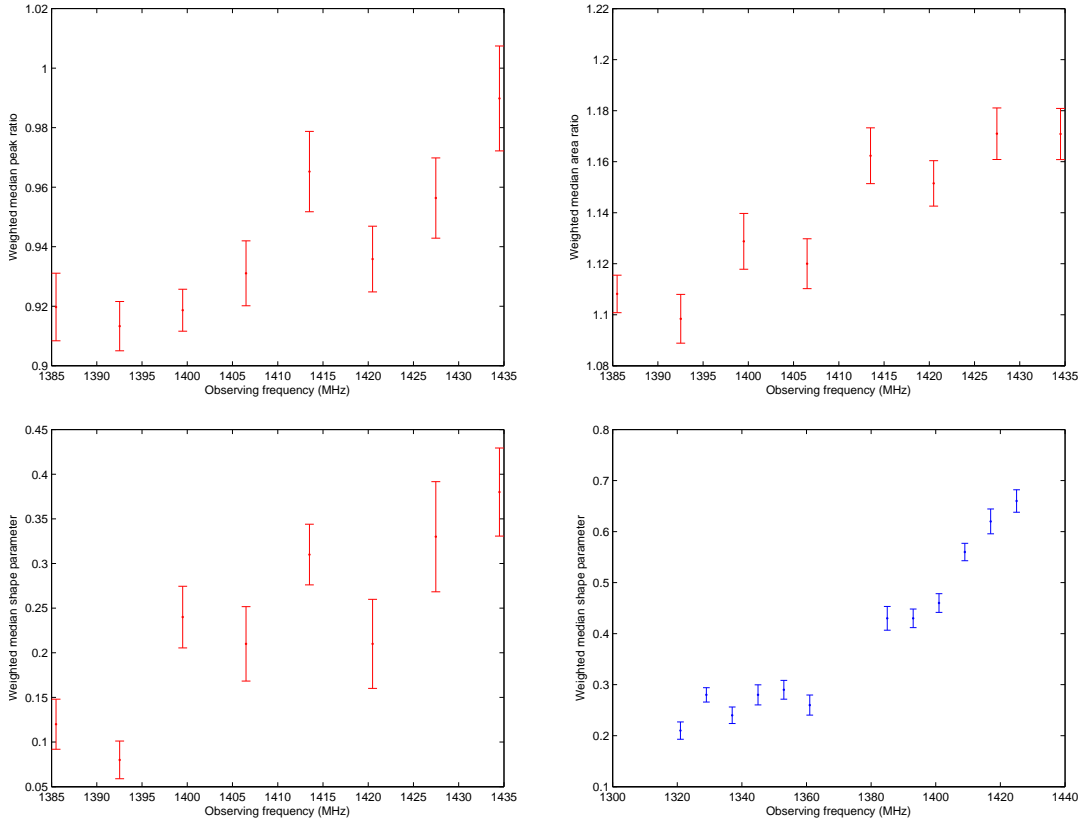


Figure 3.4: Evolution of all shape indicators as a function of frequency for PSR J1022+1001 in Effelsberg data around 1400 MHz, with Parkes data shown for comparison. The panels show Effelsberg peak ratio (top left), Effelsberg area ratio (top right), Effelsberg shape parameter (bottom left) and Parkes shape parameter (bottom right).

there is no trend in mean unscaled RMS off-pulse noise. The conclusion that it is the components, rather than the noise environment, which are changing in intensity rests on the assumption that the sub-band profiles are scaled in the same units at any given time, which is important for reliable frequency-scrunching. If the assumption were untrue, there could be no knowledge of the relationship between absolute pulse intensity and frequency, since trends in absolute RMS off-pulse noise could then be masked. However, there is no evidence for inconsistent scaling with frequency, and the assumption does not require the units of

intensity to remain constant over time. It is unusual for a pulse to strengthen as frequency increases at 1400 MHz, but, in the leading profile component of PSR J1022+1001, it seems no less plausible than the odd spectral relationship already clearly established between profile component amplitudes.

3.4.3 Separation of profile peaks as a function of frequency

There is evidence that the separation of the profile peaks follows the same general trend as their amplitude ratio, decreasing marginally by about 0.1° between 700 and 850 MHz before increasing markedly by around 0.7° between 850 and 1400 MHz (Figure 3.5). The separation values shown in Figure 3.5 are the error-weighted mean differences between crude peak positions in each sub-band containing at least five profiles, where a crude position is the bin number of maximum profile amplitude in the range where the peak is assumed to be. This sacrifices some accuracy, but provides sub-bin resolution by making only a broad prior assumption of peak locations. With full alignment, where the error-weighted mean profile is used to determine the phase locations of the peaks for all profiles, the separation is only determined to the nearest bin. Although formal errors have not been assigned, the spreads of separation values below and above 1000 MHz do not overlap, suggesting a real correlation at least between 850 and 1400 MHz. It is not possible to discern any change in peak separation across a frequency range of ~ 100 MHz.

3.5 Trends in the profile of PSR J1022+1001 over time

Examined by eye, profiles of PSR J1022+1001 often seem to vary in shape over short timescales. However, with noise contamination generally comparable to the apparent variation, it is difficult to assign short-term trends or perceive long-term

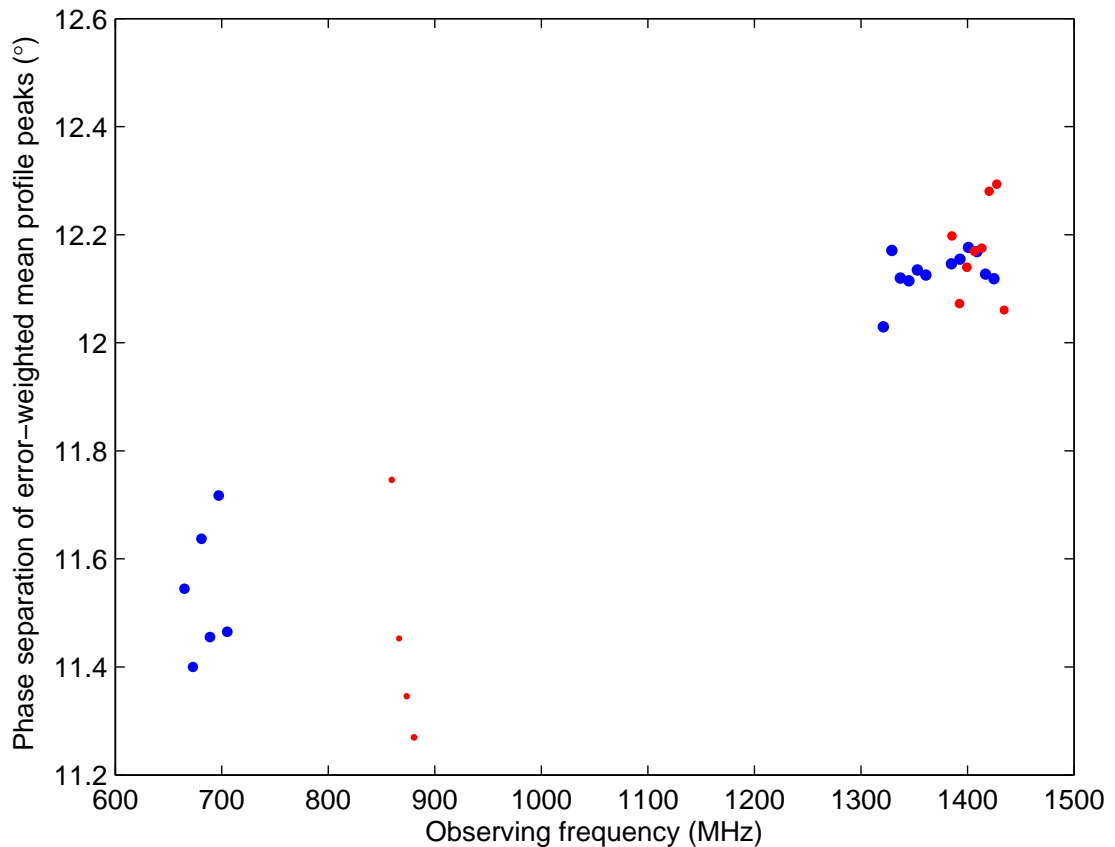


Figure 3.5: Evolution of profile peak separation for PSR J1022+1001 over a broad range of observing frequency, showing evidence for a turnover around 800 MHz followed by an increase. These values are error-weighted mean values in sub-bands, all from simply calibrated profiles for consistency. The area of each point is proportional to the log of the number of profiles in that sub-band. The blue points are from Parkes and the red points are from Effelsberg.

structure in the shape changes. Using numerical shape indicators, these things can be analysed. The assigned uncertainties take into account only random noise error, so the question is simply whether these uncertainties explain the magnitude of variation seen in the indicators.

3.5.1 Profile variation within an observation

One individual observation, picked from among many because it shows a trend, may be a statistical fluke. But it is interesting to note that the highest-SNR observation of PSR J1022+1001 in all the data studied shows a clear downward trend in the shape indicators across a 90-minute pointing, visible in most of the sub-bands as well as the full bands and slightly more pronounced at higher frequencies (Figure 3.6). It is similar in timescale to the smooth profile change reported by Kramer et al. (1999), though smaller in magnitude. Although this timescale is short, it is longer than that of moding, the phenomenon of switching profile shape which has been reported over hundreds of periods in some pulsars (Backer 1970). Fully calibrated in polarisation and averaged over all sub-bands in this 1400 MHz Parkes observation from MJD 53995, peak ratio declines by around 3%, area ratio by around 4% and s by about 0.1, which are comparable to the maximum possible changes due to scintillation across a sub-band at that frequency (see Figure 3.3). If they were due to a scintillative change over time in the gradient of intensity against frequency, the changes in the full-bandwidth profiles would be expected to be larger than in the sub-bands, but in fact they are similar. With the pulsar 29° away from the Sun in the sky at the epoch of observation, DM change is also very unlikely to be large enough to be responsible (see § 3.6.4), and, if it were, would cause much larger profile shape variation in the full-bandwidth measurements than in the sub-bands (see § 3.1.2).

The same data, when uncalibrated, shows the same shape trend marginally less clearly than when fully calibrated. When simply calibrated, the profiles show the downward trend significantly more clearly. It may be that simple calibration actually introduces spurious profile change, as was suggested by (Hotan et al. 2004). However, the persistence of the trend regardless of calibration suggests that it is, in large part, the result of either unmodelled measurement error or profile instability intrinsic to the pulsar.

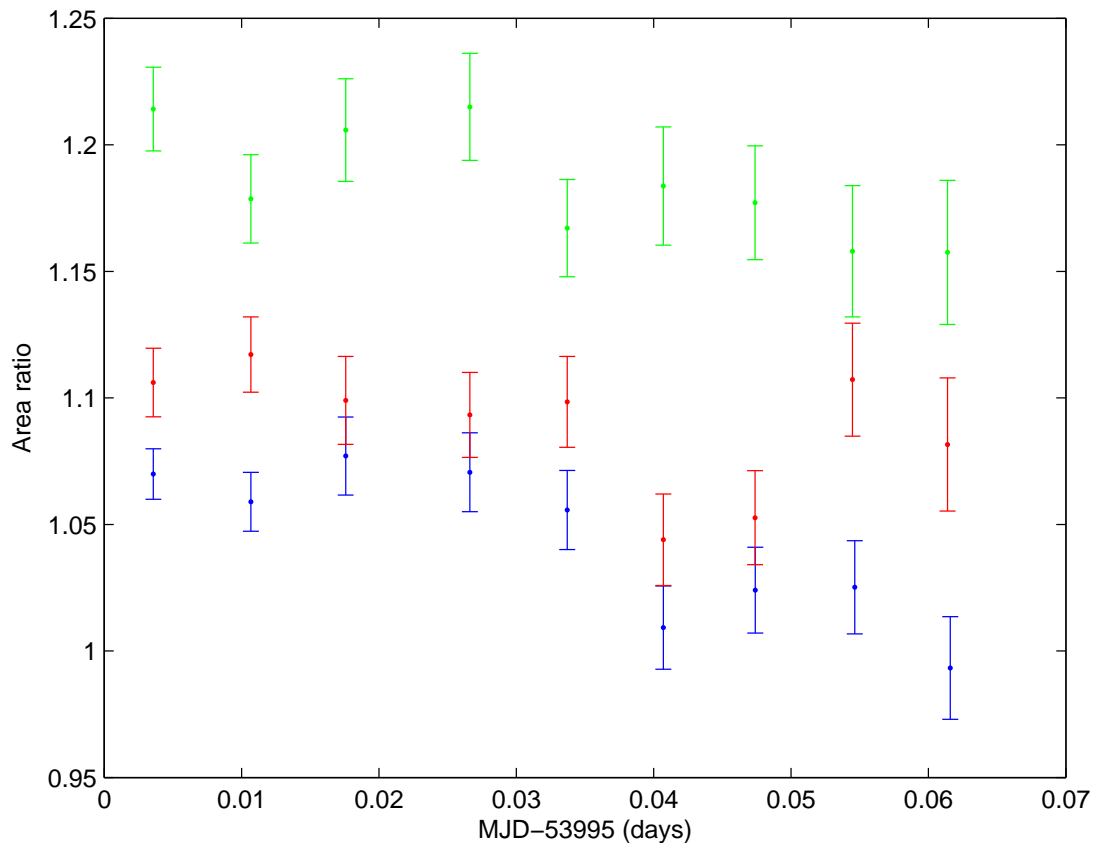


Figure 3.6: A downward trend in area ratio for PSR J1022+1001 on MJD 53995. The three fully calibrated Parkes sub-bands are 1345 (blue), 1385 (red) and 1417 MHz (green).

Whilst a number of observations of PSR J1022+1001 do show a trend in the shape indicators, the majority do not. Hotan et al. (2004) saw no convincing trends in 15 months of Parkes data, although this may be partly because they, in common with other analyses, used peaks of only a single phase bin each. The typical observational SNR is low enough to disguise a trend of the magnitude seen on MJD 53995, but there are many pointings in which profiles vary more than their SNRs would predict, changing apparently randomly on timescales of ~ 10 minutes. This could be explained by a source of random variation in addition to the measured noise (see §3.6). Liu et al. (2010, in prep.) showed that variation in PSR J1022+1001 on very short timescales of ~ 10 s–10 minutes is typically

uncorrelated in time, which is consistent with both noise and random variation and inconsistent with moding. In this case, it may not be possible to ascertain a clear timescale of variation, as was found by Ramachandran & Kramer (2003).

3.5.2 Profile variation between observations

Variation within each observation obscures any long-term change in the profile shape of PSR J1022+1001. To avoid this, the error-weighted mean values of the shape indicators from each observation can be used to assess variability over timescales of days to years. The errors in the shape indicator mean values were calculated by propagating the errors on the individual values (see Equation 3.1). In all sub-bands and full bands of the 1400 MHz Parkes data, the sets of shape indicator mean values per observation have $\chi_{X,obs}^2 > 1$ about the mean value of each set, regardless of calibration or which indicator is used. This reduced chi-squared statistic is given by:

$$\chi_{X,obs}^2 = \frac{1}{N_{obs} - 1} \sum_{k=1}^{N_{obs}} \frac{(X_{obs,k} - \bar{X}_{obs})^2}{(\delta X_{obs,k})^2} \quad (3.5)$$

where N_{obs} is the number of observations in a set of one sub-band or full band, k is observation number from 1 to N_{obs} , X denotes R , A or s , $X_{obs,k}$ is the error-weighted mean value of X in one observation, $\delta X_{obs,k}$ is the uncertainty in $X_{obs,k}$ and \bar{X}_{obs} is the error-weighted mean of all values of $X_{obs,k}$ in the set.

The mean values of $\chi_{X,obs}^2$ over all sub-bands and over all full bands (weighted by the number of observations in each band) are given in Tables 3.1–3.3, and imply significantly underestimated uncertainties on the indicator values for each observation. The fact that $\chi_{X,obs}^2$ is, in most cases, larger in full bands than in sub-bands is probably due to the smaller profile noise errors in full bands, rather than greater excess variation in full bands. It also shows, however, that the excess profile variation is not smoothed out across a bandwidth of 48 MHz. If an uncertainty cutoff is imposed on $X_{obs,k}$, so that only values with errors less

3.5: TRENDS IN THE PROFILE OF PSR J1022+1001 OVER TIME

	Parkes multibeam	Parkes H-OH	Effelsberg
Sub-bands	3.56	1.90	1.93
Full bands	8.31	4.23	2.70

Table 3.1: Reduced chi-squared of mean peak ratio per observation ($\chi_{R,obs}^2$) for profiles of PSR J1022+1001 around 1400 MHz, indicating excess variation in R_{obs} .

	Parkes multibeam	Parkes H-OH	Effelsberg
Sub-bands	11.45	5.42	7.01
Full bands	28.49	13.84	11.59

Table 3.2: Reduced chi-squared of mean area ratio per observation ($\chi_{A,obs}^2$) for profiles of PSR J1022+1001 around 1400 MHz, indicating excess variation in A_{obs} .

than a maximum size are used, the reduced chi-squared becomes larger as the cutoff becomes more stringent. This demonstrates that the uncertainties have not simply been underestimated by a common factor of $\chi_{X,obs}$, and is consistent with the presence of an additional source of error, affecting profiles of all SNRs, that is not included in the uncertainties.

Some of the distributions in time of error-weighted mean profile shape per observation look, particularly at lower frequencies, as though they are correlated on timescales of many days. This becomes more convincing when a maximum uncertainty cutoff is used (Figure 3.7). All of the sub-bands exhibit similar patterns, and the calibrated and uncalibrated data also give similar results to one another. A test for correlation, used by Jenet et al. (2006) on sets of TOAs, was conducted to formalise this. Shape indicator mean values per observation within

	Parkes multibeam	Parkes H-OH	Effelsberg
Sub-bands	43.65	18.43	10.55
Full bands	145.19	65.17	8.58

Table 3.3: Reduced chi-squared of mean shape parameter per observation ($\chi_{s,obs}^2$) for profiles of PSR J1022+1001 around 1400 MHz, indicating excess variation in s_{obs} .

a set were successively averaged together, and the variances of the averaged sets were plotted as a function of the number of values combined to make each average value. In logarithmic space, this function should have a gradient of -1 for uncorrelated (‘white’) data. With a cutoff imposed, the fully calibrated full band centred on 1341 MHz gave a gradient shallower than -1 , indicative of correlation (Figure 3.8). This was not demonstrable in the sub-bands or the higher-frequency full band, so the evidence for long-term profile trends is tentative. There is no evidence of variation as a function of parallactic angle, which would have suggested instrumental error. Long-term DM variation cannot be ruled out as a cause, and intrinsic profile change is also possible.

3.6 Statistical analysis of profile variation with time

3.6.1 Detection of excess profile variation

The statistical evaluation of profile change with time was conducted using sets of values of *weighted peak ratio*, *weighted area ratio* and *weighted shape parameter* for each profile, with each value defined as:

$$X_{w,i} = \frac{X_i - \tilde{X}}{\delta X_i} \quad (3.6)$$

where X denotes R , A or s , i indicates one profile of approximately 10 minutes’ duration in a set of one sub-band or full band (see §3.2.2), δX_i is the uncertainty in X_i and \tilde{X} is the error-weighted median of values of X in the set. The reduced chi-squared of X about its error-weighted median is then:

$$\chi_X^2 = \frac{1}{N_{prof} - 1} \sum_{i=1}^{N_{prof}} X_{w,i}^2 \quad (3.7)$$

where N_{prof} is the number of profiles in the set. The error-weighted median was chosen, in the case of the peak and area ratios, as the best estimate of

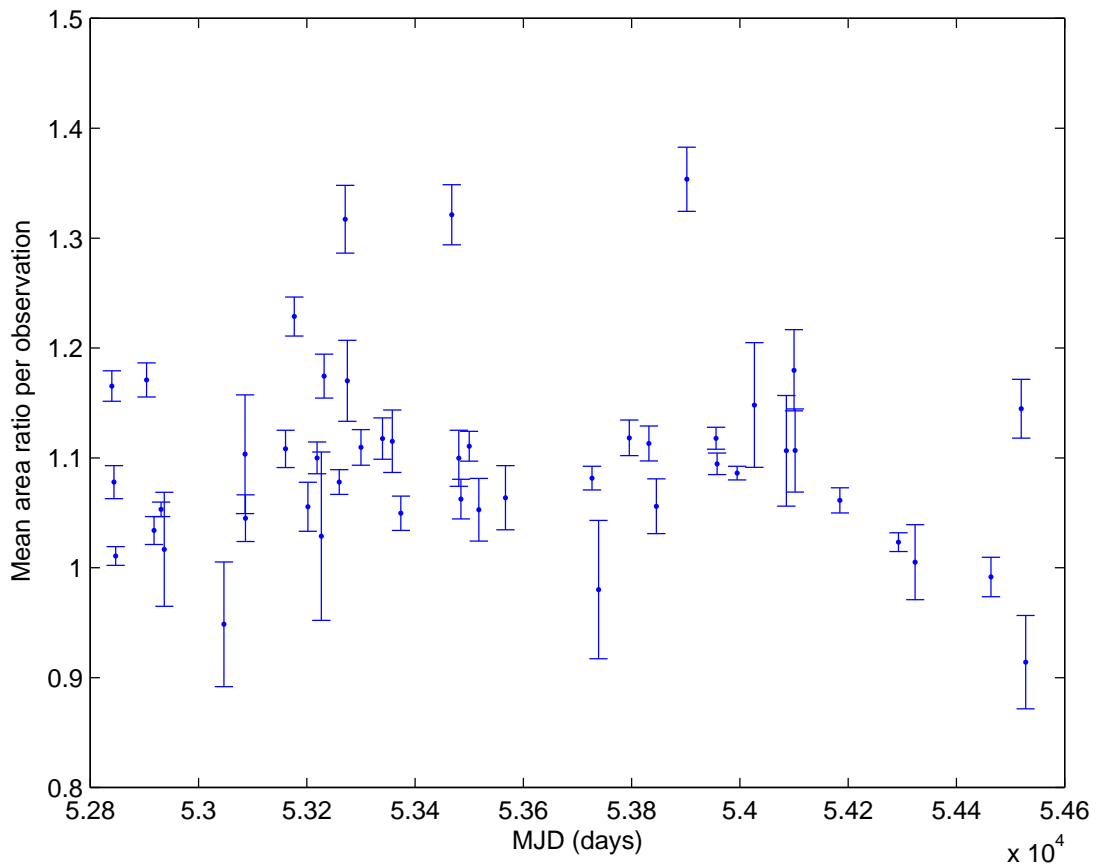


Figure 3.7: Mean area ratio per observation for PSR J1022+1001 as a function of time in Parkes data. This is the fully calibrated sub-band at 1385 MHz. There appears to be some correlation in time between values. For clarity, only values with an uncertainty of ≤ 0.08 are shown.

the ‘underlying’ ratio, i.e. the value which would represent the intrinsic ratio if the measured intensity of each peak and area were subject to extrinsic normal random variation only. Because two sets of normally distributed positive values give a set of ratios with a positive skew, the mean ratio tends to overestimate the underlying value. The median ratio is unbiased, and is more robust in the presence of extremely outlying ratio values. Median shape parameter values were used for consistency with ratios.

Under the assumptions that the measured intensity of each peak and area in each profile has a well-known uncertainty and belongs notionally to a normal

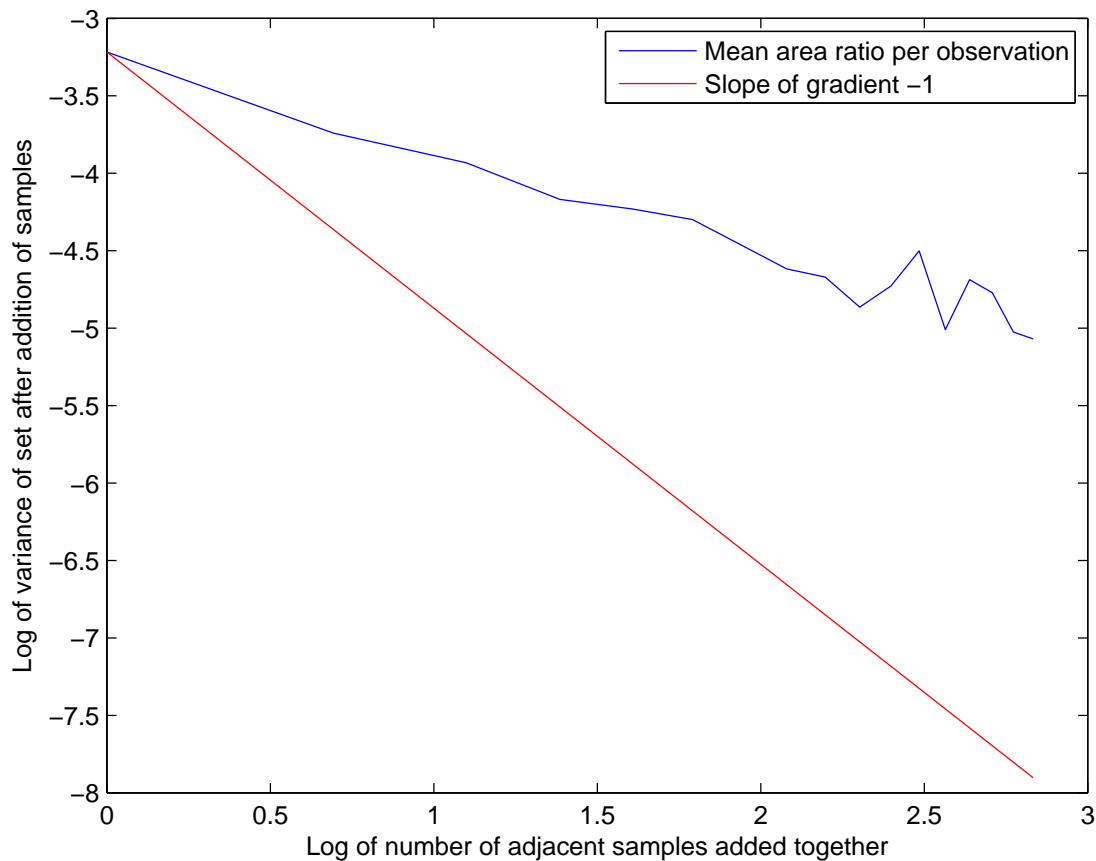


Figure 3.8: Variance of mean area ratio per observation for PSR J1022+1001 as adjacent samples are added together in Parkes data. This is the fully calibrated full band at 1341 MHz. Both axes are on a log scale, with a slope of gradient -1 for comparison. The fact that the variance gives a slope shallower than -1 implies correlation in time between values of the mean area ratio per observation.

distribution, and that all values of R and A in a single sub-band or full band belong to distributions with a common median, it follows that all values of R_w and A_w should fall on a distribution of median 0 and variance very close to 1, resulting in $\chi_R^2 = \chi_A^2 = 1$. Though slightly negatively skewed, this distribution should be close to a *standard normal distribution* (of mean 0 and variance 1), if the uncertainties are similar to those quoted above. Values of s_w should also approximate a standard normal distribution if values of s are approximately normally distributed in each sub-band and full band, giving $\chi_s^2 = 1$. A set of values

of X_w not approximating a standard normal distribution in shape, or a value of χ_x^2 significantly different to 1, would indicate inaccurate uncertainties on the values of parameter X .

It was also possible to analyse profile variation in each bin directly using normalised profiles (see §3.2.2). This was quantified using the reduced chi-squared of profile intensities about their error-weighted mean, or a template, in each bin:

$$\chi_{P,j}^2 = \frac{1}{N_{prof} - 1} \sum_{i=1}^{N_{prof}} \frac{(P_{i,j} - \bar{P}_j)^2}{(\delta P_{i,j})^2} \quad (3.8)$$

where $\delta P_{i,j}$ is the uncertainty in the intensity of profile i in bin j and \bar{P}_j is the error-weighted mean intensity of a set of profiles, or a template, in bin j . Reduced chi-squared values significantly greater than 1 would indicate variation at that phase, assuming accurate scaling and alignment. This method is similar to that used by Hotan et al. (2004), in which the standard deviation of profiles in each bin was plotted, but with error-weighting added to the procedure. Since the intensity normalisation used was not absolute, but rather a parameter in a chi-squared minimisation (see §3.2.2), a check on its effectiveness was provided by error-weighted covariances between the two intensities of the peak ratio and between the two areas of the area ratio:

$$C_Y = \sum_{i=1}^{N_{prof}} \frac{(Y_{i,F} - \bar{Y}_F)(Y_{i,B} - \bar{Y}_B)}{(\delta Y_{i,F})^2 + (\delta Y_{i,B})^2} \quad (3.9)$$

where Y denotes either P or S and $\delta Y_{i,j}$ is the uncertainty in $Y_{i,j}$. With effective normalisation, the error-weighted covariance between peaks or areas in a set of profiles should be negative if their relative amplitude is changing with time. If, instead, overall intensity differences between profiles still dominated any shape variation in spite of normalisation, so that some profiles are uniformly higher in intensity than others, then the covariance would be positive.

	Parkes multibeam	Parkes H-OH	Effelsberg
Sub-bands	1.46	1.20	1.37
Full bands	2.55	1.60	1.63

Table 3.4: Reduced chi-squared of peak ratio (χ_R^2) for profiles of PSR J1022+1001 around 1400 MHz, indicating excess variation in R .

	Parkes multibeam	Parkes H-OH	Effelsberg
Sub-bands	3.03	1.97	3.73
Full bands	6.73	3.66	4.80

Table 3.5: Reduced chi-squared of area ratio (χ_A^2) for profiles of PSR J1022+1001 around 1400 MHz, indicating excess variation in A .

3.6.2 Magnitude of excess profile variation

The statistical significance of profile variation is most reliably measured using many profiles from a wide time span. In every sub-band and both full bands around 1400 MHz, the collated Parkes and Effelsberg profiles of PSR J1022+1001 show a greater spread in shape than would be expected from their off-pulse noise. It is seen with increasing clarity in the reduced chi-squared values of peak ratio, area ratio and shape parameter when using sets of individual profiles from all observations. Tables 3.4–3.6 show the mean values of χ_x^2 in sub-bands and full bands (weighted by the number of profiles in each band) for each receiver used, using fully calibrated data for Parkes multibeam and simply calibrated data for Parkes H-OH and Effelsberg. $\chi_x^2 > 1$ is apparent in all cases, revealing that the total uncertainties in all measures of profile shape have been consistently underestimated by using only off-pulse noise. The fact that $\chi_A^2 > \chi_R^2$ for each band and receiver means that the RMS profile noise values have not been underestimated by a single factor, as this would make the two quantities equal.

One or more sources of additional error, independent of noise, were instead assumed to cause the excess variation. This takes no account of the structure of

3.6: STATISTICAL ANALYSIS OF PROFILE VARIATION WITH TIME

	Parkes multibeam	Parkes H-OH	Effelsberg
Sub-bands	15.26	8.95	6.04
Full bands	38.93	18.95	4.65

Table 3.6: Reduced chi-squared of shape parameter (χ_s^2) for profiles of PSR J1022+1001 around 1400 MHz, indicating excess variation in s .

changes over time, but simply assumes that they produce a normally distributed set of shape indicator values in the manner of uncorrelated variation. The additional errors in peak and area ratio are expressed here as relative errors, δR_{rel} and δA_{rel} , because these are easily expressed as relative errors in the intensities of the two peaks:

$$\delta X_{rel} = \delta Y_{F,rel}^2 + \delta Y_{B,rel}^2 \quad \text{if } X \equiv R \text{ or } X \equiv A \quad (3.10)$$

where $\delta Y_{F,rel}$ and $\delta Y_{B,rel}$ are the additional relative uncertainties in the leading and trailing peaks respectively, for either single- or multiple-bin peaks. An unexplained variation in peak or area ratio of 7%, for example, could be ascribed to a 7% variation in the leading peak, a 7% variation in the trailing peak or independent 5% variations in both peaks (where the variation would be assumed to affect the whole area of a peak by an equal percentage in the case of area ratio). Since the origin of the error in shape parameter is non-linear, and because the shape parameter itself is scaled from 0 to 1, its additional uncertainty, δs_{abs} , is expressed here as an absolute value. The magnitude of the additional error in one set of values of any shape indicator was calculated as a single uncertainty which brought the reduced chi-squared of the indicator down to 1 for that set:

$$\left. \begin{array}{l} \frac{1}{N_{prof} - 1} \sum_{i=1}^{N_{prof}} \frac{(X_i - \tilde{X})^2}{(\delta X_i)^2 + (\delta X_{rel} X_i)^2} \\ \frac{1}{N_{prof} - 1} \sum_{i=1}^{N_{prof}} \frac{(X_i - \tilde{X})^2}{(\delta X_i)^2 + (\delta X_{abs})^2} \end{array} \right\} = 1 \quad \left\{ \begin{array}{l} \text{if } X \equiv R \text{ or } X \equiv A \\ \text{if } X \equiv s \end{array} \right. \quad (3.11)$$

	Parkes multibeam	Parkes H-OH	Effelsberg
Sub-bands	5.4 %	4.4 %	4.1 %
Full bands	5.8 %	4.3 %	4.1 %

Table 3.7: Additional peak ratio relative errors (δR_{rel}) required to explain the spread of values of R for profiles of PSR J1022+1001 around 1400 MHz.

The additional errors are, in essence, like the E_{quad} parameters used in timing (see § 2.3 and Equation 2.2).

Tables 3.7–3.9 give the RMS of the additional errors required to explain the spread of shape parameter values in the sub-bands and full bands (weighted by the number of profiles in each band) for each receiver, corresponding to Tables 3.4–3.6. A Kolmogorov–Smirnov test (Press et al. 1992, pp. 623–626) verified that the additional errors changed the distributions of sets of weighted shape indicator values from being highly inconsistent with standard normal distributions to being consistent with them, allowing for skew and statistical outliers. The additional errors in the sub-bands are larger than the maximum possible changes across an 8-MHz sub-band due to scintillation (see Figure 3.3), while the similarity of the additional errors required in sub-bands and full bands also suggests that scintillation is not primarily responsible (see § 3.1.2).

A value of $\chi_x^2 = 2$ for a shape indicator in Tables 3.4–3.6 would imply that the corresponding additional error in Tables 3.7–3.9 was comparable to the typical noise error for that indicator, so it is clear from the actual tabular values that the additional sources of uncertainty are significant. In fact, they are often the largest sources of variation. Additional error values in the uncalibrated data sets are slightly lower (by about 0.5 % in area ratio), supporting the assertion of Hotan et al. (2004) that calibration can introduce variation. However, the additional spread is clear using any calibration or none.

These statistics benefit from the inclusion of a larger number of profiles than were available to previous studies of PSR J1022+1001. Ramachandran & Kramer

3.6: STATISTICAL ANALYSIS OF PROFILE VARIATION WITH TIME

	Parkes multibeam	Parkes H-OH	Effelsberg
Sub-bands	5.2 %	4.4 %	3.9 %
Full bands	4.6 %	3.9 %	3.9 %

Table 3.8: Additional area ratio relative errors (δA_{rel}) required to explain the spread of values of A for profiles of PSR J1022+1001 around 1400 MHz.

	Parkes multibeam	Parkes H-OH	Effelsberg
Sub-bands	0.21	0.21	0.19
Full bands	0.20	0.20	0.15

Table 3.9: Additional shape parameter absolute errors (δs_{abs}) required to explain the spread of values of s for profiles of PSR J1022+1001 around 1400 MHz.

(2003) analysed the significance of variation within a single observation, but produced reduced chi-squared values about the minimum peak ratio, whose position within a distribution has a larger uncertainty than does a median ratio determined from multiple values. Hotan et al. (2004) commented on a single observation in which variation appeared consistent with noise; they also presented standard deviation values for their entire data set, but did not compare these to the expectations due to noise. Both papers used single-bin peak ratios, which are subject to greater noise errors than multiple-bin area ratios.

The analysis conducted here shows not only that there are significant profile shape variations throughout the observations of PSR J1022+1001, but that they are almost certainly correlated across at least 6.3° of phase around one or both peaks. This is evidenced by the similarity of the additional uncertainties required in peak and area ratios. For example, if an additional peak ratio uncertainty of 5.0% were, hypothetically, caused by a 5.0% variation in the intensity of one peak, then a corresponding additional uncertainty of 4.4% in area ratio would likely be due to a 4.4% variation in the integrated intensity of the 9 bins around that same peak; if the variations in the bins around the peak were each 5.0% but were uncorrelated with one another, the expected change in their integrated

intensity would be only around one third of this, or 1.7%, unless they were each undergoing relative variation of three times more than the peak itself, which is implausible. By the same argument, the similarity of additional error values in sub-bands and full bands infers a correlation of variation across ~ 100 MHz in observing frequency.

The additional uncertainties required in each shape indicator are similar across different instruments, with the larger differences between reduced chi-squared values indicating different average noise levels. The shape parameter values have, by far, both the largest reduced chi-squared values and the largest differences between them. This may well be the result of profile change across a larger phase range than is probed by the area ratio. However, the shape parameter is also the most difficult to interpret. If there is a component of profile variation that cannot be described by a linear combination of the extreme templates (see § 3.3.1), then the reduced chi-squared becomes less predictable. Similarly, systematic differences between profiles recorded by different instruments (see § 3.4.1) may result in different reduced chi-squared values. The fact that uncertainty in s is a non-linear function of profile noise and s itself also makes the magnitudes of its additional uncertainties less well defined, although confidence in the values is increased by their good agreement across instruments.

3.6.3 Phase location of excess profile variation

The reduced chi-squared in each bin of normalised profiles (see Equation 3.8) was used to try to determine the phases at which variation occurs, and as a check on profile alignment. This confirmed the other measurements of variation, with reduced chi-squared values in all sub-bands elevated above 1 across the on-pulse region and particularly around the peaks (Figure 3.9). The result is clearer than that obtained from standard deviation without error-weighting of the profiles, as was done by Hotan et al. (2004). Variation is seen very clearly in

full bands, although some of this is likely due to scintillation effectively mixing profiles of different frequencies in the same set (see §3.1.2). Negative error-weighted covariances between peak intensities and between area intensities were found in all sub-bands and full bands, suggesting that the profiles had been normalised effectively.

It remains difficult, however, to localise the variation within the on-pulse region, because the scaling and alignment methods used are designed to minimise variation across each complete profile and must therefore spread the higher reduced chi-squared values across the pulse. The scaling, in particular, does not give absolute intensities and will lock more strongly to broader pulse features, so the higher reduced chi-squared values around the trailing peak cannot be taken as evidence that it is the source of the profile instability. Profile normalisation by only one component transferred apparent variation to whichever component was not used for normalisation, but comparison of reduced chi-squared values after normalisation by either component did not show one as more stable than the other, which was a phenomenon seen by Kramer et al. (1999). Additionally, error-weighted covariances between peak intensities and between area intensities were a mixture of positive and negative values, calling into question the effectiveness of single-component normalisation (see §3.6.1).

3.6.4 Possible contributors to observed profile variation

The analysis used contained some approximations and statistical imperfections, but these do not appear to be significant. The interpolation required for full profile alignment, for example, cannot be perfect. However, conducting and then reversing the sub-bin alignment, with interpolation at each stage, closely recovered the variation seen in the profiles aligned to the nearest bin. Furthermore, variation in all sub-bands and full bands was lower for fully aligned profiles than for those aligned to the nearest bin. The difference was a relative error of around

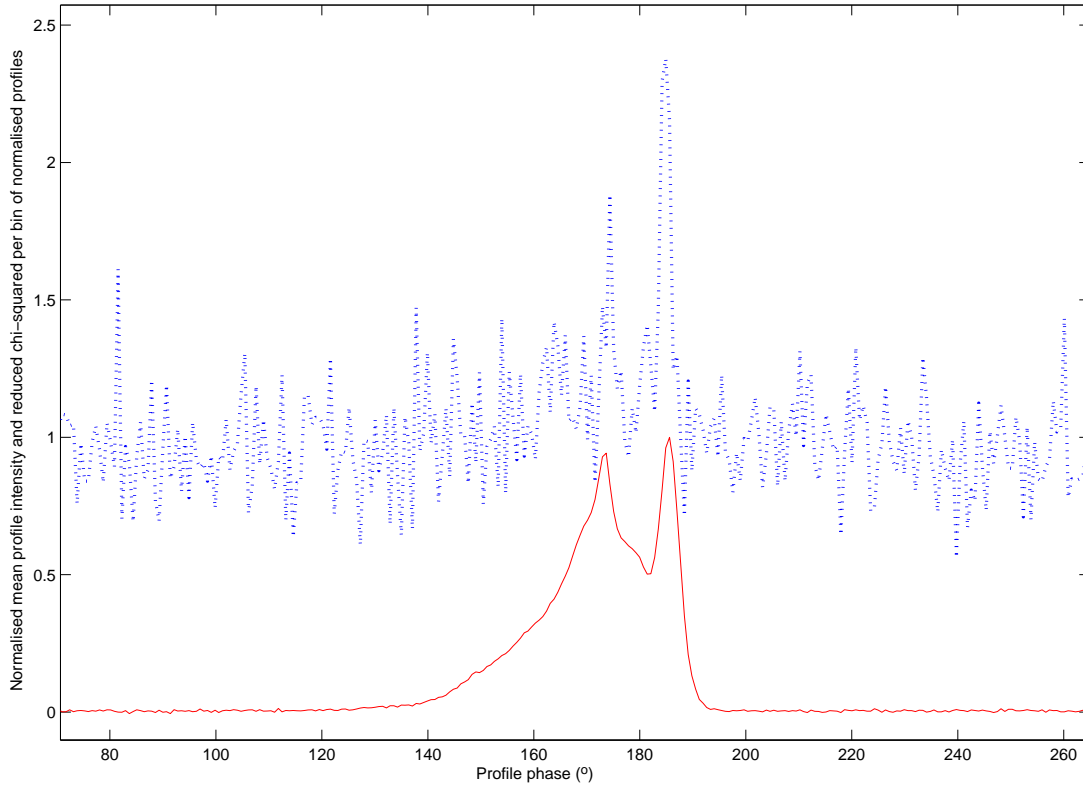


Figure 3.9: Error-weighted mean of normalised profiles (solid line) and reduced chi-squared of normalised profiles (dashed line) as a function of rotational phase in PSR J1022+1001, observed at Parkes across 8 MHz of bandwidth centred on 1393 MHz. Profile variation is seen in the on-pulse region. This is a particularly clear example, but the same trend is repeated in other sub-bands.

3% in peak ratio and around 1% in area ratio, considered independent of noise. These values are consistent with the changes in peak ratio and area ratio found by shifting the error-weighted mean profiles at each frequency by phases of up to half a bin in each direction while assuming that the profile peaks had not moved. This suggests that they represent the error introduced by neglecting sub-bin alignment and thereby comparing regions of slightly unequal profile phase. Spurious effects of interpolation appear to be negligible.

In the statistical analysis, the reduced chi-squared values of weighted peak and area ratios have associated uncertainties. They are expected to be biased

towards being slightly greater than 1, due to the fact that the uncertainties in peak intensity values, used in weighting the peak and area ratios, have associated uncertainties of their own. Weighted shape parameter values are likely to be similarly affected, as shape parameter uncertainties may also be imperfectly known. Bias due to skew in ratio distributions can also increase or decrease reduced chi-squared values depending on the median ratio value, but it makes a very small impact in the presence of the typical uncertainties in the data from PSR J1022+1001. A larger effect than both of these is the random error in the reduced chi-squared values of weighted sets resulting from the finite number of values (typically several hundred) from which they were calculated. Simulations of normally distributed sets of pseudo-random numbers suggest that the reduced chi-squared values may vary by around 5%, which does not alter the magnitudes of the additional uncertainties at the significance levels quoted in §3.6.2. Although the expected bias of reduced chi-squared values increases slightly with higher ratio values, it is far too small an effect to cause the observed trend of higher additional uncertainties being required at higher frequencies.

Interstellar scintillation, although it contributes to profile variation in full bands, was shown in §3.6.2 to be unable to translate the measured frequency dependence of PSR J1022+1001 into the time variation observed. It was found through the simulation of additional dispersion that a change in the dispersive delay of about $30 \mu\text{s}$ was required across a profile's bandwidth to produce a change in peak or area ratio of 2%, which would be large enough to stand out against profile noise. Around 1400 MHz, this corresponds to approximate DM changes of $0.2 \text{ cm}^{-3} \text{ pc}$ across a bandwidth of 50 MHz or $1.0 \text{ cm}^{-3} \text{ pc}$ across a bandwidth of 10 MHz, much larger than the DM variations previously measured through timing, which were $\lesssim 0.004 \text{ cm}^{-3} \text{ pc}$ when PSR J1022+1001 passed close to the Sun in the sky due to its small ecliptic longitude (You et al. 2007). Only observations made when the pulsar appeared very near the Sun would have larger DM changes. Dispersion variation is therefore unlikely to be a cause of noticeable change to

the shape indicators.

The bin-correlated nature of the variation could still be explained by either an intrinsic effect or polarisation calibration error, which would affect all the highly polarised parts of the profile in common. If the source is instrumental, then it is well in excess of the 1–2% expected by Hotan et al. (2004). This could be due to dynamic level setting, which is employed to cope with fluctuating signal and interference intensity in 2- and 4-bit systems. As the output digitisation levels may be set for each receiver feed individually, it could change the differential gain in between calibrator observations and produce unmodelled effects (van Straten 2010). The magnitude of this effect is not well known.

3.6.5 Comparison of PSR J1022+1001 with PSR J1730–2304 and PSR J1603–7202

In light of the unmodelled errors that can be introduced into pulse profiles by instrumentation, a comparison of two pulsars can help to identify the common uncertainties to be expected in all sources. Two less highly linearly polarised pulsars than PSR J1022+1001 were studied in the same way with Parkes CPSR2 observations for this purpose: PSR J1603–7202 and PSR J1730–2304.

PSR J1603–7202 has a similar period, period derivative and profile shape to PSR J1022+1001, but PSR J1603–7202 has a highly circularly polarised trailing component, where in PSR J1022+1001 that component is highly linearly polarised (Manchester & Han 2004). Error-weighted mean profiles of PSR J1603–7202 appear to show (mostly very weak) emission covering about 300° of its rotational phase, including a small, two-component ‘interpulse’ approximately 130° after the centre of the main pulse and just before the start of the narrow off-pulse region (Figure 3.10). Since the emission region is contiguous, PSR J1603–7202 is likely to have closely aligned rotational and magnetic axes (which must also be closely aligned with our line of sight to the pulsar), as opposed to being an

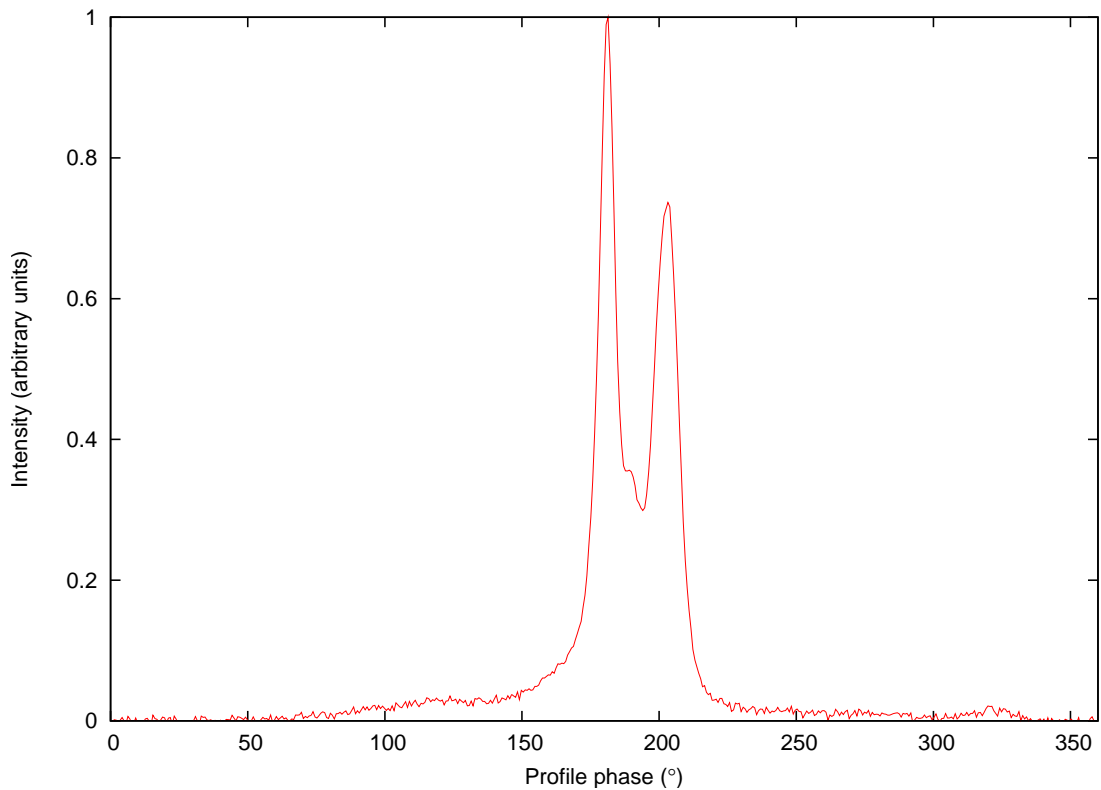


Figure 3.10: A fully calibrated profile of PSR J1603–7202 at 1405 MHz from Parkes, showing extended emission and an interpulse around 320° of phase, about 130° from the main pulse. These things suggest that PSR J1603–7202 probably has closely aligned rotational and magnetic axes. The integration time of the profile is 32 minutes and the bandwidth is 48 MHz.

orthogonal rotator in which radiation beams from two magnetic poles are visible.

Observations of PSR J1603–7202 covered approximately 6 years from 2003 to 2009, each typically occurring every 15 days and lasting 1 hour. PSR J1603–7202 shows measurable variation in calibrated profile shape as a function of frequency, with increases of about 5% in the error-weighted median values of both peak and area ratio in 8-MHz sub-bands progressing from 1321 to 1425 MHz. The frequency evolution allows for maximum differences due to scintillation of around 0.4% in peak and area ratio between profiles of 8 MHz bandwidth at the same central frequency. This could translate into apparent time variation of profile shape, but, with a scintillation timescale and bandwidth of roughly 15 minutes and

1.5 MHz respectively, the time variation due to scintillation would be expected largely to be averaged out across a bandwidth of 8 MHz or more.

The profiles of PSR J1603–7202 show, overall, a slight excess of variation in area ratio with time, but it is much smaller than that of PSR J1022+1001 and in keeping with the expected level of instrumental error, being around 1.5 % in fully calibrated CPSR2 sub-bands. There is no visible evidence of variation in the reduced chi-squared of each bin of the normalised profiles, and the profiles appear to be properly aligned (Figure 3.11). The covariances between peak intensities and between area intensities were also found to be positive in all sub-bands and full bands, showing that no variation in relative component amplitude could be discerned above the limiting uncertainty of profile normalisation. PSR J1603–7202 demonstrates that significant profile variation above the expected noise is not seen for all pulsars.

PSR J1730–2304 was observed over a similar time span to PSR J1603–7202. It has a degree of linear polarisation which has been reported very differently in previous studies (Xilouris et al. 1998; Ord et al. 2004), and in this analysis showed a polarisation level in between those published before, while its PA as a function of profile phase was consistent with past results (Figure 3.12). The total intensity profile shows quite extended emission and a small interpulse, although the main pulse is too broad to allow determination of whether the interpulse comes from the same magnetic pole.

The trailing two peaks of its three-peaked profile were used for shape analysis. It was identified by Kramer et al. (1999) as having an unstable profile, and showed a moderate degree of time variation, requiring additional errors of approximately 3 % in area ratio in fully calibrated 8-MHz-wide sub-bands. Variation of its profile with frequency was also measurable, but not sufficient to explain the time variation through scintillation. Its linear polarisation does not appear to be high enough to cause the 1–2 % maximum variation quoted by Hotan et al. (2004), although it could be that unmodelled effects related to linear polarisa-

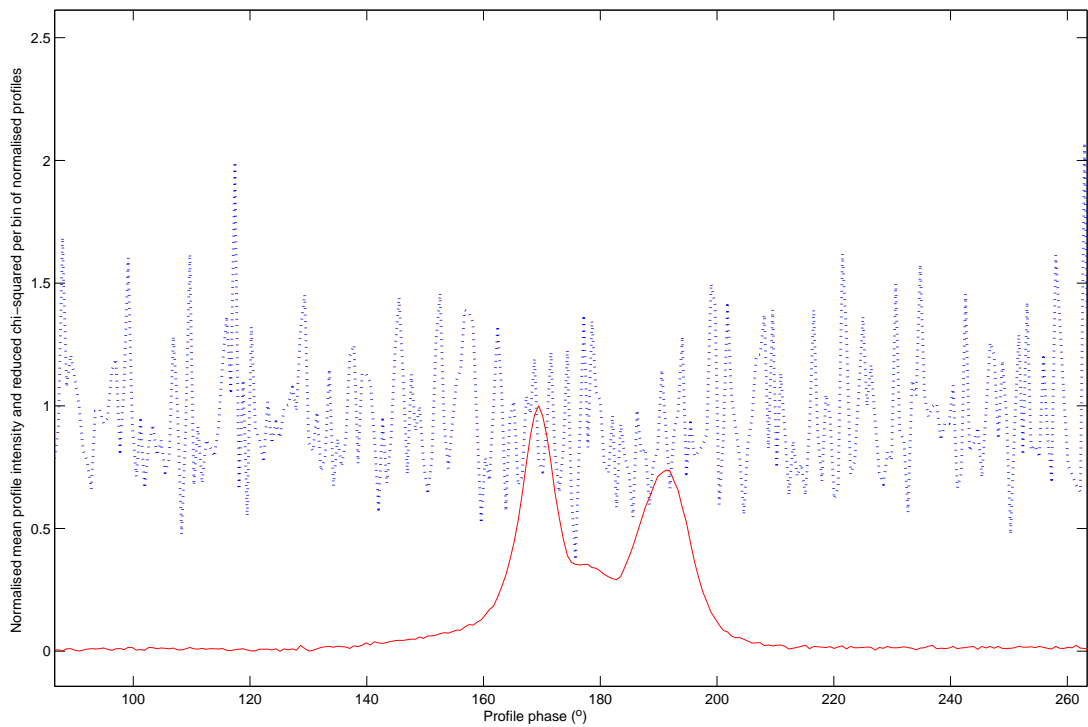


Figure 3.11: Error-weighted mean of normalised profiles (solid line) and reduced chi-squared of normalised profiles (dashed line) as a function of rotational phase in PSR J1603–7202, observed with CPSR2 across 8 MHz of bandwidth centred on 1321 MHz. No profile variation is seen in this or other sub-bands.

tion are responsible. Whatever the cause of variation in PSR J1022+1001 and PSR J1730–2304, it does not significantly affect PSR J1603–7202.

3.7 Timing of PSR J1022+1001

Timing of the calibrated sub-band profiles obtained with CPSR2 was conducted using both fixed and adaptive templates, where the adaptive templates were those produced during the calculation of shape parameter values. The fixed-template timing was as in §2.3.1. TOAs with estimated uncertainties greater than $15 \mu\text{s}$ were excluded. The timing results are shown in Table 3.10.

The two sets of templates gave very similar uncertainties for the pulsar system

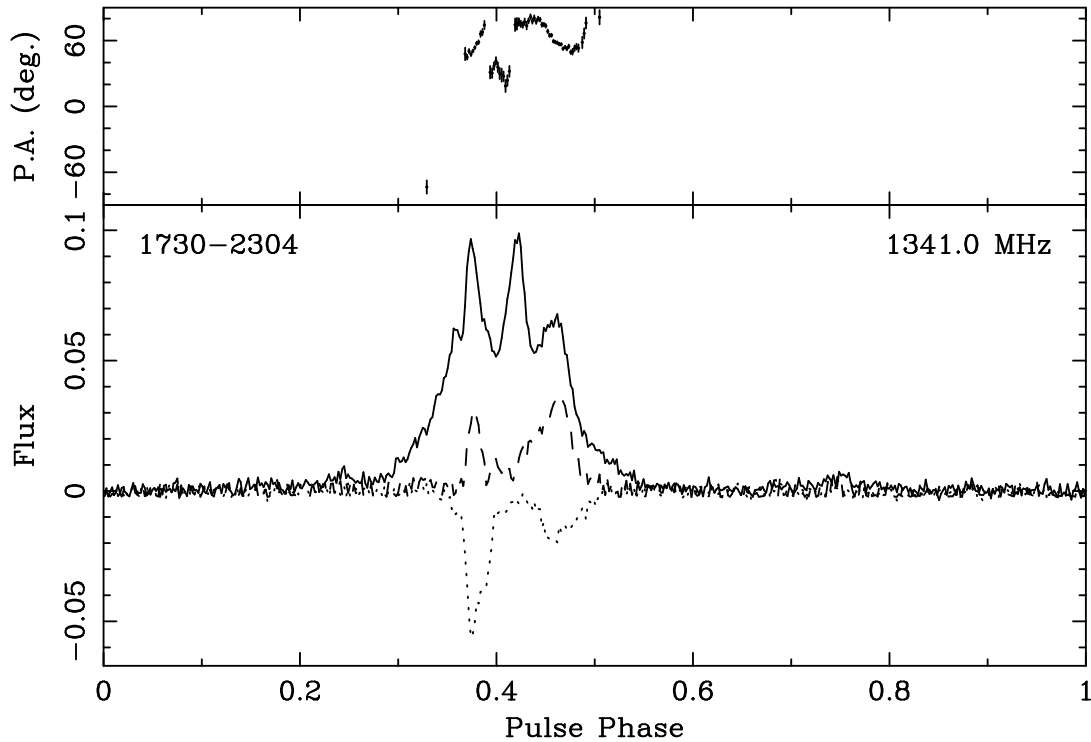


Figure 3.12: Fully calibrated PA and polarisation profiles of PSR J1730–2304 at 1341 MHz from Parkes. The integration time is 63 minutes and the bandwidth is 48 MHz. Top window: PA as a function of profile phase. Bottom window: polarisation profiles. The solid line is total intensity, the dashed line linearly polarised intensity and the dotted line circularly polarised intensity. The degree of linear polarisation is in between those previously published by Xilouris et al. (1998) and Ord et al. (2004). Emission is quite extended, and there is a small interpulse around fractional pulse phase 0.75, although it is not possible to say whether this is from the same magnetic pole as the main pulse

parameters, and most, though not all, of the parameters agree to within these uncertainties between the two methods. Slightly higher E_{quad} values (see § 2.3) were required for the adaptively timed TOAs. The large improvement in timing accuracy achieved with adaptive templates by Kramer et al. (1999) was not reproduced. Some of the early Effelsberg TOAs had much larger residuals than all the other data, which may explain the inaccurate timing found in the previous study. Most of those points were removed from this timing fit as instrumentally

Parameter	Fixed templates	Adaptive templates
Time span of observations (yrs)	12.08	12.08
Number of TOAs	7739	7786
Error-weighted residual RMS (μs)	5.47	5.62
χ_f^2 without E_{quad}	1.16	1.18
Right ascension (h:m:s)	10:22:58.0058 (10)	10:22:58.0052 (10)
Declination ($^{\circ}$:':")	+10 : 01 : 52.76 (4)	+10 : 01 : 52.73 (4)
Spin frequency (s^{-1})	60.77944798776615 (14)	60.77944798776571 (14)
Frequency derivative (s^{-2})	$-1.60097 (3) \times 10^{-16}$	$-1.60092 (3) \times 10^{-16}$
Reference epoch (MJD)	52754	52754
DM ($\text{cm}^{-3} \text{pc}$)	-	-*
Proper motion (RA) (mas yr^{-1})	-17.17 (3)	-17.13 (3)
Parallax (mas)	1.95 (19)	1.78 (19)
Binary model	BT	BT
Binary orbital period (days)	7.80513028255 (10)	7.80513028253 (10)
Epoch of periastron (MJD)	52759.96964 (16)	52759.96965 (17)
Projected semimajor axis (lt-s)	16.76541620 (10)	16.76541596 (11)
Longitude of periastron ($^{\circ}$)	97.732 (8)	97.732 (8)
Orbital eccentricity	$9.7234 (11) \times 10^{-5}$	$9.7227 (12) \times 10^{-5}$

Table 3.10: Fitted system parameters of PSR J1022+1001 using sub-bands, timed with both fixed and adaptive templates at Effelsberg, Parkes and Westerbork.

* A fixed value of $DM = 10.2521 (1) \text{ cm}^{-3} \text{ pc}$ was used (Hotan et al. 2006).

corrupted.

The lack of timing improvement with adaptive templates does not imply that no profile variation occurs. Rather, it suggests that it is subtle and appears random. Some of it must be accounted for in the template-matching error, but some may manifest as a higher error-weighted residual RMS than would be produced by noise alone. If the profile variations do not cause the profile peaks to change separation noticeably, then they need not cause very large timing residuals.

4

Upper limits on the strength of the gravitational wave background from pulsar timing

Gravitational wave detection is the most sought-after goal of contemporary high-precision pulsar timing (see § 1.3.2). Past observations may form part of a data set that provides an eventual positive detection, but cannot alone reveal the presence of gravitational waves. Existing data are instead used to place upper limits on the amplitudes of gravitational waves from individual sources and, in particular, on the collective strength of the cosmic GWB (see e.g. Verbiest 2009). Since this background must comprise a superposition of waves from many sources and therefore be stochastic, placing a bound on it amounts to an estimate of the sensitivity of pulsar timing to residuals that are correlated in time, or ‘red’. It is therefore important that the measured residuals are as uncorrelated, or ‘white’, as possible. In this chapter, timing of the pulsars discussed in the previous chapters, with analytic templates, is used to produce upper limits on GWB strength, and the reliability of the limits is examined in comparison with previously published values.

4.1 Method of determination of an upper limit on gravitational wave background strength

The method used here to limit the GWB was that developed by Jenet et al. (2006), and further examined by Hobbs et al. (2009). It is different to the technique for detection described by Jenet et al. (2005), which looks for correlations between the residuals of different pulsars as a function of their angular separation on the sky, and is sensitive to the component of the GWB near the Earth that is common to all the pulsars' residuals. The limiting method, by contrast, correlates the residuals of each pulsar with functions of time that are low-order polynomials, in order to detect red noise, but does not correlate different pulsars with one another. The polynomial correlation functions are summed incoherently to produce a detection parameter. It is assumed that the actual data do not contain a detectable signal, so this is used to create a threshold detection level. The effect of an artificial GWB is then added to the pulsar residuals to see if the threshold level is reliably exceeded, in which case that background is considered detectable. This method should provide a conservative limit as it does not look for signals correlated between pulsars. Its limit will be more general than one provided by the detection method, as it assumes only the most general form for the GWB-induced component of the residuals. Because of this, the limit will only be reliable for residuals that are white in the absence of gravitational waves, so it is necessary to test the real residuals for redness that may be introduced by other unmodelled factors such as systematic measurement error or timing noise.

4.1.1 Algorithm for determination of gravitational wave background upper limit

The practical implementation of the limit method is mostly described by Jenet et al. (2006) and Hobbs et al. (2009), and information from those papers is used

4.1: METHOD OF DETERMINATION OF AN UPPER LIMIT ON GRAVITATIONAL WAVE BACKGROUND STRENGTH

throughout this sub-section. The successful detection, or otherwise, of a simulated GWB of amplitude A_G (see Equation 1.19) was determined from an ensemble of possible backgrounds and sets of residuals, allowing a statistical assessment of the likelihood of detection. The actual data set for each pulsar consisted of TOAs with associated uncertainties and residuals. The real residuals from each pulsar were first subtracted from the real TOAs to generate a set of model TOAs, sampled at the same pulse numbers as the real ones and corresponding to the best fit of the real TOAs. The model TOAs were obtained recursively using TEMPO2 without fitting. Using MATLAB, the real residuals, kept with their associated TOA uncertainties, were then randomly shuffled with the function RANDPERM and added back on to the unshuffled model TOAs to create multiple artificial realisations of the timing data in the absence of gravitational waves. The seed of the random numbers was changed regularly to avoid repeated sequences. With the new TOAs and uncertainties determined, their associated residuals were calculated by refitting them with TEMPO2. Many shufflings were used to create multiple realisations of TOAs without gravitational waves, in order to find the threshold of GWB detectability. Their validity depends on the uncertainties accurately describing the magnitudes of the residuals, so that they are weighted correctly, and on the residuals being white, so that no correlations are destroyed by the re-ordering. To create corresponding data containing gravitational wave signatures, multiple GWBs were simulated, and their effects added to the model TOAs, using the GWBKGRD plugin for TEMPO2, whose workings are detailed by Hobbs et al. (2009). Shuffled pairs of real residuals and uncertainties were again added to these TOAs in MATLAB to produce multiple artificial realisations of the timing data in the presence of gravitational waves. Their residuals were again found by refitting the new data using TEMPO2, which was particularly important because much of the gravitational wave signature would be absorbed into changes to the pulsar system parameters and therefore undetectable (see § 4.2.2). Many shufflings were again used to create multiple realisations of data with gravitational

waves, in order to determine whether a GWB would produce residuals that would exceed the detection threshold with specified levels of confidence.

The GWB detection parameter was calculated within MATLAB, using the same process for the TOA realisations with and without gravitational waves. For each realisation, the N_p TOAs from each pulsar, p , were first converted from time values, t_p , to dimensionless normalised time values, τ_p :

$$\tau_{p,i} = 2 \left(\frac{t_{p,i} - t_{p,1}}{t_{p,N_p} - t_{p,1}} \right) - 1 \quad (4.1)$$

where i indicates TOA number from 1 to N_p . This scaled and shifted the TOAs such that $\tau_{p,1} = -1$ and $\tau_{p,N_p} = 1$. A set of discrete polynomial functions of normalised time, $J_p(\tau_p)$, was then computed, whose sum would be used to approximate the residuals associated with a realisation of the TOAs from pulsar p after fitting, and which would give an indication of the level of redness in those residuals. To do this, unnormalised polynomials, $K_p(\tau_p)$, were first found recursively by error-weighted Gram–Schmidt orthogonalisation¹ (Press et al. 1992, pp. 43–45):

$$K_{p,l,i} \left\{ \begin{array}{ll} \equiv 1 & \text{if } l = 0 \\ = \tau_{p,i} - \left(\sum_{i=1}^{N_p} \frac{\tau_{p,i}}{(\delta t_{p,i})^2} \right) / \left(\sum_{i=1}^{N_p} \frac{1}{(\delta t_{p,i})^2} \right) & \text{if } l = 1 \\ = K_{p,l-1,i} \left(\tau_{p,i} - \left(\sum_{i=1}^{N_p} \frac{\tau_{p,i} K_{p,l-1,i}^2}{(\delta t_{p,i})^2} \right) / \left(\sum_{i=1}^{N_p} \frac{K_{p,l-1,i}^2}{(\delta t_{p,i})^2} \right) \right) \\ \quad - K_{p,l-2,i} \left(\sum_{i=1}^{N_p} \frac{K_{p,l-1,i}^2}{(\delta t_{p,i})^2} \right) / \left(\sum_{i=1}^{N_p} \frac{K_{p,l-2,i}^2}{(\delta t_{p,i})^2} \right) & \text{if } l > 1 \end{array} \right. \quad (4.2)$$

where l is an integer indicating polynomial order from 0 to some reasonable maximum value (see § 4.1.2) and $\delta t_{p,i}$ is the uncertainty (in units of time) associated

¹This procedure was adapted from that described by Wolfram MathWorld: <http://mathworld.wolfram.com/Gram-SchmidtOrthonormalization.html>

4.1: METHOD OF DETERMINATION OF AN UPPER LIMIT ON GRAVITATIONAL WAVE BACKGROUND STRENGTH

with TOA i . These were then normalised to form the final polynomial set:

$$J_{p,l,i} = K_{p,l,i} / \sqrt{\sum_{i=1}^{N_p} \frac{K_{p,l,i}^2}{(\delta t_{p,i})^2}} \quad (4.3)$$

Normalisation was done after the recursive calculations, to avoid numerical rounding errors. The final polynomials were orthonormal in a weighted sense, obeying the conditions:

$$\sum_{i=1}^{N_p} \frac{J_{p,m,i} J_{p,n,i}}{(\delta t_{p,i})^2} \begin{cases} = 1 & \text{if } m = n \\ = 0 & \text{if } m \neq n \end{cases} \quad (4.4)$$

The polynomials generated for a few data sets were checked to ensure that they satisfied these conditions. The detection parameter, Υ , for one realisation of multiple pulsars was then defined from the correlation of the polynomials with their associated TOA residuals, summed over all pulsars, the polynomials up to a chosen order L and all residuals:

$$\Upsilon = \sum_{p=1}^E \sum_{l=0}^L \left(N_p \left(\sum_{i=1}^{N_p} \frac{r_{p,i} J_{p,l-1,i}}{(\delta t_{p,i})^2} \right)^2 / \left(\sum_{i=1}^{N_p} \frac{(r_{p,i} - \bar{r}_p)^2}{(\delta t_{p,i})^2} \right) \right) \quad (4.5)$$

where the array consists of E pulsars, $r_{p,i}$ is the residual (in units of time) associated with the realisation of TOA i from pulsar p and \bar{r}_p is the mean residual for that realisation of all the TOAs from pulsar p . Red residuals would be better represented than white ones by low-order polynomials, resulting in a higher detection parameter value. Using many realisations, distributions of values of Υ were obtained both with and without gravitational waves. The threshold detection parameter, Υ_0 , was taken to be the value in the distribution without waves above which a fraction p_f of the values lay. The positive detection parameter, Υ_d , was taken to be the value in the distribution with waves above which a fraction p_d of the values lay. A positive GWB detection would be revealed by $\Upsilon_d > \Upsilon_0$, accepting a probability of p_f that a non-existent background would be falsely found and a probability of $(1 - p_d)$ that a detectable background would be missed. The upper limit of the real GWB, A_{max} , would be the lowest value of A_S to permit a detection within these confidence limits.

4.1.2 Parameters of a simulated gravitational wave background

GWBs were simulated using a spectral power index of $\alpha = -2/3$ (see § 1.3.2), corresponding to a background emitted by supermassive black hole binary systems. Following Jenet et al. (2006), each background consisted of 10^4 gravitational waves, randomly distributed on the sky and with random frequencies, f_{GW} , between 1.59×10^{-11} and 2.31×10^{-5} Hz, corresponding to periods of 12 hours to 2000 years. The frequencies were drawn from a probability distribution uniform in $\log(f_{GW})$, following Hobbs et al. (2009), because higher-frequency waves originate from shorter-period binary systems, which last for less time before coalescing and are therefore less numerous. The distances of the pulsars from the Earth were set at the values given by the model from which their model TOAs were formed. Following Jenet et al. (2006), the detection probabilities used were $p_f = 0.001$ and $p_d = 0.95$, meaning that, in a real data set, there would be a 0.1% chance of falsely detecting a GWB of amplitude $\gtrsim A_{max}$ where there was a real amplitude of $A \ll A_{max}$, and there would be a 95% chance of detecting a GWB of amplitude $\gtrsim A_{max}$ where there was a real amplitude of $A \simeq A_{max}$.

The above parameters can all be set in `GWBKGRD`. When testing a GWB of amplitude A_S for detectability, 100 realisations of the background were generated. In converging on a value of A_{max} , distributions of 100 detection parameter values were used to find Υ_0 and Υ_d . In common with Jenet et al. (2006), 10^4 values were used in the final analysis for statistical accuracy, i.e. each GWB realisation was added to 100 shufflings of the residuals. Polynomials up to order 7 were summed to produce all values of Υ (i.e. $L = 7$ in Equation 4.5), as they collectively represent 95% of the power of a GWB of $\alpha = -2/3$ in timing residuals (Jenet et al. 2006). The offset of each set of realised residuals for each pulsar was chosen

such that the error-weighted mean of the set was zero, i.e.:

$$\sum_{i=1}^{N_p} \frac{r_{p,i}}{(\delta t_{p,i})^2} = 0 \quad (4.6)$$

This offset is arbitrary, and is normally chosen by TEMPO2 to give a set of residuals an unweighted mean of zero. By instead satisfying the above condition, the zeroth-order polynomial, which is constant as a function of time for any set of residuals, made no contribution to any value of Υ . Without satisfying the condition, this polynomial would correlate with the offset and, since its value was slightly changed upon each shuffling of residuals, could dominate over the polynomials that were fitting GWB signals, spoiling the detection parameter as an indicator of gravitational waves.

4.2 Limits on gravitational wave background strength using pulsar timing with analytic templates

The TOAs obtained from PSR J1022+1001 using adaptive Gaussian templates in § 3 were used to produce upper limits on the strength of the GWB. The residuals of the other pulsars proved too red to be used. Even PSR J1022+1001, which passed the whiteness tests, was suspected of some redness, as described below, and the reliability of the limits produced is criticised in light of this.

4.2.1 Tests of the suitability of timing residuals

The whiteness of the timing residuals obtained in § 2 was tested using the three-fold method described by Jenet et al. (2006). First, a Lomb-Scargle periodogram of the residuals was inspected, as this is akin to an FFT with irregularly sampled data and would show clear peaks in structural frequency (Press et al. 1992,

pp. 575–584). Second, the variance of the residuals was measured as adjacent time samples were successively summed and the data set shrank. Uncorrelated residuals would give a gradient of -1 in a log-log plot of number of samples added together against variance. Finally, the polynomial spectrum of the real data was checked for patterns. Only PSR J1022+1001 passed all of these tests.

4.2.2 Limits using PSR J1022+1001

The previously successful sub-band timing of PSR J1022+1001 was used to generate an upper limit on the GWB. Figure 4.1 shows an example of the effects of a GWB, generated by `GWBKGRD`, on the real TOAs from PSR J1022+1001, before and after fitting with `TEMPO2`. The waves with the longest periods dominate the pre-fit residuals, creating an apparently linear slope that is actually part of a very long sine wave. These signals may well exist in real TOAs, but they represent only what would be seen if the pulsar system parameters were a priori known. As shown in the post-fit residuals, most of the gravitational wave power is lost in fitting, with linear and quadratic patterns simply interpreted as being part of the frequency and slowdown of the pulsar’s rotation respectively. The RMS of the error-weighted post-fit residuals is $0.1 \mu\text{s}$ higher than that of the real residuals (see Table 3.10), but its red signature makes it detectable using the method described in § 4.1.1. The longer a pulsar data set, the better the long-period gravitational waves could be separated from truly linear and quadratic slopes.

With Effelsberg, Parkes and Westerbork data combined over 12 years, a limit of $A_{max} = 1.1 \times 10^{-14}$ was obtained, which is just above the top of the estimated amplitude of $10^{-15} < A < 10^{-14}$ (Jenet et al. 2006). This was the same as that found by Jenet et al. (2006) using seven pulsars, and only 10% higher than that of Verbiest (2009) using a long data set of PSR J1713+0747. As previously found by Hobbs et al. (2009) with PSR J1857+0943, the value of Υ for the real TOAs from PSR J1022+1001 with all telescopes combined was found to be suspiciously high

4.2: LIMITS ON GRAVITATIONAL WAVE BACKGROUND STRENGTH USING PULSAR TIMING WITH ANALYTIC TEMPLATES

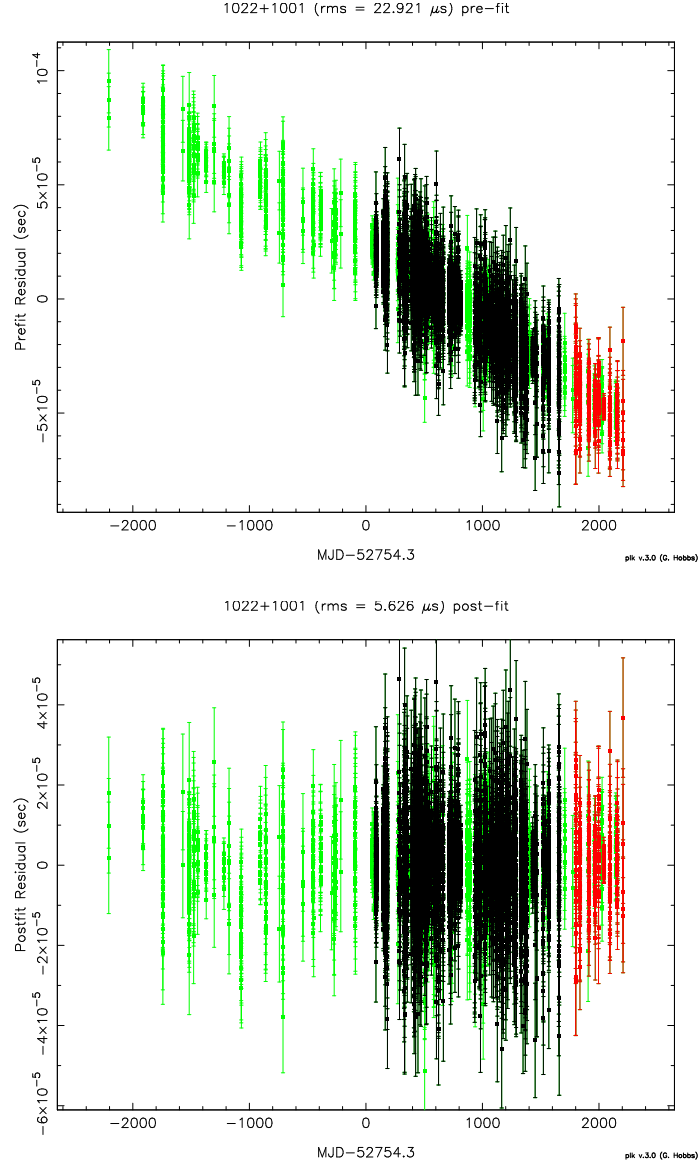


Figure 4.1: Timing residuals for PSR J1022+1001 after addition of an artificial GWB of $A_S = 1.1 \times 10^{-14}$ to the TOAs. The top panel shows the pre-fit residuals based on the timing model for PSR J1022+1001 derived from its real TOAs; these residuals are dominated by the GWB. The bottom panel shows the post-fit residuals after updating the timing model, in which most of the GWB signal has been lost in fitting the pulsar system parameters. The error-weighted post-fit residual RMS is $0.1 \mu\text{s}$ higher than that of the real residuals; the effect of the GWB cannot be seen by eye, but its red signature makes it detectable. Effelsberg is in green, Parkes in black and Westerbork in red.

compared to the shuffled threshold values – higher than the entire distribution, in this case – indicating likely redness in the real TOAs and a limit that was too low. With Parkes and Westerbork only, the limit became $A_{max} = 1.4 \times 10^{-14}$, with the value of Υ for the real TOAs still above the threshold detection parameter distribution but not by as much. With Parkes data alone, the limit became $A_{max} = 1.7 \times 10^{-14}$, and the value of Υ for the real TOAs was near the top end of the threshold detection parameter distribution but not above it. Figure 4.2 shows the threshold and positive detection parameter distributions, and the detection parameter value for the real TOAs, for a successful detection of an artificial GWB of $A_S = 1.1 \times 10^{-14}$ using TOAs from PSR J1022+1001 obtained at Effelsberg, Parkes and Westerbork.

The indication is that even the most conservative GWB limit obtained here is optimistic. However, PSR J1022+1001 still seems to be a powerful pulsar in terms of constraining the strength of the GWB. With more advanced whitening techniques, such as are described by Champion et al. (2010), a stringent and reliable limit might be obtained.

4.2: LIMITS ON GRAVITATIONAL WAVE BACKGROUND STRENGTH
USING PULSAR TIMING WITH ANALYTIC TEMPLATES

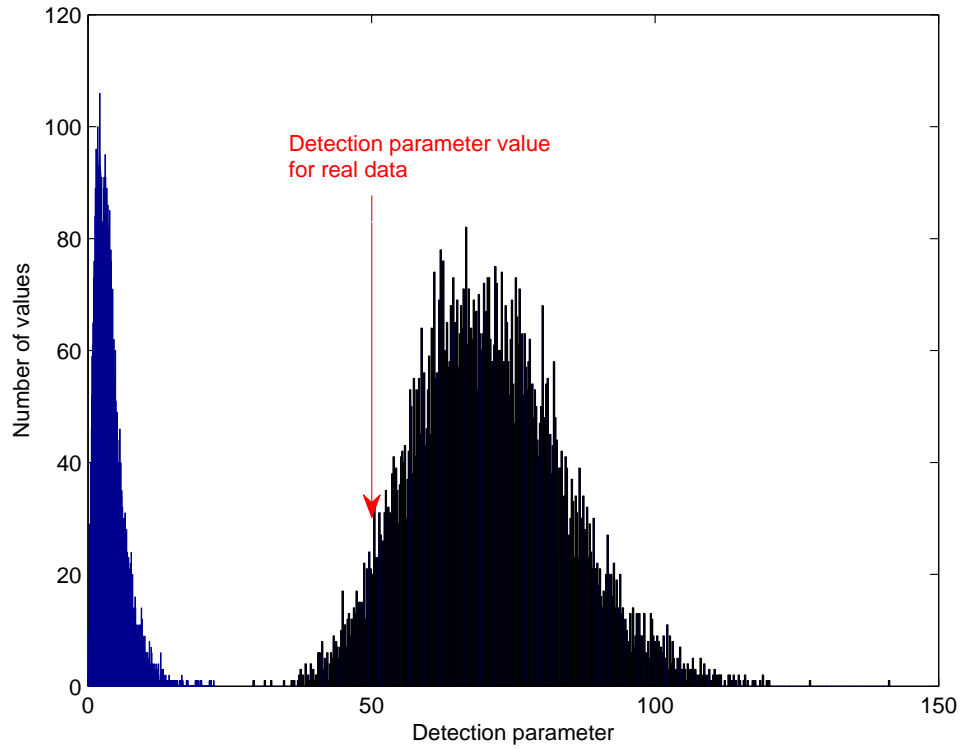


Figure 4.2: Threshold and positive detection parameter distributions for artificial GWB detection using TOAs from PSR J1022+1001 obtained at Effelsberg, Parkes and Westerbork. The positive detection parameter distribution, on the right, is almost entirely above that of the threshold detection parameter, indicating the successful detection of an artificial GWB of $A_S = 1.1 \times 10^{-14}$. However, the value obtained with the real residuals, unshuffled and containing no inserted gravitational waves, is also above the threshold detection parameter distribution, suggesting that the real residuals are correlated.

5

Discussion of results and future work

5.1 Pulsar timing with analytic templates

Analytic templates exist in order to provide noise-free and adaptable representations of pulse profiles. Gaussian templates were first used as a means to identify individual pulse components (Krishnamohan & Downs 1983), and, although more components were generally used in this PhD project than could be easily distinguished in the profiles fitted, they are a natural way to represent the integrated stochastic emission of pulsars. Gaussian templates have been shown in this thesis to produce consistent timing results across telescopes (§2.2.1), which is important for the PTAs striving to make the first direct detection of gravitational waves. Equally significantly, they have been shown to be adaptable as a function of frequency (§2.2.2–2.2.3), which is becoming necessary as observing bandwidths increase. Adaptation using a constant number of components with fixed centres cannot always be accomplished across a broad frequency range, but over a narrow frequency range it can be done. It gives an additional dimension to phase-aligned templates, and can yield better timing results than are achieved by scrunching

profiles and templates in frequency (§ 2.3.1).

It is clear from attempts to produce reliable limits on gravitational wave strength that correlations within timing residuals can be very subtle and difficult to measure, but that they can make a big difference to any limit placed on the GWB. A polynomial spectrum is, in fact, a good way to pick up such red noise, by comparing that of the real residuals to those of a shuffled set (§ 4.2.1–4.2.2). Removing or managing redness will be necessary for the foreseeable future, and perhaps in perpetuity, and its minimisation is obviously desirable. Doing this while combining data sets across telescopes has been shown to be a challenge, and a direct comparison of the timings of a set of profiles with analytic and high-SNR templates would be a useful future piece of work. This would help to show whether such templates can be a source of systematic timing error.

It will be a great advantage to PTAs if observations are stored with as much detail as possible – as profiles with many sub-integrations, frequency channels and counterpart calibration observations. Data storage limitations have, in the past, sometimes resulted in only TOAs being kept. There are myriad complex aspects to the process of turning profiles into TOAs, and if as much unprocessed data as possible is kept, researchers will be able to compare and select different approaches. These data should be readily accessible within any timing collaboration, as should different processing pipelines. To this end, the EPTA is currently developing a repository for its profiles as it moves towards LEAP.

5.2 The effect of apparent pulse profile variation on timing accuracy

It is difficult to pin down the causes of measured profile variation, but work on PSR J1022+1001 has made it clear that such variation is as much a source of inaccuracy as instrumental noise for some pulsars (§ 3.6.2). The similar, bin-correlated

variation seen in PSR J1730–2304, but not in PSR J1603–7202, demonstrates that it is not common to all pulsars, and that it could be related to linear polarisation (§ 3.6.5). However, PSR J1730–2304 does not seem to be polarised enough for the observed variation to be explained by the expected level of calibration error, so the possibility remains open that small, mostly random profile variations are intrinsic to PSR J1022+1001 and PSR J1730–2304. The recently installed digital filterbank at Jodrell Bank may help to settle this question by processing data from circular receiver feeds in the Lovell Telescope. If the apparent profile changes are instrumental, the reverse of the linear-feed results would be expected, with clear excess variation in PSR J1603–7202 but little or none in PSR J1022+1001 and PSR J1730–2304.

If instrumental error is the problem, then systems with high numbers of output bits, which do not require dynamic level setting, could be the solution. Unmodelled effects will become increasingly significant as observational SNR increases with the next generation of radio telescopes, and these defects will need to be understood lest they become the limiting factor in timing accuracy. PSR J1022+1001 would provide a good test case for such work, and the analysis methods used here (§ 3.3.1) could be employed as they have been shown to be sensitive to variation in this and other pulsars (§ 3.4–3.6). If intrinsic MSP profile variation has been found, then it may be difficult to overcome as it seems to be random and without a clear timescale (§ 3.5.1).

In spite of its timing issues, PSR J1022+1001 has proved to have relatively uncorrelated residuals which may make it a powerful member of PTAs (§ 4.2.1). It has been used to set low upper limits on the strength of the GWB, although even the most conservative of these, $A_{max} = 1.7 \times 10^{-14}$, may be optimistic as a result of its apparent red residual noise (§ 4.2.2). Even with this taken into account, however, it appears to be capable of producing a surprisingly stringent limit on the GWB. With more advanced whitening techniques, a more reliable estimate of its sensitivity to gravitational waves will be possible. If its excess

profile variation can also be removed, then its residuals might become naturally whiter and place it among the best pulsars for gravitational wave measurement.

References

- Baade W., Zwicky F., 1934, Proc. Nat. Acad. Sci., 20, 259
- Backer D. C., 1970, Nature, 228, 42
- Bell S. J., Hewish A., 1967, Nature, 213, 1214
- Blandford R., Teukolsky S. A., 1976, ApJ, 205, 580
- Britton M. C., van Straten W., Bailes M., Toscano M., Manchester R. N., 2000, in Kramer M., Wex N., Wielebinski R., eds., Pulsar astronomy – 2000 and beyond, IAU Colloquium 177, pp. 73–76. Astronomical Society of the Pacific, San Francisco, CA, USA
- Burke B. F., Smith F. G., 2002, An introduction to radio astronomy. Cambridge University Press, Cambridge
- Camilo F., 1995, PhD thesis, Princeton University, Princeton, NJ, USA
- Carroll B. W., Ostlie D. A., 1996, An introduction to modern astrophysics. Addison-Wesley, Reading, MA, USA
- Champion D. J., Hobbs G. B., Manchester R. N., Edwards R. T., Backer D. C., Bailes M., Bhat N. D. R., Burke-Spolaor S., Coles W., Demorest P. B., Ferdman R. D., Folkner W. M., Hotan A. W., Kramer M., Purver M. B., Sarkissian J. M., Stairs I. H., van Straten, W., Verbiest, J. P. W., Yardley, D. R. B., 2010, ApJ, 720, L201
- Cognard I., Theureau G., Desvignes G., Ferdman R., 2009, arXiv e-Prints, 0911.1612v1
- Cordes J. M., Lazio T. J. W., 2003, arXiv e-Prints, astro-ph/0207156v3
- Cordes J. M., Lazio T. J. W., 2003, arXiv e-Prints, astro-ph/0301598v1
- Damour T., Deruelle N., 1986, Ann. Inst. H. Poincaré (Physique Théorique), 44, 263

- Demorest P. B., Pennucci T., Ransom S. M., Roberts M. S. E., Hessels J. W. T., 2010, *Nature*, 467, 1081
- Detweiler S., 1979, *ApJ*, 234, 1100
- Edwards R. T., Hobbs G. B., Manchester R. N., 2006, *MNRAS*, 372, 1549
- Ferdman R. D., van Haasteren R., Bassa C. G., Burgay M., Cognard I., Corongiu A., D’Amico N., Desvignes G., Hessels J. W. T., Janssen G. H., Jessner A., Jordan C., Karuppusamy R., Keane E. F., Kramer M., Lazaridis K., Levin Y., Lyne, A. G., Pilia, M., Possenti, A., Purver, M., Stappers, B., Sanidas, S., Smits, R., Theureau, G., 2010, *Class. Quant Grav.*, 27, 084014
- Gangadhara R. T., Thomas R. M. C., 2008, in Hasan S. S., Gangadhara R. T., Krishnan V., eds., *Turbulence, dynamos, accretion disks, pulsars and collective plasma processes*, *Astrophysics and Space Science proceedings*, pp. 137–145. Springer-Verlag, New York, NY, USA
- Gold T., 1968, *Nature*, 218, 731
- Hellings R. W., Downs G. S., 1983, *ApJ*, 265, L39
- Hewish A., Bell S. J., Pilkington J. D. H., Scott P. F., Collins R. A., 1968, *Nature*, 217, 709
- Hibschman J. A., Arons J., 2001, *ApJ*, 546, 382
- Hobbs G., Archibald A., Arzoumanian Z., Backer D., Bailes M., Bhat N. D. R., Burgay M., Burke-Spolaor S., Champion D., Cognard I., Coles W., Cordes J., Demorest P., Desvignes G., Ferdman R. D., Finn L., Freire P., Gonzalez M., Hessels, J., Hotan, A., Janssen, G., Jenet, F., Jessner, A., Jordan, C., Kaspi, V., Kramer, M., Kondratiev, V., Lazio, J., Lazaridis, K., Lee, K. J., Levin, Y., Lommen, A., Lorimer, D., Lynch, R., Lyne, A., Manchester, R., McLaughlin, M., Nice, D., Osłowski, S., Pilia, M., Possenti, A., Purver, M., Ransom, S., Reynolds, J., Sanidas, S., Sarkissian, J., Sesana, A., Shannon, R., Siemens, X., Stairs, I., Stappers, B., Stinebring, D., Theureau, G., van Haasteren, R., van Straten, W., Verbiest, J. P. W., Yardley, D. R. B., You, X. P., 2010, *Class. Quant Grav.*, 27, 084013
- Hobbs G., Jenet F., Lee K. J., Verbiest J. P. W., Lommen A., Yardley D., Manchester R., Shettigara C., Edwards R. T., 2009, *MNRAS*, 394, 1945
- Hobbs G. B., Edwards R. T., Manchester R. N., 2006, *MNRAS*, 369, 655
- Hotan A. W., Bailes M., Ord S. M., 2004, *MNRAS*, 355, 941

- Hotan A. W., Bailes M., Ord S. M., 2006, MNRAS, 369, 1502
- Hotan A. W., van Straten W., Manchester R. N., 2004, PASA, 21, 302
- Janssen G. H., Stappers B. W., Kramer M., Nice D. J., Jessner A., Cognard I., Purver M. B., 2008, A&A, 490, 753
- Janssen G. H., Stappers B. W., Kramer M., Purver M., Jessner A., Cognard I., 2008, in Bassa C., Wang Z., Cumming A., Kaspi V. M., eds., 40 years of pulsars: Millisecond pulsars, magnetars and more, AIP Conference Proceedings vol. 983, pp. 633–635. American Institute of Physics, Melville, NY, USA
- Jenet F., Finn L. S., Lazio J., Lommen A., McLaughlin M., Stairs I., Stinebring D., Verbiest J., Archibald A., Arzoumanian Z., Backer D., Cordes J., Demorest P., Ferdman R., Freire P., Gonzalez, M., Kaspi, V., Kondratiev, V., Lorimer, D., Lynch, R., Nice, D., Ransom, S., Shannon, R., Siemens, X., 2009, ArXiv e-Prints, 0909.1058v1
- Jenet F. A., Anderson S. B., 1998, PASP, 110, 1467
- Jenet F. A., Cook W. R., Prince T. A., Unwin S. C., 1997, PASP, 109, 707
- Jenet F. A., Hobbs G. B., Lee K. J., Manchester R. N., 2005, ApJ, 625, L123
- Jenet F. A., Hobbs G. B., van Straten W., Manchester R. N., Bailes M., Verbiest J. P. W., Edwards R. T., Hotan A. W., Sarkissian J. M., Ord S. M., 2006, ApJ, 653, 1571
- Kaspi V. M., Taylor J. H., Ryba M., 1994, ApJ, 428, 713
- Kramer M., Wielebinski R., Jessner A., Gil J. A., Seiradakis J. H., 1994, A&AS, 107, 515
- Kramer M., Xilouris K. M., Camilo F., Nice D., Lange C., Backer D. C., Doroshenko O., 1999, ApJ, 520, 324
- Krishnamohan S., Downs G. S., 1983, ApJ, 265, 372
- Large M. I., Vaughan A. E., Mills B. Y., 1968, Nature, 220, 340
- Liu K., 2009, personal communication
- Liu K., Wex N., Kramer M., Keane E. F., Purver M. B., 2010, in prep.
- Lorimer D. R., Kramer M., 2005, Handbook of pulsar astronomy. Cambridge University Press, Cambridge, UK
- Lyne A. G., Smith F. G., 1968, Nature, 218, 124
- Lyne A. G., Smith F. G., 2006, Pulsar Astronomy, 3rd ed. Cambridge University

Press, Cambridge, UK

Manchester R. N., 2008, in Bassa C., Wang Z., Cumming A., Kaspi V. M., eds., 40 years of pulsars: Millisecond pulsars, magnetars and more, AIP conference proceedings vol. 983, pp. 584–592. American Institute of Physics, Melville, NY, USA

Manchester R. N., Han J. L., 2004, *ApJ*, 609, 354

Mereghetti S., 2008, *Astron. Astrophys. Rev.*, 15, 225

Michel F. C., Li H., 1999, *Phys. Rep.*, 318, 227

Misner C. W., Thorne K. S., Wheeler J. A., 1973, *Gravitation*. W. H. Freeman, New York, NY, USA

Müller J. W., 2000, *Rapports BIPM*, 2000/6

Navarro J., Manchester R. N., Sandhu J. S., Kulkarni S. R., Bailes M., 1997, *ApJ*, 486, 1019

Ord S. M., van Straten W., Hotan A. W., Bailes M., 2004, *MNRAS*, 352, 804

Pacini F., 1967, *Nature*, 216, 567

Press W. H., Teukolsky S. A., Vetterling W. T., Flannery B. P., 1992, *Numerical recipes: The art of scientific computing*, 2nd ed. Cambridge University Press, Cambridge

Radhakrishnan V., Cooke D. J., Komesaroff M. M., Morris D., 1969, *Nature*, 221, 443

Ramachandran R., Kramer M., 2003, *A&A*, 407, 1085

Ratel G., 2006, *Metrologia*, 43, S244

Richards D. W., Comella J. M., 1969, *Nature*, 222, 551

Sagan C., 1994, *Pale blue dot: A vision of the human future in space*. Random House, New York, NY, USA

Shapiro S. L., Teukolsky S. A., 1983, *Black holes, white dwarfs and neutron stars: The physics of compact objects*. John Wiley & Sons, New York, NY, USA

Staelin D. H., Reifenstein III E. C., 1968, *Science*, 162, 1481

Taylor J. H., 1992, *Philos. Trans. Roy. Soc. London A*, 341, 117

van Straten W., 2003, PhD thesis, Swinburne University of Technology, Melbourne, VIC, Australia

- van Straten W., 2004, *ApJS*, 152, 129
- van Straten W., 2008, personal communication
- van Straten W., 2010, personal communication
- Verbiest J. P. W., 2009, PhD thesis, Swinburne University of Technology, Melbourne, VIC, Australia
- Verbiest J. P. W., Bailes M., Coles W. A., Hobbs G. B., van Straten W., Champion D. J., Jenet F. A., Manchester R. N., Bhat N. D. R., Sarkissian J. M., Yardley D., Burke-Spolaor S., Hotan A. W., You X. P., 2009, *MNRAS*, 400, 951
- Xilouris K. M., Kramer M., Jessner A., von Hoensbroech A., Lorimer D., Wielebinski R., Wolszczan A., Camilo F., 1998, *ApJ*, 501, 286
- Yardley D. R. B., Hobbs G. B., Jenet F. A., Verbiest J. P. W., Wen Z. L., Manchester R. N., Coles W. A., van Straten W., Bailes M., Bhat N. D. R., Burke-Spolaor S., Champion D. J., Hotan A. W., Sarkissian J. M., 2010, *MNRAS*, 407, 669
- You X. P., Hobbs G., Coles W. A., Manchester R. N., Edwards R., Bailes M., Sarkissian J., Verbiest J. P. W., van Straten W., Hotan A., Ord S., Jenet F., Bhat N. D. R., Teoh A., 2007, *MNRAS*, 378, 493



Figure 5.1: The Earth, photographed in composite from a distance of 700 kilometres by the Terra satellite in 2001, and augmented by various other observations. It has been named the “blue marble” after the image taken from the Apollo 17 spaceship in 1972 (figure credit: NASA/GSFC/R. Stöckli & R. Simmon; NASA/MODIS; USGS/EROS; USGS/FFC; NOAA/DMSP).